MODAL METHODS FOR PHOTONIC DEVICES

MODAL METHODS FOR MODELING AND SIMULATION OF PHOTONIC DEVICES

By

JIANWEI MU, B.ENG., M.Sc.

A Thesis

Submitted to the School of Graduate Studies

in Partial Fulfilment of the Requirements

for the Degree

Doctor of Philosophy

McMaster University

DOCTOR OF PHILOSOPHY (2011) McMaster University

(Electrical and Computer Engineering) Hamilton, Ontario

TITLE:	Modal Methods for Modeling and Simulation of Photonic Devices
AUTHOR:	Jianwei Mu
	M.Sc (McMaster University, Canada)
	B.ENG.(National University of Defense Technology, China)
SUPERVISOR:	Dr. Wei-Ping Huang
	Professor, Department of Electrical and Computer Engineering
NUMBER OF PAGES:	xiii, 137

Abstract

Optical waveguide structures and devices are the fundamental basic building blocks of photonic circuits which play important roles in modern telecommunication and sensing systems. With the fast development of fabrication technologies and in response to the needs of miniaturization and fast increased functionality in future integrated photonic chips, various structures based on high-index contrast waveguides, surface plasmonic polaritons structures, etc., have been widely proposed and investigated. Modeling and simulation methods, as efficient and excellent cost performance tools comparing to costly facilities and time-consuming fabrication procedures, are demanded to explore and design the devices and circuits before their finalization.

This thesis covers a series of techniques for modeling, simulation and design of photonic devices and circuits with the emphasis of handling of radiation wave and the related power couplings. The fundamental issue in optical waveguide analysis is to obtain the complete mode spectrum. In principle, we need the radiation modes to expand the arbitrary fields of an open waveguide. In practice, however, the continuum nature of the radiation modes makes them hard to use. The discrete leaky modes may approximately represent a cluster of radiation modes under some circumstance and can be utilized in mode expansion together with guided modes to significantly simplify the analysis of mode coupling problems in optical waveguides. However, the leaky modes are unbounded by nature and hence lack the usual characteristics of normal guided modes in terms of normalization and orthogonality. Recently a novel scheme for handling of radiation optical fields was proposed and demonstrated by applying perfectly matching

layers (PML) terminated with a perfectly reflecting boundary (PRB) condition. In this scheme, the radiation fields are represented in terms of a set of complex modes, some of which resemble the conventional leaky modes and others associated with the interaction between the PML media and the reflecting numerical boundaries. The mode spectrum is therefore split into the guided modes and complex modes which possess the normal mode features such as normalization and modal orthogonality. The seemingly paradoxical application of both the PML and PRB in the new method has in fact overcome one of the main challenges associated with this traditional method, i.e., the desire for discrete, orthogonal, and normalized modes to represent radiation fields and the need for elimination and reduction of spurious reflections from the edges of the finite computation window.

With the understanding of mode spectrum, a full vector mode matching method and a complex coupled mode method for analyzing the wave propagation in optical waveguides under the framework of PRL and PRB computation model have been proposed. The methods have been validated through various structures such as waveguide facet, polarization rotators, long/short period gratings etc. Then the proposed techniques have been utilized to design a series of waveguide structures based on surface plasmonic polaritons, slot waveguides etc.

Acknowledgements

I would like to express my deepest gratitude to Dr. Wei-Ping Huang, my supervisor during my PhD study. This thesis would not have been possible without his encouragement, guidance, and support throughout my study and research at McMaster University.

I greatly appreciate Dr. Xun Li for his encouragement and inspiration during my postgraduate study. I am grateful for my supervisor committee members, Dr. M. Bakr, and Dr. C.Q. Xu for their advice and suggestions in my study. I would like to thank Dr. J. K. Zhang, Dr. S. Kumar, Dr. T. R. Field, my teaching assistant supervisors, for their help in my work.

I would like to show my gratitude to my former colleagues Dr. H. Zhang, Dr. M.H. Yan, Mr. K. Jiang, Dr. Y.P. Xi, and Dr. Y. Chen for their fruitful discussions. I am grateful for Dr. H. C. Chang from National Taiwan University and Dr. Y. Nakano from Tokyo University for their guidance during my summer research programs.

I would like to thank Ms. Cheryl Gies, Ms. Helen Jachna, Mr. Terry Greenlay and Mr. Cosmin Coroiu for their administrative works and technical support.

I also thank my colleagues and friends, Lei Zhao, Qingyi Guo, Lanxin Deng, Yu Li, Lin Han, Yudan Yan, Yi Lan, Qingyang Xu, Patrick Fayard, R. Mehdi, Xiao Deng, for their useful discussions. Special thanks are given to Mr. G. Dickson and the staff of the Hamilton Central Public Library Learning Center for their help in English and Canadian culture study.

I am heartily thankful to my family, they made this thesis possible.

Contents

List of Figures

Chapter 1 Introduction

1.1 Research Background

Analogous to electronic integrated circuits, photonic integrated circuits (PICs) or integrated optical circuits are devices which integrate multiple functional photonic components[1]. The advances of large-scale, monolithic photonic integrated circuits (PICs) have benefitted the fiber communication system significantly in many aspects such as system reliability, and cost reduction, etc[2-5].

Although the development benchmarks of photonic integrated devices and circuits are symbolized by the advances of high-density functional devices, processing technologies enabling the device production[6-11], the significance of the computer aided design (CAD) tools cannot be neglected[12, 13]. Not only can CAD tools lower the product early stage research cost, they can greatly shorten the design cycle by evaluating the feasibility of device concept, optimizing structure parameters, etc[14].

It should be noted, however, comparing to the CAD tools in designing electronic integrated circuits (RF circuits, for example), CAD tools for photonic devices and circuits are still in the early stage. Most CAD tools are method-oriented instead of problem-oriented. Consequently, photonic designs still rely heavily on the designer's experience. In fact, photonic CAD tools have become one of the bottlenecks of developing high-density functional photonic devices and circuits[15]. The ideal CAD tool should have the following features: high speed, satisfactory accuracy, low memory usage, and be free of arbitrary geometries. Sadly, none of the mainstream algorisms satisfies the above criteria,

thus the pursuing of stable, accurate and efficient simulation tools has attracted constant attention in recent years [14, 16].

According to the analysis domain, photonics CAD tools can be grouped into two classes: 1) time-domain methods; 2) frequency-domain methods. Time-domain methods represented by finite-difference time-domain method (FDTD) in which the Maxwell equations have been discretized in time and space, can be treated as rigorous, stable, and versatile approaches. FDTD has been widely used in integrated optics, particularly in photonic bandgap structures where frequency domain methods are difficult to handle [17, 18]. However, it is limited to devices of small size, due to the extremely long computation time and the high requirement for computer hardware. The frequency domain methods, represented by coupled mode theory (CMT)[19-22], beam propagation method (BPM)[23-25], and mode matching method (MMM)[26, 27] etc, are good at disclosing the physical properties and are superior to time domain methods in terms of computation effort. Each frequency domain method has its advantage: coupled mode theory (CMT) is considered as mathematically simple and accurate for relatively weakly guided optical waveguides; beam propagation method (BPM) based on the scattering operators can handle arbitrary waveguide structures but still computational expensive for periodic structures[25, 28-30]; on the other hand, mode matching method (MMM) has been known as an efficient and rigorous method for dealing with periodical structures [31]. The fundamental issue which affects the performance of the frequency-domain method is how to handle radiation fields. Although the input dielectric waveguide used in photonic integrated circuits is typically designed to support only one guided mode, most photonic

devices are not uniform along the wave propagation direction so reflection and radiation loss have to be considered. The radiation loss resulting from the power coupling between the guided mode and the radiation fields is difficult to solve due to the continuum nature of the radiation modes. Recent progress of BPM can handle the evanescent fields by introducing the complex coefficient Padé to approximate the propagator [32]. However, BPM is mainly used in two-dimensional problems due to the stability and convergence issues.

1.2 Research Motivations

This thesis is dedicated to developing stable, accurate frequency-domain analysis methods which can cope with the radiation fields. In particular, we will focus on the coupled mode theory, mode matching method and their related applications. As described in previous section, coupled mode theory (CMT) has been widely applied as an analytical approach for analysis of wave propagation and field interaction in optical waveguides. The classical coupled mode theory for optical waveguides was developed in 1970s [19-21, 33, 34], followed by a series of advances in both theoretical formulations and applications [35-39]. In CMT, the total field of an optical waveguide is expanded in normal modes of the reference waveguide, and a set of coupled ordinary differential equations is derived. Treatment of discrete guided modes has always been an advantage in the coupled-mode theory due to the fact that only phase matched modes play significant roles in the power exchange. Moreover, in practical optical waveguide structures such as optical fibers, an outer cladding region with lower refractive index and high loss is normally utilized. Under this circumstance, one can solve and apply the CMT

based on a more realistic model [40, 41]. However, for waveguides with infinite cladding (frequently used due to its simplicity) and with finite cladding with lower refractive index than that of the outer cladding (widely used for sensing applications), the radiation modes inevitably occur. For non-guided radiation fields, the application of coupled-mode theory becomes cumbersome due to the continuous spectrum of radiation modes. For certain waveguide structures such as step-index slab waveguides and circular fibers, analytical expressions for the radiation modes do exist and can be utilized [42, 43]. The problem is acute for waveguide structures for which analytical expressions for the radiation modes are not readily available. One possible solution to circumvent the problem of radiation modes is to introduce leaky modes to approximate the radiation modes. The leaky modes are, however, neither orthogonal nor normalizable in real domain [44, 45]. For this reason, it is difficult to deal with leaky mode formulations analytically and even more so numerically for practical applications.

A similar situation occurs for the mode-matching method in which both discrete guided modes and continuous radiation modes are required in the mode expansion in order to obtain accurate simulation results. Theoretically, the radiation modes may be discretized into a set of box modes by use of perfectly reflecting boundary condition enclosing the transverse structure of the waveguides. Practically, the size of the artificial box must be sufficiently large in order to achieve an accurate approximation for the radiation modes. Consequently, a large of number of box modes must be used.

Recently a new computation model was introduced to the mode-matching method in which the waveguide structure is enclosed by perfectly matched layers (PML)

terminated by a perfectly reflecting boundary conditions (PRB) [46-49]. This seemingly paradoxical combination of PML and PRB leads to a somewhat unexpected yet remarkable result: it creates an open and reflectionless environment equivalent to the original physical domain in a closed and finite computation domain. A set of complex modes can be derived from this waveguide model that are well behaved in terms of orthogonality and normalization and can be readily solved by standard analytical and numerical techniques. By utilizing the complex modes as orthogonal basis functions to represent the radiation fields, the mode-matching method can be applied as if all the modes are discrete and guided. So far, the finite-difference based numerical implementation of MMM for the analysis of three-dimensional structures has been reported under the semi-vector approximation [50]. It is true that the semi-vector approximation is sufficient for many practical optical waveguides in which the modal fields are predominantly linearly polarized and the coupling between the field components is negligible. However, the hybrid nature of the modes in high-index contrast waveguides is usually strong and can not be ignored. In order to accurately simulate such devices—polarization rotators [51], for instance, the semi-vector approximation is deficient and the full vector approach is mandatory.

In this work, within the framework of PML and PRB computation model, we develop a finite-difference based full-vectorial MMM for three-dimensional propagation problems. Further, the complex coupled mode theory based on complex modes has been proposed and applied to investigate the radiation coupling in short/long period gratings.

Another objective of this work is to design photonic devices and evaluate their

feasibilities. Bragg gratings based on slot waveguides, surface plasmon polaritions (SPPs) have been proposed and simulated by complex mode matching method.

1.3 Thesis Outline

In Chapter 1, the necessity and significance of photonic CAD has been presented with an emphasis of frequency-domain analysis methods. The challenges of the current modeling algorisms have been discussed and the motivation of the research has been described.

Chapter 2 describes the fundamental governing equations for full vector wave analysis in optical waveguides.

In Chapter 3, the finite difference method for modal calculation of optical waveguide structure has been described. The perfect matching layers and the zero boundary conditions, together with their implementations, have been presented in detail.

In Chapter 4, a three-dimensional full vectorial complex mode matching method has been derived and validated through examples of waveguide facets and polarization rotators. Bragg gratings based on surface plasmonic polaritons and slot waveguides have been proposed and analyzed by the complex mode matching method.

In Chapter 5, a complex coupled mode theory is developed for reflective/transmission gratings, and for waveguide tapers. The effectiveness and the applicability have been evaluated with comparison with rigorous numerical methods.

We summarize the major contributions and future suggestions in Chapter 6.

Chapter 2 Fundamental Equations of Optical Waveguides

2.1 The Wave Equations in Frequency Domain

In this thesis, we make the following assumptions: (1) the medium in the waveguide structure is lossless, linear, and isotropic. The permittivity and permeability of vacuum are denoted as ε_0 and μ_0, respectively. The permeability μ in the medium is equal to the free space value μ_0 throughout this thesis. (2) the time dependency is expressed as $\exp(j\omega t)$. The wave is propagating along z, and the z dependency is expressed as $\exp(-j\beta z)$ which refers to the propagation in the positive z direction, or $\exp(j\beta z)$ in the negative z direction. ω and β are the angular frequency and the propagation constant, respectively.

We consider a waveguide structure where the transverse index profile $n(x,y)$ is arbitrary and defined in the Cartesian coordinate system. The Maxwell's equations can be written as

$$\nabla \times E = -j\omega\mu_0 H \tag{2.1}$$

$$\nabla \times H = j\omega\varepsilon_0 n^2 E \tag{2.2}$$

$$\nabla \cdot \left(n^2 E\right) = 0 \tag{2.3}$$

$$\nabla \cdot \left(H\right) = 0 \tag{2.4}$$

The two curl equations are characteristic equations for analysis of simulation of the wave propagation in dielectric materials. The coupled vector wave equations, however, can be decoupled to two sets of equations based on either the transverse electric or magnetic fields.

2.1.1 E formulations for mode analysis

The vector wave equation for the electric field is derived from eqs. (2.1)-(2.2)

$$\nabla\times\left[\nabla\times E\right]=n^2k^2E \tag{2.5}$$

where $k=\omega\sqrt{\varepsilon_0\mu_0}$ is the wave number in free space. By using the vector identity

$$\nabla\times\nabla\times=\nabla\left(\nabla\cdot\right)-\nabla^2 \tag{2.6}$$

Eq. (2.5)becomes

$$\nabla^2E+n^2k^2E=\nabla\left(\nabla\cdot E\right) \tag{2.7}$$

where the terms of the RHS contains all the vectorial properties of the electromagnetic field.

We can easily obtain longitudinal field components once the transverse components of an electromagnetic field are known through $\nabla\cdot\left(n^2E\right)=0$. Consequently, the transverse components are sufficient to describe the vectorial characteristics of the electromagnetic field. The transverse components of eq. (2.7) is

$$\nabla^2E_t+n^2k^2E_t=\nabla_t\left(\nabla_t\cdot E_t+\frac{\partial E_z}{\partial z}\right) \tag{2.8}$$

where E_t and E_z are the transverse and longitudinal field components, respectively.

Utilizing $\nabla\cdot\left(n^2E\right)=0$, we obtain

$$\nabla_t\left(n^2E_t\right)+\frac{\partial n^2}{\partial z}E_z+n^2\frac{\partial E_z}{\partial z}=0 \tag{2.9}$$

For mode analysis, $n(x,y)$ is z-invariant, $\partial n^2/\partial z=0$, eq. (2.9) reduced to

$$\frac{\partial E_z}{\partial z}=-\frac{1}{n^2}\nabla_t\left(n^2E_t\right) \tag{2.10}$$

Substituting (2.10)into (2.8), and using the transformation

$$E(x,y,z)=E(x,y)e^{-j\beta z} \tag{2.11}$$

One can derive the vectorial wave equation for the transverse electric field,

$$\nabla_t^2E_t+\left(n^2k^2-\beta^2\right)E_t=\nabla_t\left[\nabla_t\cdot E_t-\frac{1}{n^2}\nabla_t\cdot\left(n^2E_t\right)\right] \tag{2.12}$$

Eq. (2.12) can be written in matrix form

$$\begin{bmatrix}P_{xx} & P_{xy}\\ P_{yx} & P_{yy}\end{bmatrix}\begin{bmatrix}E_x\\ E_y\end{bmatrix}=\beta^2\begin{bmatrix}E_x\\ E_y\end{bmatrix} \tag{2.13}$$

where the differential operators are defined as

$$P_{xx}E_x=\frac{\partial}{\partial x}\left[\frac{1}{n^2}\frac{\partial}{\partial x}\left(n^2E_x\right)\right]+\frac{\partial^2E_x}{\partial y^2}+n^2k^2E_x \tag{2.14}$$

$$P_{xy}E_y=\frac{\partial}{\partial x}\left[\frac{1}{n^2}\frac{\partial}{\partial y}\left(n^2E_y\right)\right]-\frac{\partial^2E_y}{\partial y\partial x} \tag{2.15}$$

$$P_{yy}E_y=\frac{\partial}{\partial y}\left[\frac{1}{n^2}\frac{\partial}{\partial y}\left(n^2E_y\right)\right]+\frac{\partial^2E_y}{\partial x^2}+n^2k^2E_y \tag{2.16}$$

$$P_{yx}E_x=\frac{\partial}{\partial y}\left[\frac{1}{n^2}\frac{\partial}{\partial x}\left(n^2E_x\right)\right]-\frac{\partial^2E_x}{\partial x\partial y} \tag{2.17}$$

Eq. (2.13) is a full vectorial equation. All the vectorial properties of the electromagnetic field are included. $P_{xx}\neq P_{yy}$ causes the polarization dependence whereas

$P_{xy} \neq 0$ and $P_{yx} \neq 0$ induces the polarization coupling between the two components E_x, E_y. If the coupling between the two polarization is weak and negligible, by neglecting the cross terms P_{xy} and P_{yx}, the full vectorial (2.13) reduces to two decoupled equations:

$$P_{xx}E_x = \beta^2 E_x \tag{2.18}$$

$$P_{yy}E_y = \beta^2 E_y \tag{2.19}$$

There is only one transverse field component in Eqs. (2.18)-(2.19), and the eigenmodes associated with those equations are commonly named as quasi-TE modes and quasi-TM modes. The equations are referered to semivecotrial vector equations. If the structures are weakly-guiding, even the polarization dependence may be neglected. Eq (2.13) reduces to

$$P_{xx} = P_{yy} = \frac{\partial^2}{\partial x^2} + \frac{\partial^2}{\partial y^2} + n^2 k^2 \tag{2.20}$$

Since the polarization difference is negligible, we call this scalar approximation. Eqs. (2.18),(2.19)are then replaced by a single equation

$$P\Psi = \beta^2 \Psi \tag{2.21}$$

2.1.2 H formulations for mode analysis

Similarly, we can derive the vectorial wave equation based on the transverse magnetic field from eqs. (2.1)-(2.2),

$$\nabla_t^2 H_t + \left(n^2 k^2 - \beta^2\right) H_t = \nabla_t \left[\nabla_t \cdot H_t - \nabla_t \cdot \left(H_t\right)\right] \tag{2.22}$$

Eq. (2.22)can be written in matrix form

$$\begin{bmatrix} B_{xx} & B_{xy} \\ B_{yx} & B_{yy} \end{bmatrix} \begin{bmatrix} H_x \\ H_y \end{bmatrix} = \beta^2 \begin{bmatrix} H_x \\ H_y \end{bmatrix} \tag{2.23}$$

where the differential operators are defined by

$$B_{xx}H_x = \frac{\partial^2 H_x}{\partial x^2} + n^2\left[\frac{\partial}{\partial y}\left(\frac{1}{n^2}\cdot\frac{\partial H_x}{\partial y}\right)\right] + n^2k^2H_x \tag{2.24}$$

$$B_{xy}H_y = \frac{\partial^2 H_y}{\partial y \partial x} - n^2\frac{\partial}{\partial y}\left(\frac{1}{n^2}\frac{\partial H_y}{\partial x}\right) \tag{2.25}$$

$$B_{yy}H_y = \frac{\partial^2 H_y}{\partial y^2} + n^2\left[\frac{\partial}{\partial x}\left(\frac{1}{n^2}\cdot\frac{\partial H_y}{\partial x}\right)\right] + n^2k^2H_y \tag{2.26}$$

$$B_{yx}H_x = \frac{\partial^2 H_x}{\partial x \partial y} - n^2\frac{\partial}{\partial x}\left(\frac{1}{n^2}\frac{\partial H_x}{\partial y}\right) \tag{2.27}$$

Eq. (2.23)is a full vectorial equation and all the vectorial properties of the electromagnetic waves are included. $B_{xx} \neq B_{yy}$ causes the polarization dependence. The polarization coupling happens between H_x and H_y when $B_{xy} \neq 0$ and $B_{yx} \neq 0$. If the coupling between the two polarizations is weak and negligible, we may neglect the cross terms B_{xy} and B_{yx} and simplify the full vectorial eqation (2.23) to two decoupled semivectorial equations:

$$B_{xx}H_x = \beta^2 B_x \tag{2.28}$$

$$P_{yy}E_y = \beta^2 E_y \tag{2.29}$$

Furthermore, for the weakly guided structures ($\frac{\partial n^2}{\partial x} \approx \frac{\partial n^2}{\partial y} \approx 0$), the polarization features may be neglected. The full vectorial eqation (2.23) becomes

$$B_{xx} \approx B_{yy} = \frac{\partial^2}{\partial x^2} + \frac{\partial^2}{\partial y^2} + n^2k^2 \tag{2.30}$$

Under the scalar approximation, eqs.(2.28), (2.29) are replaced by a single equation

$$P\Psi = \beta^2\Psi \tag{2.31}$$

2.2 Relation between the Fields

2.2.1 Relation between the fields from H to E

The transverse magnetic field components are obtained from solving eq. (2.22), and we can calculate the transverse electric field components from the magnetic field components by

$$E_x = \frac{Z_0 N_{eff}}{n^2} H_y - \frac{Z_0}{n^2 N_{eff} k^2}\left[\frac{\partial^2 H_y}{\partial x^2} + \frac{\partial^2 H_x}{\partial y \partial x}\right] \tag{2.32}$$

$$E_y = -\frac{Z_0 N_{eff}}{n^2} H_x + \frac{Z_0}{n^2 N_{eff} k^2}\left[\frac{\partial^2 H_x}{\partial y^2} + \frac{\partial^2 H_y}{\partial x \partial y}\right] \tag{2.33}$$

where $Z_0 = \sqrt{\mu_0 / \varepsilon_0}$ is the impedance of light in vacuum, and $N_{eff} = \beta / k_0$ is the modal index of the waveguide. For waveguides in which the transverse components coupling are weak ($\frac{\partial^2 H_{x,y}}{\partial y \partial x} \approx 0$), the expressions can be greatly simplified as

$$E_x = \frac{Z_0 N_{eff}}{n^2} H_y - \frac{Z_0}{n^2 N_{eff} k^2}\left(\frac{\partial^2 H_y}{\partial x^2}\right) \tag{2.34}$$

$$E_y = -\frac{Z_0 N_{eff}}{n^2} H_x + \frac{Z_0}{n^2 N_{eff} k^2}\left(\frac{\partial^2 H_x}{\partial y^2}\right) \tag{2.35}$$

This approximation is referred to semivectorial approximation. For weakly waveguides in which $\frac{\partial n^2}{\partial x} \approx \frac{\partial n^2}{\partial y} \approx 0$, we have the scalar mode approximation:

$$E = \pm \frac{Z_0}{N_{eff}} H \tag{2.36}$$

2.2.2 Relation between the fields from E to H

If we have the transverse electric field components obtained from eq. (2.13), we can find the transverse magnetic transverse field components by

$$H_x = -Y_0 N_{eff} E_y + \frac{Y_0}{N_{eff} k^2}\left\{\frac{\partial}{\partial y}\left[\frac{1}{n^2}\frac{\partial}{\partial y}\left(n^2 E_y\right)\right]+\frac{\partial}{\partial y}\left[\frac{1}{n^2}\frac{\partial}{\partial x}\left(n^2 E_x\right)\right]\right\} \tag{2.37}$$

$$H_y = +Y_0 N_{eff} E_y - \frac{Y_0}{N_{eff} k^2}\left\{\frac{\partial}{\partial x}\left[\frac{1}{n^2}\frac{\partial}{\partial x}\left(n^2 E_x\right)\right]+\frac{\partial}{\partial x}\left[\frac{1}{n^2}\frac{\partial}{\partial y}\left(n^2 E_y\right)\right]\right\} \tag{2.38}$$

where $Y_0 = \sqrt{\varepsilon_0 / \mu_0}$ is the admittance of light in vacuum. For waveguides with the weakly polarization coupling ($\frac{\partial}{\partial y}\left[\frac{1}{n^2}\frac{\partial}{\partial x}\left(n^2 E_x\right)\right] \approx \frac{\partial}{\partial x}\left[\frac{1}{n^2}\frac{\partial}{\partial y}\left(n^2 E_y\right) \approx 0\right]$), the semivector solutions are given by

$$H_x = -Y_0 N_{eff} E_y + \frac{Y_0}{N_{eff} k^2}\left(\frac{\partial}{\partial y}\left(\frac{1}{n^2}\frac{\partial}{\partial y}\left(n^2 E_y\right)\right)\right) \tag{2.39}$$

$$H_y = +Y_0 N_{eff} E_y - \frac{Y_0}{N_{eff} k^2}\left(\frac{\partial}{\partial x}\left(\frac{1}{n^2}\frac{\partial}{\partial x}\left(n^2 E_x\right)\right)\right) \tag{2.40}$$

For very weakly guided waveguide structures with $\frac{\partial n^2}{\partial x} \approx \frac{\partial n^2}{\partial y} \approx 0$, we have the scalar approximation:

$$\tilde{H} = \pm N_{eff} Y_0 \tilde{E} \tag{2.41}$$

where $\tilde{H}$ stands for H_x / H_y, and $\tilde{E}$ stands for E_x / E_y.

2.3 Normalization for Guided Modes

For general Media, the time average power for each guided mode is real and finite and can be normalized as:

$$\frac{1}{4}\iint_{Entire\ region}\left(E_{tn}\times H_{tn}^{*}+E_{tn}^{*}\times H_{tn}\right)\cdot\hat{z}dA=1 \tag{2.42}$$

where t denotes transverse components, and n denotes the mode number. The expression reduces to

$$\frac{1}{2}\iint_{Entire\ region}\left(E_{tn}\times H_{tn}\right)\cdot\hat{z}dA=1 \tag{2.43}$$

for lossless media. However, it is noted for general media

$$\frac{1}{2}\iint_{Entire\ region}\left(E_{tn}\times H_{tn}\right)\cdot\hat{z}dA=N_{n} \tag{2.44}$$

where N_n may not be equal to unity and may even be complex!

2.4 Symmetry of Guided Modes

By definition, the propagation constants of the forward and backward guided modes are related by

$$\beta^{+}=-\beta^{-} \tag{2.45}$$

here "+" denotes forward direction, and "–" denotes backward direction). Consequently, it is readily proved that the relations between the forward fields and the backward fields can be expressed as

$$E_{t}^{+}=+E_{t}^{-} \tag{2.46}$$

$$H_{t}^{+}=-H_{t}^{-} \tag{2.47}$$

$$E_{z}^{+}=-E_{z}^{-} \tag{2.48}$$

$$H_{z}^{+}=+H_{z}^{-} \tag{2.49}$$

Therefore, we only need to solve for only one set, and the other set can be derived easily. This relation hold for medium is complex or anisotropic medium, as long as it is reciprocal. For lossless but nonreciprocal media, it is easily deduced that for lossless but nonreciprocal media, we have

$$\left(E_t^-\right)^* = +\left(E_t^+\right) \tag{2.50}$$

$$\left(H_t^-\right)^* = -\left(H_t^+\right) \tag{2.51}$$

$$\left(E_z^-\right)^* = +\left(E_z^+\right) \tag{2.52}$$

$$\left(H_z^-\right)^* = -\left(H_z^+\right) \tag{2.53}$$

It is easily concluded that for reciprocal and lossless media that

$$\begin{aligned} \Im\left(E_t^\pm\right) &= \Im\left(H_t^\pm\right) = 0 \\ \Re\left(E_z^\pm\right) &= \Re\left(H_z^\pm\right) = 0 \end{aligned} \tag{2.54}$$

Therefore, for an isotropic, passive, and lossless medium, the transverse field components of the guided modes are real whereas the longitudinal components are pure imaginary.

2.5 Orthogonality for Guided Modes

Let m and n denote the modal indices of two distinct guided modes with corresponding propagation constants represented by β_m and β_n, respectively. The governing equations for modes are easily deduced from Maxwell equations as

$$\nabla_t \times E_m - j\beta_m \hat{z} \times E_m = -j\omega\mu_0 H_m \tag{2.55}$$

$$\nabla_t \times H_m - j\beta_m \hat{z} \times H_m = +j\omega\varepsilon_0 n^2 E_m \tag{2.56}$$

$$\nabla_t \times E_n - j\beta_n \hat{z} \times E_n = -j\omega\mu_0 H_n \tag{2.57}$$

$$\nabla_t \times H_n - j\beta_n \hat{z} \times H_n = +j\omega\varepsilon_0 n^2 E_n \tag{2.58}$$

Dot-multiply eqs. (2.55) with H_n and (2.57)with H_m and subtract. We have

$$\nabla_t \cdot (E_m \times H_n - E_n \times H_m) - j(\beta_m - \beta_n)(E_m \times H_n - E_n \times H_m) \cdot \hat{z} = 0 \tag{2.59}$$

Integrate (2.59) over the entire cross section and utilize the Green's theorem. Note that the fields vanish at infinity, we have

$$(\beta_m - \beta_n) \iint_{\text{entire region}} (E_{tm} \times H_{tn} - E_{tn} \times H_{tm}) \cdot \hat{z} da = 0 \tag{2.60}$$

if $\beta_m \neq \beta_n$, then

$$\iint_{\text{entire region}} (E_{tm} \times H_{tn} - E_{tn} \times H_{tm}) \cdot \hat{z} da = 0 \tag{2.61}$$

Change m to $-m$ and make use the symmetric properties of the modes, we have

$$(\beta_m - \beta_n) \iint_{\text{entire region}} (E_{tm} \times H_{tn} - E_{tn} \times H_{tm}) \cdot \hat{z} da = 0 \tag{2.62}$$

if $\beta_m \neq -\beta_n$, then

$$\iint_{\text{entire region}} (E_{tm} \times H_{tn} + E_{tn} \times H_{tm}) \cdot \hat{z} da = 0 \tag{2.63}$$

By adding or subtracting (2.62)with (2.63) yields

$$\iint_{\text{entire region}} (E_{tm} \times H_{tn}) \cdot \hat{z} da = \iint_{\text{entire region}} (E_{tn} \times H_{tm}) \cdot \hat{z} da = 0 \tag{2.64}$$

This orthogonality relation is valid even for active or lossy media. In particular, if the media are passive and lossless, the orthogonality relation maybe rewritten as

$$\iint_{\text{entire region}} (E_{tm}^* \times H_{tn}) \cdot \hat{z} da = 0 \tag{2.65}$$

2.6 Confinement factor

The confinement factor is an important parameter featuring the percentage of the power being confined in the guided region of the waveguide. The confinement factor in

this thesis is defined by

$$\Gamma = \frac{\iint_{\text{Guided region}} \Re\left(E_x^* H_y - E_y^* H_x\right) dxdy}{\iint_{\text{Entire region}} \Re\left(E_x^* H_y - E_y^* H_x\right) dxdy} \tag{2.66}$$

2.7 Wave Equations of 2D Waveguide Structures

If the waveguide extends infinitely in the direction parallel to the transverse cross section, the electromagnetic waves will be confined only in one direction. Suppose the refractive index is uniform along y coordinates, then the electromagnetic fields do not change with y, i.e.,

$$\frac{\partial}{\partial y} = 0 \tag{2.67}$$

By applying this condition into eqs (2.8) and (2.22), we find there are two sets of solutions corresponding to the transverse(TE) and the transverse magnetic TM modes, respectively. Accordingly, only three components exist for TE modes and TM modes, namely, E_y , H_x , H_z for TE modes, and H_y , E_x , E_z for TM modes. The governing equations for TE modes can be expressed in terms of E fields

$$\frac{\partial^2 E_y}{\partial x^2} + \left(n^2 k_0^2 - \beta_{TE}^2\right) E_y = 0 \tag{2.68}$$

or H fields

$$\frac{\partial^2 H_x}{\partial x^2} + \left(n^2 k_0^2 - \beta_{TE}^2\right) H_x = 0 \tag{2.69}$$

The transverse electric field is related to the transverse magnetic field by

$$E_y = \frac{Z_0}{N_{TE}} H_x \tag{2.70}$$

Similarly, we can obtain the governing equations for TM modes in terms of E fields

$$\frac{\partial}{\partial}\left(\frac{1}{n^2}\frac{\partial}{\partial x}\left(n^2 E_x\right)\right)+\left(n^2 k_0^2 - \beta_{TM}^2\right)E_x = 0 \tag{2.71}$$

or H fields

$$n^2 \frac{\partial}{\partial y}\left(\frac{1}{n^2}\frac{\partial H_y}{\partial x}\right)+\left(n^2 k_0^2 - \beta_{TM}^2\right)H_y = 0 \tag{2.72}$$

The transverse electric field is related to the transverse magnetic field by

$$E_x = -\frac{N_{TM}}{n^2} Z_0 H_x \tag{2.73}$$

From the above analysis, it is clearly shown that the two sets of equations for TE and TM modes are dual to each other. We may obtain the solutions for TM modes from TE modes by replacing H for E, E for $-H$ and μ_0 for $\varepsilon_0 n^2$.

2.8 Summary

In this Chapter, the frequency-domain governing equations have been derived and discussed. The duality of electric fields and magnetic fields has been presented. Important properties of guided modes such as normalization, orthogonality have been described.

Chapter 3 Finite difference Method for Optical waveguide Mode Analysis

3.1 Introduction

The prerequisites of the simulation, analysis, design, and optimization of the optical waveguide structure is to determine the complete set of guided modes and radiation modes. In principle, the radiation modes need to be considered to expand the arbitrary fields of the open waveguide. In practice, however, the continuum nature of the radiation modes makes them hard to use. The discrete leaky modes, on the other hand, may approximately represent a cluster of radiation modes under some circumstance. The leaky modes are unbounded by nature and hence lack the usual characteristics of normal guided modes in terms of normalization and orthogonality [45].

Recently a novel scheme for handling of radiation optical fields was proposed and demonstrated by applying perfectly matching layers (PML) terminated with a perfectly reflecting boundary (PRB) condition [48, 49]. In this scheme, the radiation fields are represented in terms of a set of complex modes, some of which resemble the conventional leaky modes and others associated with the interaction between the PML media and the reflecting numerical boundaries. The mode spectrum is therefore split into the guided modes and complex modes which possess the normal mode features such as normalization and modal orthogonality. The seemingly paradoxical application of both the PML and PRB in the new method has in fact overcome one of the main challenges associated with this traditional method, i.e., the desire for discrete, orthogonal, and

normalized modes to represent radiation fields and the need for elimination and reduction of spurious reflections from the edges of the finite computation window. In this chapter, we will describe the computation model used in this work and the related implementations.

3.2 Computation Model

The schematic of the computation model is illustrated in Figure 3.1. The optical waveguide is enclosed by perfect matched layers terminated by perfect reflection boundaries.

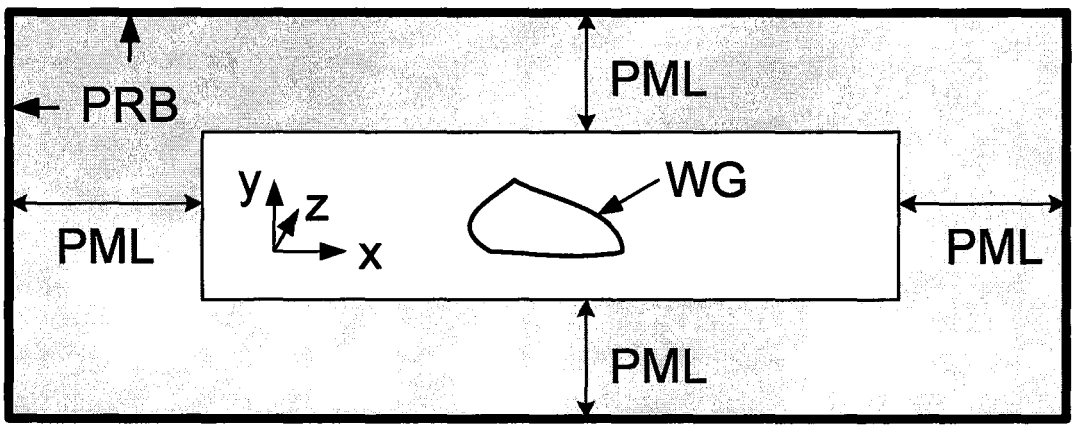

Figure 3.1. Mode computation model

One has to solve eq. (2.13) or eq. (2.23) to obtain the complete modal solutions. As described in the previous section, many numerical solutions are available for this task [52]. In this work, finite difference method is preferred due to its simplicity and straightforward implementation [53-55]. It should be noted that, for two dimensional waveguide structures, analytical methods are also qualifying the mode calculations within this computation framework [56-58] .

Although finite difference schemes have been widely used in solving partial difference equations, it is recently introduced into optical waveguide analysis by Stern[54]. In stern's approach, the discontinuity of the dielectric medium was matched by averaging the permittivity over meshes. For the sake of simplicity, we use the two-dimensional waveguide structures to illustrate the implementation of FDM. Considering the sampled field ϕ_i and the nearby field ϕ_{i+1} illustrated in Figure 3.2.

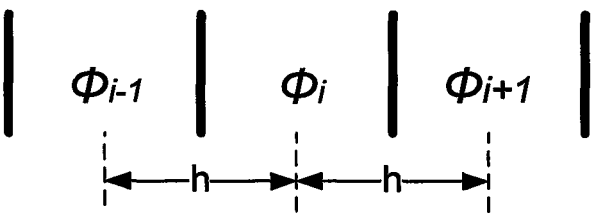

Figure 3.2 Schematic of interfaces between sampled points

Using the Taylor series expansion, the second derivative of ϕ_i is expressed as

$$\frac{d^2\phi_i}{dx^2} = \frac{\phi_{i+1} + \phi_{i-1} - 2\phi_i}{h^2} + O(h^3). \tag{3.1}$$

The TE modal equation(2.68) is discretized as

$$\frac{1}{h^2}\left(E_y^{i+1} + E_y^{i-1} - 2\hat{E}_y^i\right) + n_i^2 k_0^2 E_y^i = \beta^2 E_y^i, \tag{3.2}$$

and the TM modal equation(2.71) under this FDM scheme is discretized as

$$\frac{1}{h^2}\left(\frac{1}{\left(n_{i+0.5}^2\right)} \bullet E_x^{i+1} + \frac{1}{\left(n_{i-0.5}^2\right)} \bullet E_x^{i-1} - \left(\frac{1}{\left(n_{i+0.5}^2\right)} + \frac{1}{\left(n_{i-0.5}^2\right)}\right) E_x^i\right) + n_i^2 k_0^2 E_x^i = \beta^2 E_x^i \tag{3.3}$$

where

$$\begin{aligned} n_{i+0.5}^2 &= \frac{1}{2}\left(n_i^2 + n_{i+1}^2\right) \\ n_{i-0.5}^2 &= \frac{1}{2}\left(n_i^2 + n_{i-1}^2\right) \end{aligned} . \tag{3.4}$$

Combining all sampled points together the discretized modal equations become the eigen value problems,

$$\mathrm{A}\Phi = \beta^2\Phi . \tag{3.5}$$

where A is a sparse matrix. The eigenvalue problem can be solved efficiently with Arnoldi iteration method.

It's noted that the truncation error of this scheme is $O\left(h^0\right)$, where h is the mesh size. The truncation error is implied by the discretization scheme although the accuracy can be increased by using fine meshes. By using the Taylor series expansion at the interface of the refractive index discontinuities, Vassallo[59] provided an improved FDM scheme which has $O\left(h^2\right)$ truncation error when the interface is in the middle between the sampled points. Later on, this work is developed by Chiou[53] et al with the combination of the Generalized Douglas (GD) scheme. The truncation error of Chiou's scheme is $O\left(h^4\right)$ in the uniform discretization cases irrespective of the location of the interfaces. The high order finite difference scheme, is effective for two-dimensional waveguide analysis, however, is cumbersome in three-dimensional waveguide investigations[60].

3.3 Perfect Reflection Boundary Conditions

In this thesis, we are using perfect reflection boundary conditions (PRB) to terminate the computation window. For $M \times N$ grids, zero boundary conditions require that

$$\begin{aligned} \Phi_{0,n} &= 0 && n = 0,1,2,\cdots N \\ \Phi_{m,0} &= 0 && m = 0,1,2,\cdots M \\ \Phi_{M+1,n} &= 0 && n = 0,1,2,\cdots N \\ \Phi_{m,N+1} &= 0 && m = 0,1,2,\cdots M \end{aligned}$$

If the computation window is large enough, the field can be seen decaying to zero. However, parasite reflections may happen for radiative waves since they will be reflected back at the boundary thereby affect the simulation results. The problem is well overcome by the introduction of perfect matched layers and will be described in the next section.

3.4 Perfectly Matching Layers

The modal solutions for the forward propagating fields on the reference waveguide structures with PML are governed by the modified Maxwell's equations [50]

$$\nabla_t \times E - j\beta E = -j\omega\mu_o [\Lambda] H \tag{3.6}$$

$$\nabla_t \times H - j\beta H = +j\omega\varepsilon [\Lambda] E \tag{3.7}$$

where $\varepsilon(x,y)$ is the refractive index of the unperturbed reference waveguide without PML. The tensor $[\Lambda]$ accounts for the PML and is given by

$$[\Lambda] = \begin{bmatrix} S_y/S_x & 0 & 0 \\ 0 & S_x/S_y & 0 \\ 0 & 0 & S_x S_y \end{bmatrix} \tag{3.8}$$

where S_x and S_y are called the coordinate stretching factors and given by

$$S_x = \kappa_x - j\frac{\sigma_x}{\omega\varepsilon} \tag{3.9}$$

$$S_y = \kappa_y - j\frac{\sigma_y}{\omega\varepsilon} \tag{3.10}$$

and $\kappa_x(\kappa_y)$ and $\sigma_x(\sigma_y)$ are the parameters to control the phase shift and absorption of the travelling waves in the PML along x (y). For non-PML media, we have $\kappa_x = \kappa_y = 1$, $\sigma_x = \sigma_y = 0$.

In practice, we normally set the phase-shift parameter κ_x and κ_y to unity since they are significant only for dealing with evanescent fields. On the other hand, the profiles of the absorption coefficients σ_x and σ_y are critical for effectively reducing the reflections from the perfectly reflecting boundary. A commonly used expression for the absorption profile is

$$\sigma = \sigma_{\max}\left(\frac{\rho}{T_{PML}}\right)^m \tag{3.11}$$

where T_{PML} is the thickness of the PML layer and ρ is the distance measured from the starting position of the PML. A good measure for the effectiveness of the PML is the reflection coefficient defined by [61]

$$R_{PML} = \exp\left\{-\frac{2\sigma_{\max}}{n\sqrt{\varepsilon_o/\mu_o}}\int_0^{T_{PML}}\left(\frac{\rho}{T_{PML}}\right)^m d\rho\right\} \tag{3.12}$$

In terms of the PML reflection coefficient, the PML coefficient can be conveniently

expressed as

$$S = \kappa - j\frac{\lambda}{4\pi n T_{PML}}\left[(m+1)\ln\left(\frac{1}{R_{PML}}\right)\right]\left(\frac{\rho}{T_{PML}}\right)^{m} \tag{3.13}$$

It was shown that when $m = 2$ the PML seems to be the most effective.

3.5 Examples

To illustrate the salient features of the complex modes and their dependence on PML parameters, we calculate the mode effective indices and corresponding field patterns for a step-index slab waveguide with refractive indices of the core, inner cladding, and outer cladding equal to n_{co}, n_{cl}, and n_s, respectively (Figure 3.3). In particular, we vary the value of the refractive index in the outer cladding from lower, equal, and higher than/to the refractive index of the inner cladding so that the modal characteristics of the cladding guided, radiative, and leaky situations can be examined in detail. The waveguide parameters are chosen such that the refractive indices of the core and the inner cladding are n_{co}=1.458 and $n_{cl} = 1.450$, respectively. The half widths of the core and the inner cladding layers are $d_{co} = 2.5\mu m$ and $d_{cl} = 12.5\mu m$. The operation wavelength is assumed to be $\lambda = 1.550\mu m$. The thickness of the PML layer is $T_{PML} = 2.5\mu m$ and positioned at $d_{PML} = 38\mu m$. The PML absorption coefficient is chosen such that the total PML reflection coefficient is $R_{PML} = 10^{-12}$.

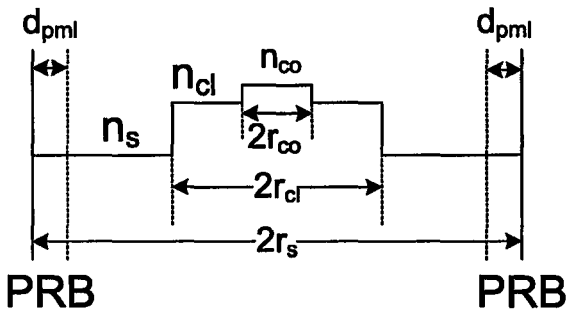

Figure 3.3 Schematic of five-layer step-index waveguide

In Figure 3.4(a), it shows the real and imaginary parts of the effective indices for the first twenty (20) modes supported in the waveguide for four different values of the refractive index in the outer cladding. In order to clearly observe the characteristics for the guided and quasi-leaky modes, we further blow up a portion of the graph in the dashed circle in Figure 3.4 (a) and show it in Figure 3.4 (b).

It is apparent that, in the case that the index of the outer cladding is lower than that of the inner cladding, all the modes are guided with real effective indices as if the PML and PRB do not exist. In the case of infinite cladding with $n_{cl} = n_s$ and leaky waveguide structures with outer cladding index higher than the inner cladding ($n_s > n_{cl}$), the cladding modes become complex and are divided into two groups, namely, the cladding quasi-leaky modes with the field mainly confined in the cladding region, and the PML modes with the field mainly concentrating in the PML region. The imaginary parts of the quasi-leaky modes represent the radiation loss. It is observed that, as the refractive index of the outer cladding increases from below to above that of the inner cladding, the leakage loss of the cladding modes increases. Further increase of

the outer cladding index, however, leads to a decrease in leakage loss due to the increase in reflection from the interface between the inner and outer cladding.

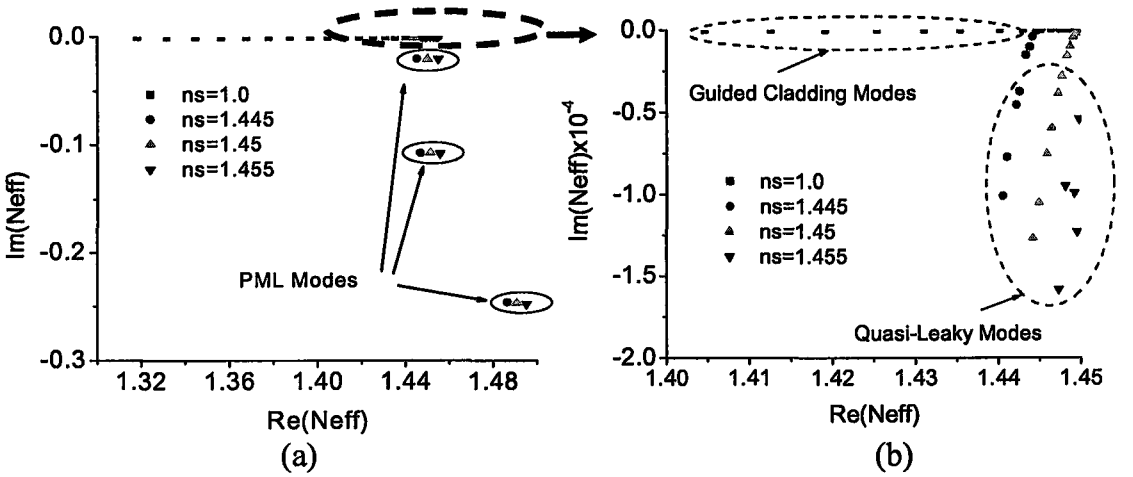

Figure 3.4 (a) Real and imaginary parts of the effective indices for the first twenty (20) modes (in descending order based on the values of the real part for the mode effective indices) supported in the waveguide for the different outer cladding indices. (b) A blow-up view for the portion of graph in (a) enclosed by the dashed circle.

In Figure 3.5, we plot the mode leakage loss defined as the power attenuation coefficient in dB per mm for the first five (5) quasi-leaky modes as functions of the outer cladding index. It is observed that the leakage losses of the higher-order complex modes are higher. In addition, we see that, as the refractive index of the outer cladding increase beyond that of the inner cladding, the leakage loss of the corresponding complex modes decreases due to the increase of the reflection at the inner and outer cladding interface.

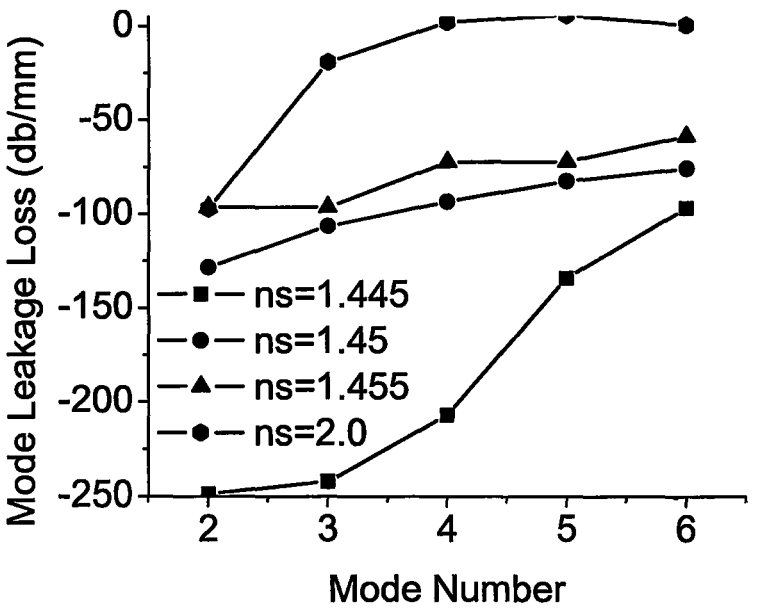

Figure 3.5. Mode leakage loss for the quasi-leaky modes.

Further, we observe the presence of the PML modes whose imaginary parts of the effective mode indices are much greater than those for the quasi-leaky modes. It is also noted that as the mode order increases, the imaginary parts of the PML modes increase but their real parts decrease, which are fundamentally different from the characteristics of the quasi-leaky modes.

The mode field patterns of the fundamental guided mode, the lowest order quasi-leaky cladding mode, and the lowest order PML mode are depicted in Figure 3.6 for the three waveguide structures (i.e., $n_s < n_{cl}, n_s = n_{cl}$ and $n_s > n_{cl}$).

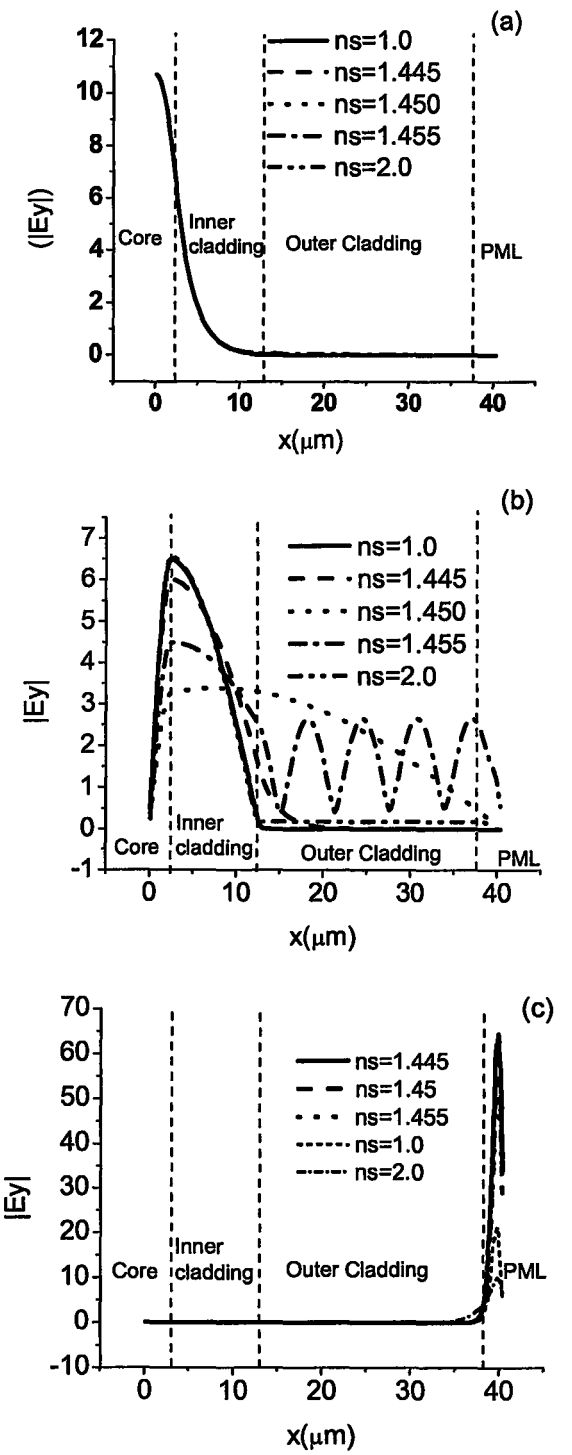

Figure 3.6 Mode field patterns: (a) the fundamental guided mode; (b) the quasi-leaky cladding modes; (c) the PML modes.

It is noted from Figure 3.6 that the guided mode is well confined in the core and hence not affected by the change of refractive index in the outer cladding as expected. On the other hand, fields of the quasi-leaky modes are primarily concentrated in the inner cladding region and hence highly sensitive to the variations of refractive index in the outer cladding. It is observed that more leakage for the cladding modes occurs when the refractive index of the outer cladding is slightly greater than that of the inner cladding, e.g., $n_s = 1.455$. The cladding mode suffers less loss as the index of the outer cladding becomes significantly larger than that of the inner cladding due to the reflection from the interface between the inner and the outer claddings. Finally, the PML modes are mainly present in the PML region and suffer huge mode losses.

The use of PML does introduce additional complexity in the waveguide model with more parameters. Therefore, it is instructive to investigate the effect on PML parameters on the mode characteristics. The field confinement factors in the core and the inner cladding as functions of PML reflection coefficients are shown in Figure 3.7(a) and Figure 3.7 (b), respectively.

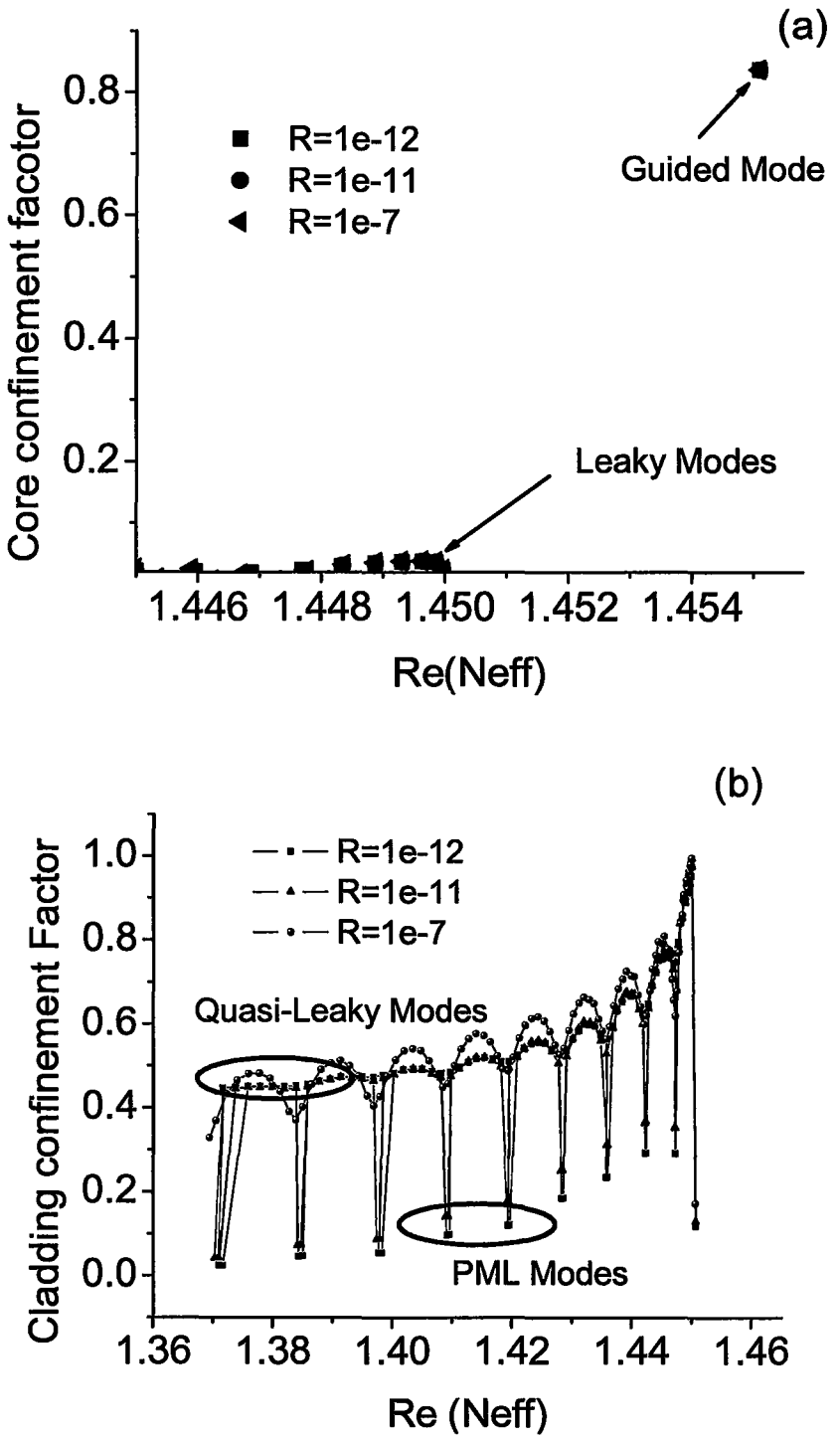

Figure 3.7. Field confinement factor as a function of PML parameters.

The field confinement factors in the core and the inner cladding as functions of computation window size are shown in Figure 3.8(a) and Figure 3.8 (b), respectively.

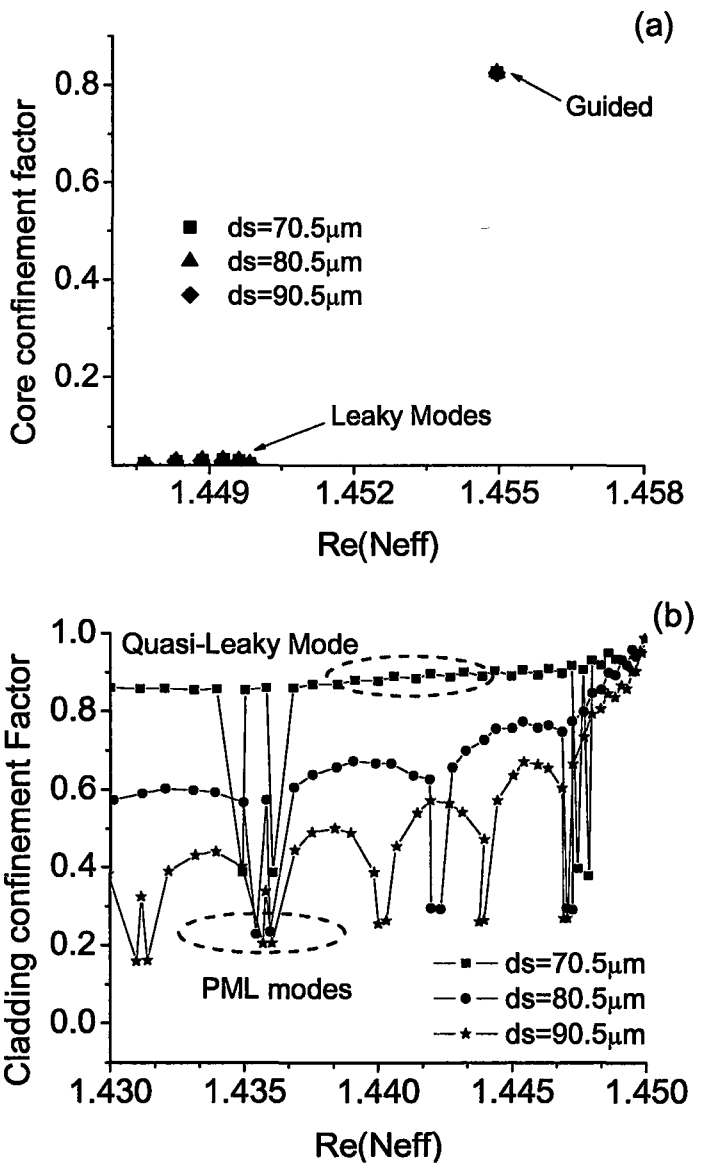

Figure 3.8. Field confinement factors in core and cladding region as functions of computation window (n_s=1.455).

It is observed that the core guided mode and the lower order cladding quasi-leaky

modes are not much affected by the variation of the PML parameters as shown in Figure 3.7 (a) and Figure 3.8 (a). On the other hand, the higher-order cladding leaky modes and the PML modes are more sensitive to the computation windows size and the PML absorption coefficient as shown in Figure 3.7 (b) and Figure 3.8 (b). The use of PML reflection of 10^{-12} and the computation window size of $90.5\mu m$ appears to be sufficient for the calculation of the complex modes of the waveguide under investigation.

Further, we investigate the modal orthogonality defined by eq. (2.64). For the first forty (40) modes obtained for the waveguide structure with infinite cladding ($n_s = n_{cl} = 1.450$). We show the results for the mode order m and n in Figure 3.9(a) and Figure 3.9 (b), respectively. The mode orthogonality defined in eq. (2.64) in terms of the overlap integral without complex conjugate is clearly demonstrated Figure 3.9 (a) for the complex modes. On the other hand, these complex modes are not necessarily power-orthogonal, i.e., the overlap integral with complex conjugate customarily used in the conventional coupled-mode theory are not always null, especially for the high-order complex modes as illustrated in Figure 3.9 (b). Nevertheless, for the coupling among guided and lower-order complex modes with relatively small leakage losses, the power orthogonality relationship is approximately valid as demonstrated in Figure 3.9 (b).

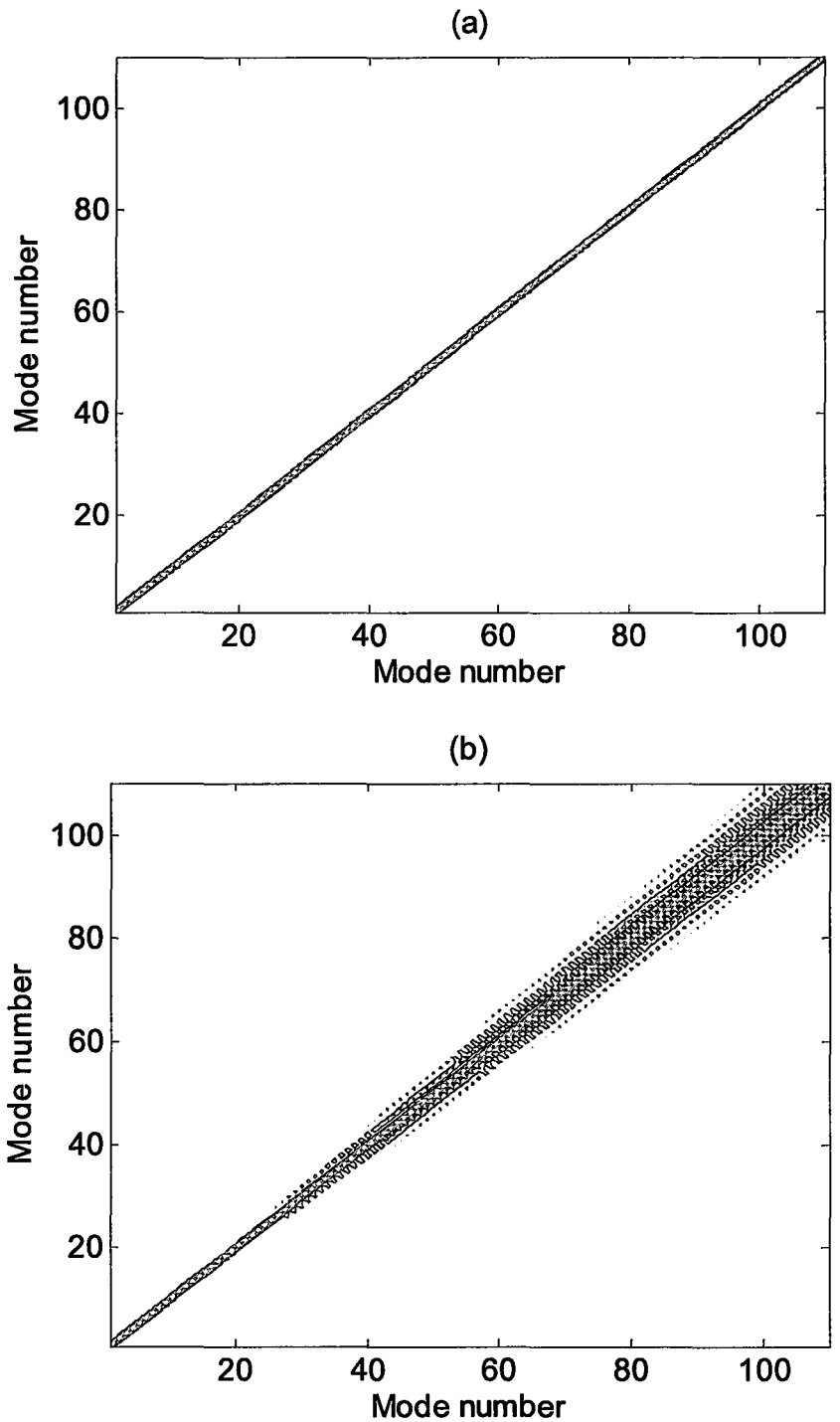

Figure 3.9. Mode field overlap integrals for different modes. (a)Non-conjugate overlapping integral using eq. (2.64); (b) Conjugate overlapping integral using eq. (2.65).

3.6 Summary

In this chapter, the computation model based on the combination of perfectly matched layers and perfect reflection boundary conditions has been described. It shows that within the current computation model, the complete mode spectrum consist of guided modes and complex modes. Characteristics of complex modes as functions of PML parameters have been discussed. The orthogonal relationship of complex modes has been disclosed and it is found that for higher order modes, non-conjugate overlapping integral should be used instead of conjugate overlapping.

Chapter 4

Complex Mode Matching Method

4.1 Introduction

Mode-matching method (MMM) has been known as an efficient and rigorous method in dealing with waveguide structures with longitudinal discontinuities especially for periodical structures. In MMM approach, the structure is divided into multiple homogenous sections. For each section, the total propagating field is expressed as the eigen-modes superposition. By applying the continuity conditions of tangential components of electric and magnetic field at the interfaces and the mode orthogonality relations, the different sections can be related by a scattering matrix. The entire reflection and transmission are calculated by cascading the scattering matrices. The theoretical formulations of the mode-matching method have been developed in the literature [31, 62]. The area of continuing interests and research activities has mainly concerned the treatment of the radiation fields for simulation of open waveguide structures. One of the widely used approaches was by enclosing the object with a sufficient large metal box so as to discretize the continuous radiation fields. The shortcoming associated with the computation model is that a large number of the modes in the box have to be considered to ensure adequate accuracy. Further, a detrimental oscillation error has been observed with change of the size of the computation window that is slow to diminish. Another scheme for implementation of the MMM is to represent the radiation field in terms of

Fourier expansion. In this treatment, a periodic boundary condition is implied and spurious reflections from the boundaries need to be dealt with [63].

Recently, a new scheme for the mode-matching method was proposed and demonstrated by applying perfectly matching layers (PML) terminated with a perfectly reflecting boundary (PRB) condition [48, 49]. In the new MMM scheme, the radiation fields are represented in terms of a set of complex modes, some of which resemble the conventional leaky modes and others associated with the interaction between the PML media and the reflecting numerical boundaries. The mode spectrum is therefore split into the guided modes and complex modes which possess the normal mode features such as normalization and modal orthogonality. So far, the finite-difference based numerical implementation of MMM for the analysis of three-dimensional structures has been reported under the semi-vector approximation. It is true that the semi-vector approximation is sufficient for many practical optical waveguides in which the modal fields are predominantly linearly polarized and the coupling between the field components is negligible. However, the modal hybridness in high index contrast waveguides is usually pronounced and can not be ignored. In order to accurately model such devices—polarization rotator, for example, the semi-vector approximation is deficient and the full vector approach is mandatory [51, 64].

4.2 Derivations of Complex Mode Matching Method

Considering a wave propagating from $z < 0$, at the first discontinuity ($z = 0$), part of the wave will be reflected into the region $z < 0$ and part of the wave will be transmitted into the region $z > 0$. Assuming that N modes are significant in both sides, the total

transverse fields in terms of the forward waves (denoted by "+") and backward waves(denoted by "−") can be expressed as:

for $z<0$

$$E_t^A=\sum_{i=1}^{N}(a_i^+e^{-j\beta_i^A z}+a_i^-e^{j\beta_i^A z})\vec{e}_{ti}^A, \tag{4.1}$$

$$H_t^A=\sum_{i=1}^{N}(a_i^+e^{-j\beta_i^A z}-a_i^-e^{j\beta_i^A z})\vec{h}_{ti}^A, \tag{4.2}$$

for $z>0$

$$E_t^B=\sum_{k=1}^{N}(b_k^+e^{-j\beta_k^B z}+b_k^-e^{j\beta_k^B z})\vec{e}_{tk}^B, \tag{4.3}$$

$$H_t^B=\sum_{k=1}^{N}(b_k^+e^{-j\beta_k^B z}-b_k^-e^{j\beta_k^B z})\vec{h}_{tk}^B. \tag{4.4}$$

Here, the superscripts A and B denote the waveguide sections $z<0$ and the first section as $z>0$, respectively; subscript t denotes the transverse component; the subscripts i and k denote mode index in waveguide A and waveguide B, respectively. $\vec{e}_t$ and $\vec{h}_t$ are the transverse electric and magnetic fields, and $a^{\pm}\left(b^{\pm}\right)$ are the amplitudes of forward and backward waves in waveguide A (B). The continuity of the tangential electric and magnetic fields at $z=0$ gives rise to

$$\sum_{i=1}^{N}(a_i^++a_i^-)\vec{e}_{ti}^A=\sum_{k=1}^{N}(b_k^++b_k^-)\vec{e}_{tk}^B, \tag{4.5}$$

$$\sum_{i=1}^{N}(a_i^+-a_i^-)\vec{h}_{ti}^A=\sum_{k=1}^{N}(b_k^+-b_k^-)\vec{h}_{tk}^B. \tag{4.6}$$

Taking the inner product of Eq. (15.a) with $\vec{h}_{tk}^{B}$ and $\vec{e}_{tk}^{B}$ with Eq.(15.b) , and utilizing the orthogonality relations, we obtain

$$b_k^+ = \sum_{i=1}^{N} a_i^+ \left[\frac{<\vec{e}_{ti}^{A}, \vec{h}_{tk}^{B}> + <\vec{e}_{tk}^{B}, \vec{h}_{ti}^{A}>}{2<\vec{e}_{tk}^{B}, \vec{h}_{tk}^{B}>} \right] + \sum_{i=1}^{N} a_i^- \left[\frac{<\vec{e}_{ti}^{A}, \vec{h}_{tk}^{B}> - <\vec{e}_{tk}^{B}, \vec{h}_{ti}^{A}>}{2<\vec{e}_{tk}^{B}, \vec{h}_{tk}^{B}>} \right], \tag{4.7}$$

$$b_k^- = \sum_{i=1}^{N} a_i^+ \left[\frac{<\vec{e}_{ti}^{A}, \vec{h}_{tk}^{B}> - <\vec{e}_{tk}^{B}, \vec{h}_{ti}^{A}>}{2<\vec{e}_{tk}^{B}, \vec{h}_{tk}^{B}>} \right] + \sum_{i=1}^{N} a_i^- \left[\frac{<\vec{e}_{ti}^{A}, \vec{h}_{tk}^{B}> + <\vec{e}_{tk}^{B}, \vec{h}_{ti}^{A}>}{2<\vec{e}_{tk}^{B}, \vec{h}_{tk}^{B}>} \right], \tag{4.8}$$

where the inner product of the field vectors is defined by

$$<\vec{e}, \vec{h}> = \frac{1}{2} \iint \left(\vec{e} \times \vec{h} \right) \cdot \hat{z} ds.$$

In the matrix form, we have

$$\begin{pmatrix} p^+ \\ p^- \end{pmatrix} = \begin{pmatrix} T_{11AB} & T_{12AB} \\ T_{21AB} & T_{22AB} \end{pmatrix} \begin{pmatrix} q^+ \\ q^- \end{pmatrix} = \mathrm{T}_{AB} \cdot \begin{pmatrix} q^+ \\ q^- \end{pmatrix}, \tag{4.9}$$

where $p\pm$ and $q\pm$ are defined as mode amplitude vectors ($b_1^{\pm}, b_2^{\pm}, \cdots b_N^{\pm}$) and ($a_1^{\pm}, a_2^{\pm}, \cdots a_N^{\pm}$),respectively. T_{AB} denotes the transfer matrix across the discontinuous interface $z = 0$. In this work, scattering matrix is used since the transmission and reflection coefficients are easily obtained. The scattering matrix is written as

$$\begin{pmatrix} q^+ \\ p^- \end{pmatrix} = \begin{pmatrix} T_{A,B} & R_{B,A} \\ R_{A,B} & T_{B,A} \end{pmatrix} \begin{pmatrix} p^+ \\ q^- \end{pmatrix} = \mathrm{S}_{AB} \cdot \begin{pmatrix} q^+ \\ q^- \end{pmatrix} \tag{4.10}$$

The elements of scattering matrix S_{AB} are given by

$$T_{A,B} = T_{11AB} - T_{12AB} \cdot T_{22AB}^{-1} \cdot T_{21AB} \tag{4.11}$$

$$R_{B,A} = T_{12AB} \cdot T_{22AB}^{-1} \tag{4.12}$$

$$R_{\mathrm{A,B}} = -T_{22\mathrm{AB}}^{-1} \cdot T_{21\mathrm{AB}} \tag{4.13}$$

$$T_{\mathrm{B,A}} = T_{22\mathrm{AB}}^{-1} \tag{4.14}$$

The complete scattering matrix which characterizes a unit cell can be acquired by cascading the scattering matrix across the junction and propagation matrix within the z-invariant sections. Taking the example of section B, the propagation matrix is given by,

$$P_B = \begin{pmatrix} e^{-j\beta_1^B \Lambda_b} & & 0 \\ & \ddots & \\ 0 & & e^{-j\beta_N^B \Lambda_b} \end{pmatrix}, \tag{4.15}$$

where Λ_b is the section length. The elements of scattering matrix of a unit cell are given by

$$T_{\mathrm{A,B}}^{\mathrm{u}} = P_B \cdot T_{\mathrm{A,B}}, \tag{4.16}$$

$$R_{\mathrm{B,A}}^{\mathrm{u}} = P_B \cdot R_{\mathrm{B,A}} \cdot P_B, \tag{4.17}$$

$$R_{\mathrm{A,B}}^{\mathrm{u}} = R_{\mathrm{A,B}}, \tag{4.18}$$

$$T_{\mathrm{B,A}}^{\mathrm{u}} = T_{\mathrm{B,A}} \cdot P_B, \tag{4.19}$$

where u denotes the unit cell. The entire scattering matrix for the structures with multiple discontinuities can be obtained by cascading the scattering matrices layer by layer. Assuming that the scattering matrix linking the first interface with the $(m-1)^{\mathrm{th}}$ interface is given by

$$\begin{bmatrix} p_{m-1}^{+} \\ p_1^{-} \end{bmatrix} = \begin{bmatrix} T_{1,m-1} & R_{m-1,1} \\ R_{1,m-1} & T_{m-1,1} \end{bmatrix} \begin{bmatrix} p_1^{+} \\ p_{m-1}^{-} \end{bmatrix}, \tag{4.20}$$

and the scattering matrix linking the $(m-1)^{th}$ with m^{th} interfaces is given by

$$\begin{bmatrix} p_m^+ \\ p_{m-1}^- \end{bmatrix} = \begin{bmatrix} T_{m-1,m} & R_{m,m-1} \\ R_{m-1,m} & T_{m,m-1} \end{bmatrix} \begin{bmatrix} p_{m-1}^+ \\ p_m^- \end{bmatrix}, \tag{4.21}$$

the scattering matrix linking the first interface with the m^{th} interface can be easily obtained by

$$\begin{bmatrix} p_m^+ \\ p_1^- \end{bmatrix} = \begin{bmatrix} T_{1,m} & R_{m,1} \\ R_{1,m} & T_{m,1} \end{bmatrix} \begin{bmatrix} p_1^+ \\ p_m^- \end{bmatrix}, \tag{4.22}$$

where

$$T_{1,m} = T_{m-1,m}(I - R_{m-1,1}R_{m-1,m})^{-1}T_{1,m-1}, \tag{4.23}$$

$$R_{m,1} = T_{m-1,m}(I - R_{m-1,1}R_{m-1,m})^{-1}R_{m-1,1}T_{m,m-1} + R_{m,m-1}, \tag{4.24}$$

$$R_{1,m} = T_{m-1,1}(I - R_{m-1,m}R_{m-1,1})^{-1}R_{m-1,m}T_{1,m-1} + R_{1,m-1}, \tag{4.25}$$

$$T_{m,1} = T_{m-1,1}(I - R_{m-1,m}R_{m-1,1})^{-1}T_{m,m-1}. \tag{4.26}$$

Here I is the identity matrix. It is noted that the computation efforts could be significantly reduced when the structure contains periodic cells such as Bragg reflectors. The key idea is to find the equivalent scattering matrix of s cells. The scattering matrix of $2s$ periods is obtained by cascading the two identical scattering matrices of s cells. Taking the advantage of symmetric features, for any M periods, only $\log_2 M + 1$ or $\log_2 (M+1)$ steps (depends on whether M is an integer power of 2) needed, therefore, this method can speed up the calculation significantly.

4.3 Evaluations of Complex Mode Matching Method

The full-vector mode-matching method developed in the previous section will be applied to analyze the facet reflectivity of a buried waveguide structure (Figure 4.1). The

propagation is along z direction, and the transmission medium is assumed to be air. the operation wavelength is 1.30 μm.

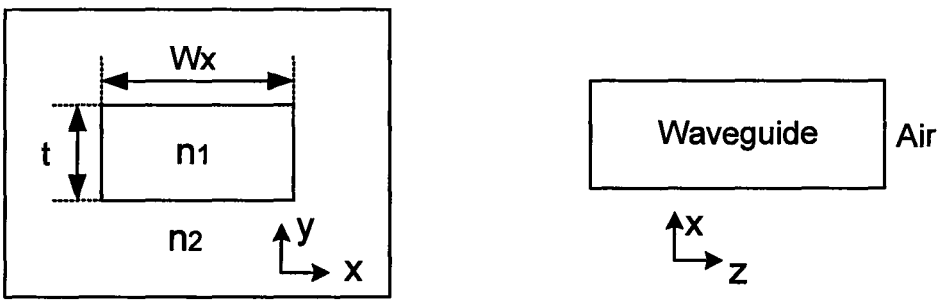

Figure 4.1. Buried waveguide structure

The modal facet reflectivities of the fundamental quasi-TE and quasi-TM modes against the core width wx have been calculated. The refractive indexes of the core and the cladding media are 3.54 and 3.17, respectively. The core thickness t is 0.4 μm. The simulation parameters are summarized as follows: the computational window size is 1.4μm ×2.4 μm (thickness ×width) including a perfectly matched layer (PML) of 0.2μm thickness on each side; the horizontal and vertical mesh sizes are 50 nm. Three hundred modes have been employed to increase the accuracy.

The modal reflectivities of the quasi-TE and quasi-TM modes against the core width of the buried waveguide are shown in Figure 4.2. Comparing with the reported results from full-vector and semi-vector approaches [28, 65], it is observed that the results from full-vector mode-matching method are in good agreement with that from the full-vector Bi-BPM. However, it is noted that there is a prominent discrepancy between the semi-vector and the full-vector approaches as the width and thickness of the structure

becomes comparable. In other words, the semi-vector method is valid for large structure aspect ratio r (defined by max (wx,t)/min (wx,t)).

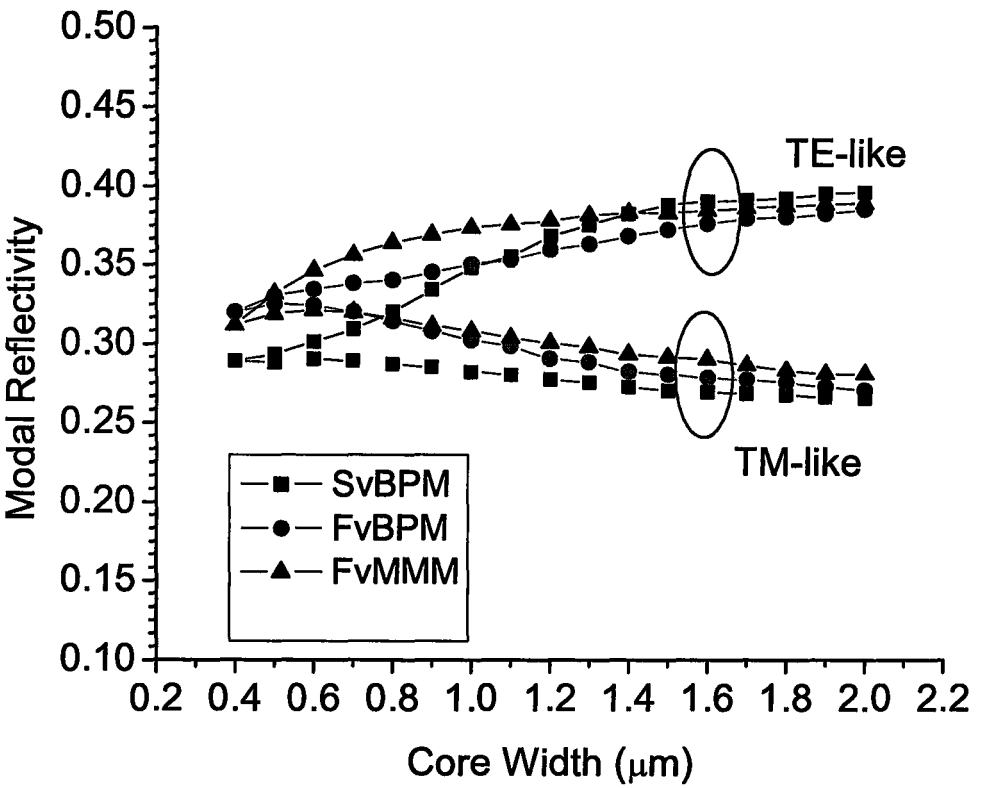

Figure 4.2. Calculated modal reflectivities of quasi-TE and quasi-TM modes. Solid triangles: full vector mode matching method; solid circles: full vector beam propagation method; solid squares: semi–vector beam propagation method.

We also investigated the convergence behaviour of the facet modal reflectivity of the buried waveguide as a function of mode numbers. The simulation parameters are summarized as follows: the width and thickness of the cross section are fixed at 0.4 μm; the computation window is set to 1.4μm × 1.4 μm (thickness × width) including a

perfectly matched layer (PML) of 0.2 μm thickness on each side. The facet reflectivity of the quasi-TE mode as a function of mode numbers is shown in Figure 4.3. It is observed that the modal reflectivity oscillates then converges to stable.

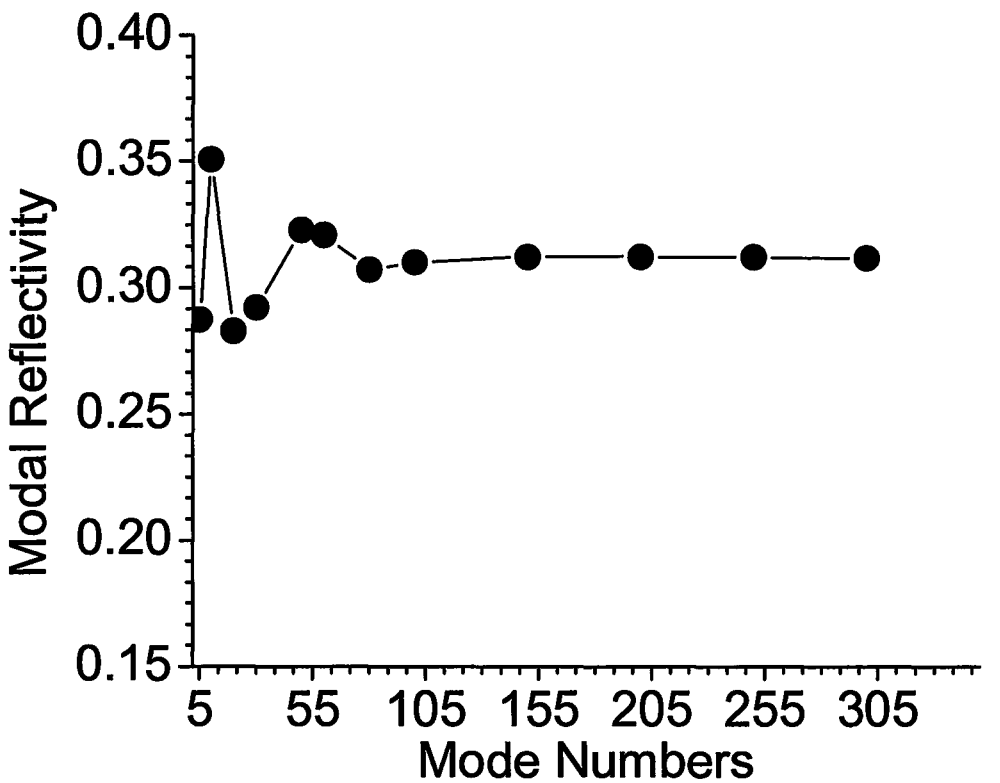

Figure 4.3. Facet modal reflectivity as a function of mode numbers.

To validate the full-vector finite-difference mode-matching method for multiple discontinuities, the polarization rotator which has been widely used in optical systems is simulated[64]. The structure consists of a buried waveguide (λ=20mm) with periodic perturbations (Figure 4.4). The structure parameters are summarized as follows: The refractive indexes of buried waveguide and the loadings are ε_r=2.8; the width (W) and the height (H) of the buried waveguide are 13mm and 6.5 mm, respectively. The width of

the loading (w) is chosen to be half of the waveguide structure, i.e., w=6.5mm. The height of the loaded strip (h) is chosen to be 2mm or 3mm. The phase matching condition between the fundamental quasi-TE and quasi-TM modes in the loaded sections gives rise to the loading length $d = \pi/(\beta_{TE} - \beta_{TM})$, where β_{TE} and β_{TM} are the propagation constants of the quasi-TE and quasi-TM modes, respectively.

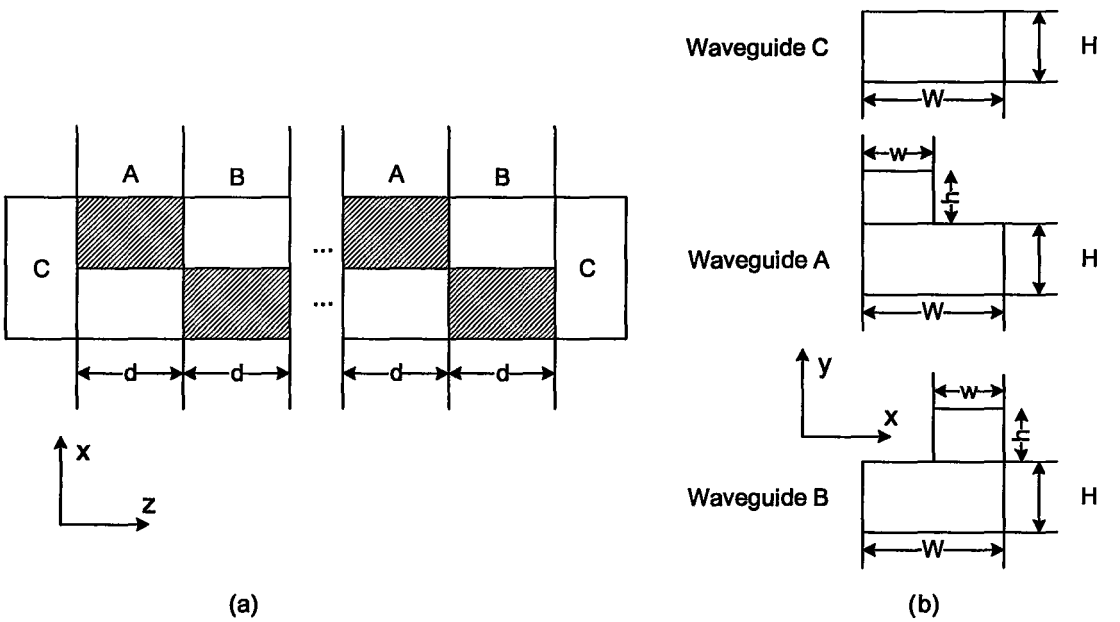

Figure 4.4. Schematic representation of a periodically loaded waveguide. (a) Top view (b) cross-section.

The parameters used in the simulations are summarized as follows: the computational window size is 35 × 35mm including a perfectly matched layer (PML) of 6 mm thickness on each side; the mesh sizes are fixed as $\Delta x = \Delta y$ =0.5mm, 60 modes are employed in the mode matching scheme. The power exchange as the function of loadings for h=2mm and h=3mm are shown in Figure 4.5 and Figure 4.6, respectively. It is observed that the simulation results agree well with the experimental results from ref [64].

The overall loss is proportional to the loading numbers which results from the radiation loss at the junctions.

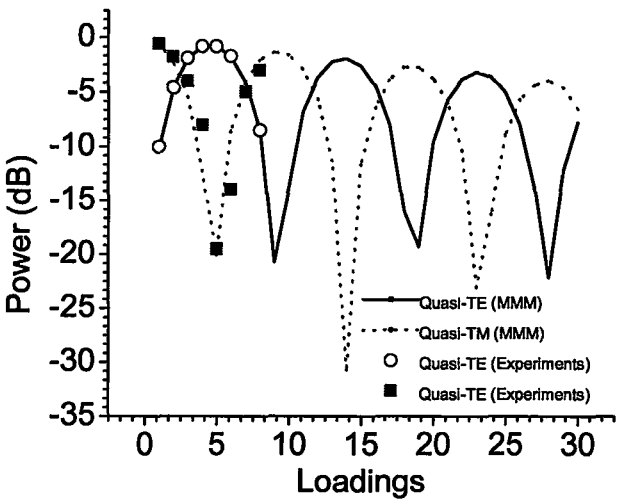

Figure 4.5. The Power exchange between quasi-TE and quasi-TM modes as the functions of loading numbers (h=2mm). Solid line: Quasi-TE from MMM; dot line: Quasi-TM from MMM; circle: Quasi-TE from experiments; square: Quasi-TM from experiments.

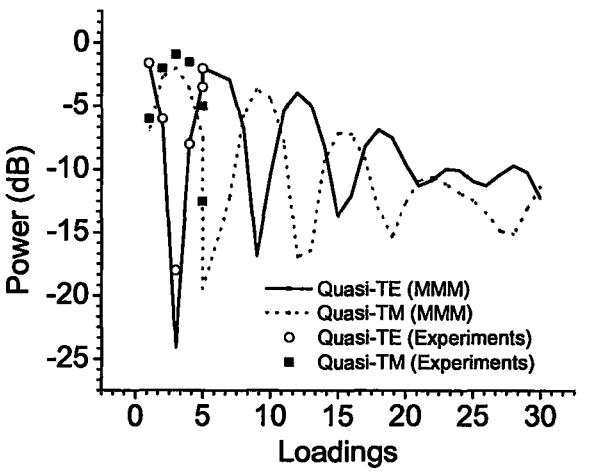

Figure 4.6. The Power exchange between quasi-TE and quasi-TM modes as the functions of loading numbers (h=3mm). Solid line: Quasi-TE from MMM; dot line: Quasi-TM from MMM; circle: Quasi-TE from experiments; square: Quasi-TM from experiments.

4.4 Applications of Mode Matching Method

4.4.1 Slot waveguide Grating

Photonic devices based on slot waveguide structures have recently attracted much attention as a solution to confine light in the low-index material within the nanometer range [66-69]. Different from the conventional optical waveguides in which the light is guided in high index medium by the total internal reflection (TIR)[33, 70], the slot waveguide confines the TM field in the low index region by way of strong discontinuities at the interface between the low-index core and the high-index claddings. The boundary condition for the dominant TM field at the interface dictates that the electric field is significantly higher in the low index region than that of the high-index cladding region so that the light can be confined and guided with low leakage losses as long as the slot width is smaller than the decay length of the field in the guiding region. The distinct characteristics of the slot waveguides have been explored in a number of applications, including optical modulators[71], direction couplers [72], optical sensing[73] and optical beam splitters[74]. In this section, we investigate by way of theoretical modeling and simulation, the important performance parameters of Bragg gratings based on dielectric slot waveguides such as the peak reflectivity, the field confinement factor, etc., against key design parameters such as the refractive index and width of the guiding layer, the widths of the cladding layer etc. The simulation is conducted by employing a complex mode matching method (CMMM) and the accuracy of the CMMM is validated by a bi-direction beam propagation method (Bi-BPM)[75] .

The waveguide grating is modeled as a periodic structure with a unit cell consisting of two sub-sections of different widths for the high-index claddings, namely, section A and section B in Figure 4.7. The width of the high index region of section A, the width of the high index cladding region of section B, slot core width, core refractive index, the section lengths of section A and section B are represented by w_{H1}, w_{H2}, w_L, n_L, Λ_A and Λ_B, respectively. The remaining waveguide parameters in our simulation are defined as follows: the refractive index of the high index cladding is n_H=3.48, the refractive index of the outer cladding is n_C=1.0, the desired central wavelength is λ_0=1550nm.

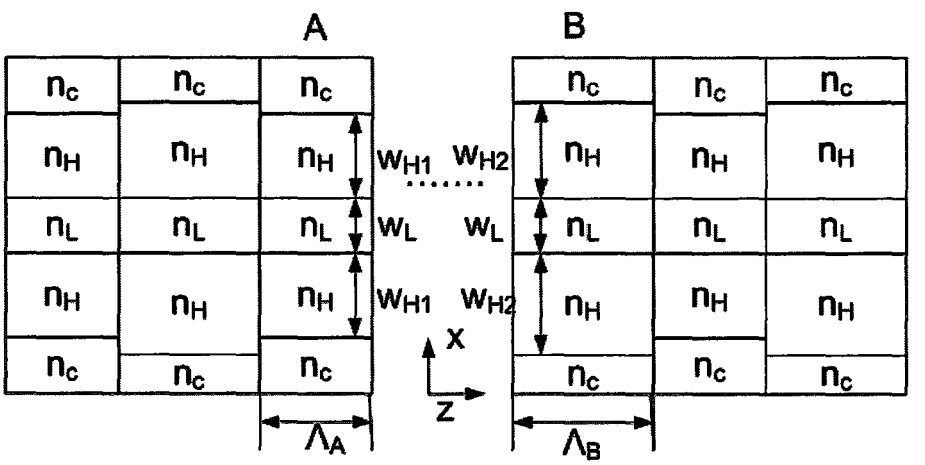

Figure 4.7. Schematic of a Bragg grating based on slot waveguide. The high index cladding width varies along the propagation direction in order to create a periodic perturbation.

The confinement factor in the slot region is defined as the fraction of power concentrated and guided in the slot core region:

$$\Gamma = \frac{\iint_{\text{core}} \frac{1}{n^2} \left| H_y(x) \right|^2 dx}{\iint_{\text{Entire}} \frac{1}{n^2} \left| H_y(x) \right|^2 dx}$$

We have assumed that the grating is due to the corrugation of the outer cladding surfaces, which may be readily realized by etching. The other reason for the grating on the outer cladding interfaces is that the field at the grating interface is relatively weak and the field mismatch between the adjacent grating sections is small. Hence, the scattering loss due to longitudinal discontinuities is relatively small. The method of simulation described below is equally applicable for other grating configurations such as gratings placed at the inner surface of the grating. As the field is stronger and the field mismatch larger under this circumstance, we expect that the scattering loss for this type of grating is higher than that of the outer interface for the same grating height. Also, we have simulated the vertically etched gratings based on a 2D structure. For a horizontally etched grating, the simple 2D model is no longer valid. We may reduce the 3D structure into an equivalent 2D structure by using effective index method in which the horizontal surface grating is converted into a volume grating. Such an approximation is, however, not very accurate and will not be pursued further in this paper.

For analysis of the slot waveguide gratings, we employ a complex mode matching method (CMMM), which is well suited for simulation of the periodic waveguide structures due to its intuitiveness, computation efficiency and accuracy, and the optical modes of the structure are calculated by a finite difference mode solver [53]. In the

CMMM, the structure under investigation is enclosed by perfectly matched layers (PML) terminated by perfectly reflecting boundaries (PRB) as illustrated in Figure 4.8.

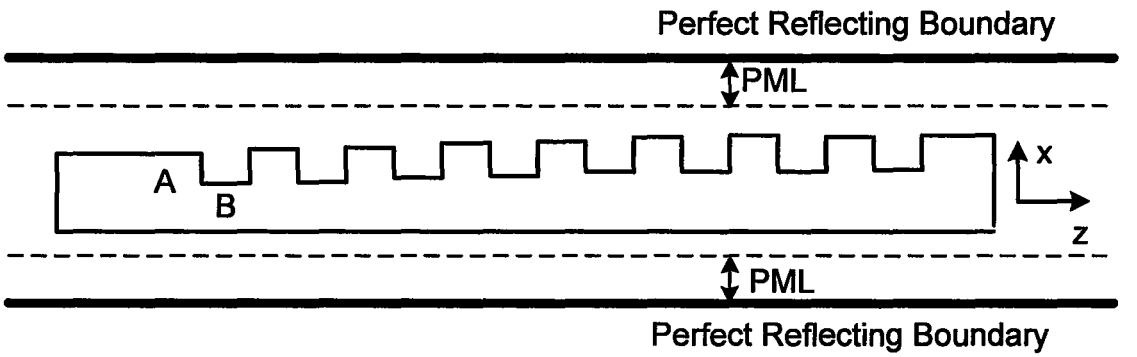

Figure 4.8. Sketch of the computation window: the studied structure is enclosed by perfectly matched layers terminated by perfectly reflecting boundaries (PRB).

To support and validate the complex mode matching method, we have also applied a different numerical method, namely, the bi-directional beam propagation method (Bi-BPM) to the same slot waveguide grating structures. The Bi-BPM based on scattering operators relies on the reflection operator and transmission operator. The reflected and transmitted fields can be calculated from these operators defined at the input interface, which are obtained by a sweeping process from the output to the input of the structure involving transition step and propagation step. The continuity conditions of tangential components of electric and magnetic field at the interface of discontinuities lead to the transition step. The propagation step is carried out by a normal one-way BPM process. The rational approximation such as rotated branch cut Padé approximation to the square root operators can be further applied in the transition step and propagation step.

In order to illustrate the accuracy and efficiency of the CMMM, the reflection spectrum of a designed slot waveguide grating (Figure 4.7) is calculated by CMMM and

Bi-BPM. The core width is w_L=20nm; The widths of the two high index cladding segments are w_{H1}=100nm and w_{H2}=110nm, respectively. The refractive index of the slot core region is n_L=1.0. The lengths of the two sections are Λ_A=0.31μm and Λ_B= 0.28μm, respectively. The number of periods is 20. Parameters used in the CMMM simulation are summarized as follows: the computational window size is 2.02μm including a perfectly matched layer (PML) of 0.2μm thickness on each side; 40 modes have been employed to achieve a sufficient precision. The parameters used in Bi-BPM are as follows: the computational window size is 2μm including a perfectly matched layer (PML) of 0.2μm thickness on each side; the longitudinal step sizes in n_0 and n_1 regions are $\Delta z_A = 0.031\,\mu m$ and $\Delta z_1 = 0.028\,\mu m$, respectively; the reference index is chosen to be the effective index of the corresponding waveguide segment. The complex Padé (8, 8) approximant is used in combination with a rotated angle $\alpha = \pi/2$.

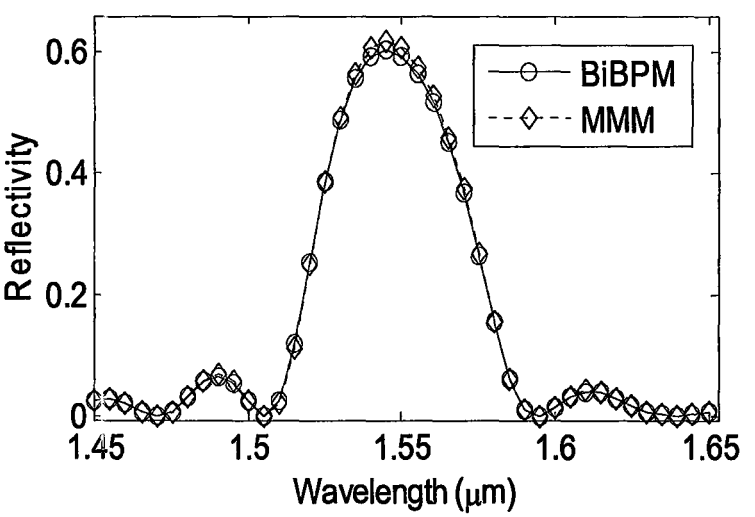

Figure 4.9. Reflection spectrum of slot waveguide grating Figure 4.7 with 20 periods. Circle: Bi-BPM; diamond: CMMM.

We present the reflection spectrum covering the wavelength range from 1.45μm to 1.65μm with a resolution of 5nm obtained by CMMM and Bi-BPM in Figure 4.9,. The good agreement of the two methods verifies the accuracy of CMMM.

A. Effect of the Refractive Index of the Guiding Layer

We first study the dependence of the optical confinement and peak reflection of the guiding layer, i.e., the slot core. The grating parameters used in the simulation are as follows: the core width is w_L=20nm. The widths of high index cladding region are w_{H1}=100nm and w_{H2}=110nm, respectively. The number of periods is 20.

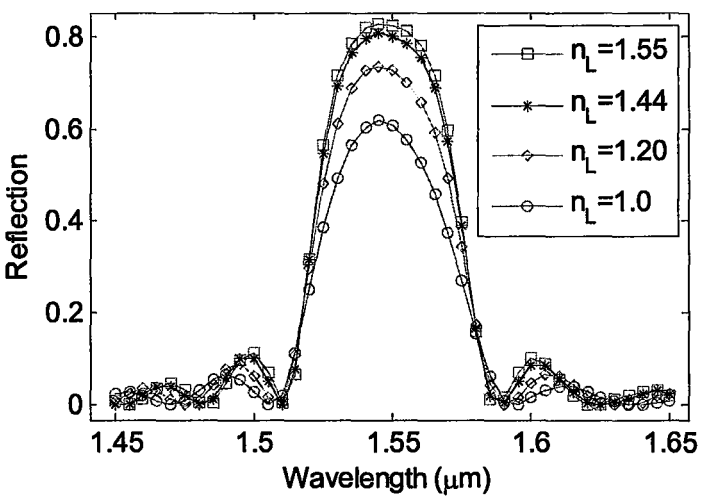

Figure 4.10. Reflection spectrum of slot waveguide grating of Figure 4.7 with 20 periods for different refractive indexes of the guiding layer. Circle: n_L=1.0; diamond: n_L=1.20; star: n_L=1.44; square: n_L=1.55.

The reflection spectra are calculated and displayed in Figure 4.10 as a function of refractive index of the guiding layer. It is observed that with increasing the refractive index of the guiding layer, the peak reflection tends to increase. On the other hand, the confinement factors in the guiding layer for the two grating sections decrease with the

increase of the guiding-layer refractive index as shown in Figure 4.11. The reason for the increase in peak reflectivity and decrease in confinement factors under this condition is that the field intensity near the outer interface of the cladding is enhanced as the index of the guidance layer increase, which leads to an increase in grating induced reflection. In the meanwhile, the field confinement in the guiding layer is reduced as the field spreads more out into the cladding regions.

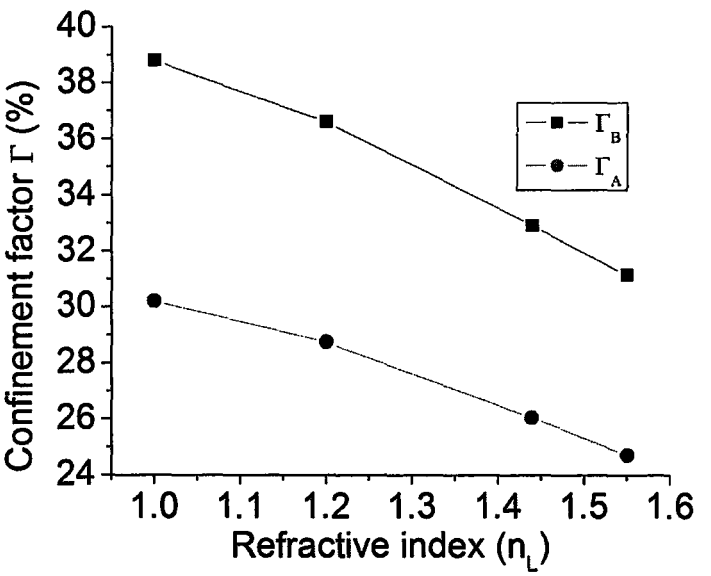

Figure 4.11. Confinement factor in the core region as functions of guiding-layer refractive index, w_L=20nm, w_{H1}=100nm, w_{H2}=110nm, the number of periods is 20. Solid square: confinement factor in section B; solid circle: confinement factor in section A.

We also investigate the peak reflection as a function of period numbers with respect to different core materials. Figure 4.12 shows the peak reflection with respect to grating length as core refractive index varying from 1.0 to 1.55. We observe that the general trend with respect to grating period numbers, namely, the peak reflection will

increase rapidly then get saturated to a maximum value. A maximum peak reflection of about 98% is observed in 75 periods.

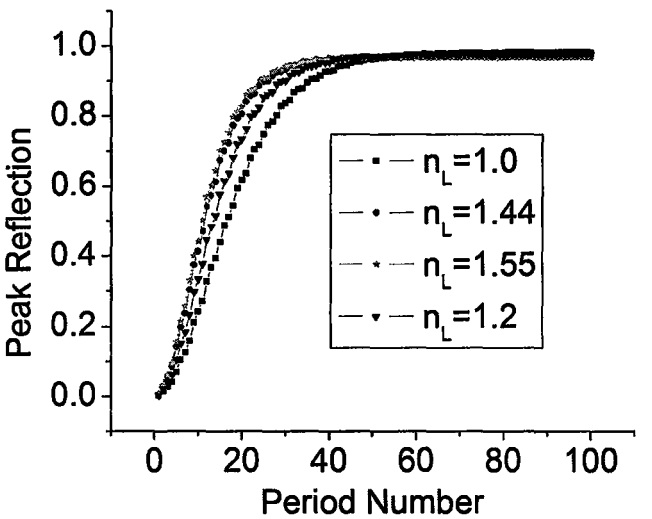

Figure 4.12. Peak reflection versus period numbers for different guiding-layer materials. w_L=20nm, w_{H1}=100nm, w_{H2}=110nm. Solid square: n_L= 1.0; solid circle: n_L=1.44; solid pentagram: n_L=1.55; solid downward pointing triangle: n_L=1.20.

B. Effect of the Width of the Guiding Layer

The effect of the slot width on the confinement factors and peak reflectivity is investigated in this section. We assume the widths of two high index cladding regions are w_{H1}=100nm and w_{H2}=110nm, respectively. The refractive index of the slot core region is n_L=1.0 and the number of periods is 20. We calculate the confinement factor of section A and B, and peak reflection as a function of the slot core width. The results are presented in Figure 4.13. It shows that the confinement factors in both sections A and B increase whereas the peak reflection decreases with the increase of width. From Figure 4.13, it is

observed that there is a tradeoff between confinement factors and peak reflectivity against the width of the slot width.

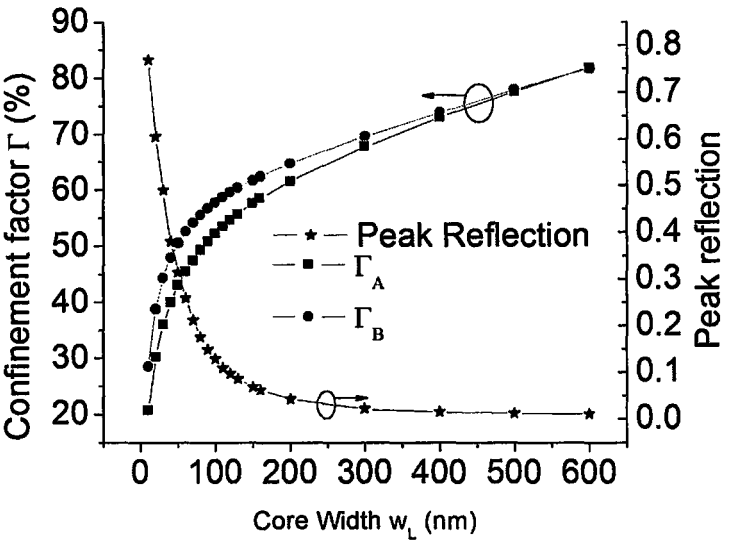

Figure 4.13. Peak reflection, confinement factors in core region of section A and confinement factor in core region of section B as functions of core width. solid square: confinement factor in section A; solid circle: confinement factor in section B; solid star: Peak reflection.

It is noted that the slot width used in the investigation for the effect of the refractive index of the guiding layer is 20 nm which is narrower than what has been experimentally demonstrated. The conclusion obtained from the analysis should be applicable for waveguides with larger slot width. In fact, we have studied the effect of slot width from 10 nm – 50nm in Section B and the results indeed support above claims.

C. Effect of the Width of the High Index Cladding

To reveal the dependence on the width of the high index cladding width (w_H) for the confinement factors and the peak reflection, we fix the difference of the high index

claddings, namely, $\Delta w = w_{H1} - w_{H2}$. By setting $\Delta w = 10nm$, the refractive index of the core $n_L = 1.0$, the width of the slot core $w_L = 20nm$ and 20 periods, we calculate the peak reflection and confinement factors as a function of high index cladding width w_{H1}. The results are shown in Figure 4.14.

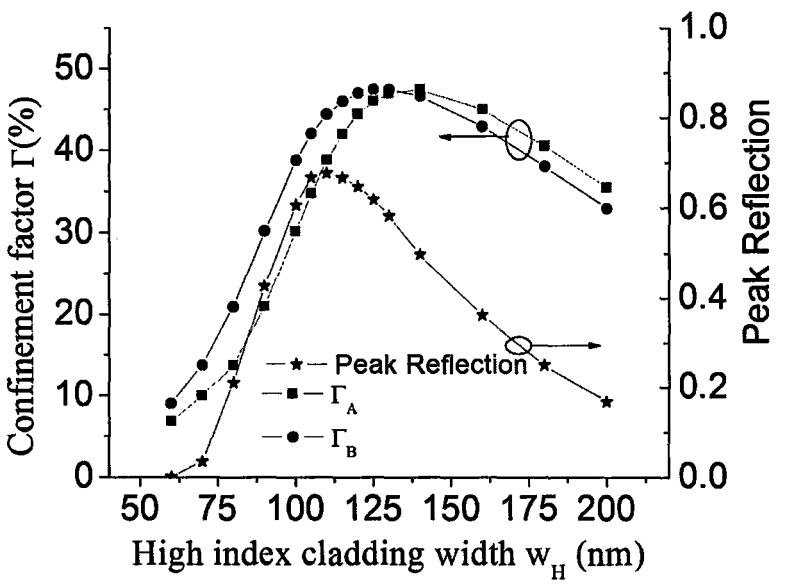

Figure 4.14. Peak reflection, confinement factors in the guiding region of section A and B as functions of high index cladding width w_{H1}. Solid square: confinement factor in section A; solid circle: confinement factor in section B; solid star: peak reflection.

It is observed that both the reflection and confinement factors increase as the width of the cladding increases when the width is relatively small (<110nm). They then reach their maximum values at a certain width and subsequently decrease with increasing the width of the high index cladding layer. These behaviors can be explained by the evolution of the power density distribution of the fundamental mode of the slot waveguide (section A) as a function of the cladding width as illustrated in Figure 4.15.

The power density distributions at three different high index cladding widths, i.e., w_{HI}=80nm, 120nm, 180nm, respectively, are displayed for the sake of comparison. It is noted that the power density is higher in the low-index slot region and also around the outer cladding interface where the gratings exist for w_H=120nm than those at w_H=80nm and 180nm, which also means greater confinement and reflection.

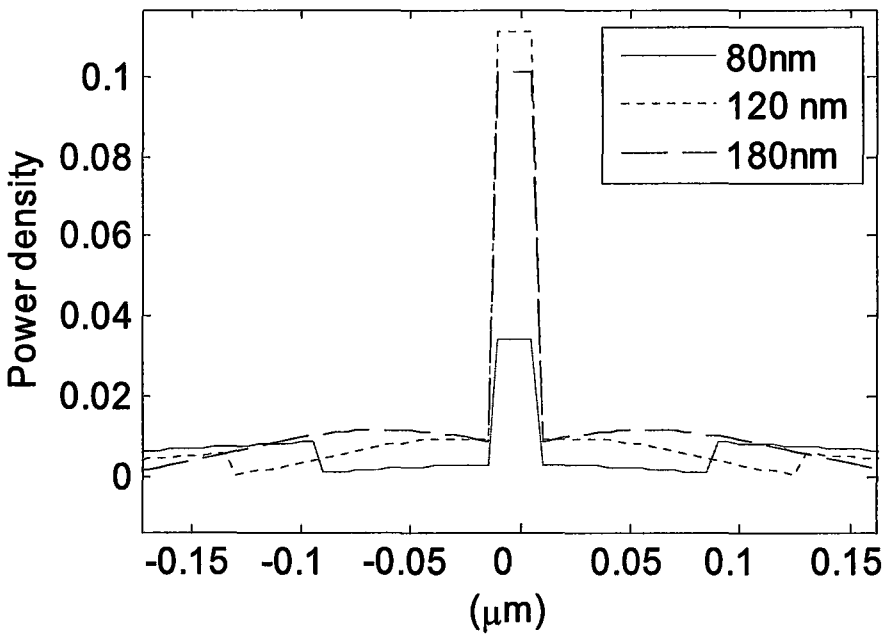

Figure 4.15. Power density distributions of the fundamental mode the slot waveguide for different widths of the high-index claddings. Solid line: w_{HI}=80nm; dotted line: w_{HI}=120nm; dash line: w_{HI}=180nm.

It is noted that the height of the corrugation 10nm in our simulation may be difficult to realize with current fabrication technology. As the objective of this work is to understand the underlying physics and hence the choice of such a parameter will not alter the conclusion drawn from the simulation and analysis. The characteristics of the

confinement factor and peak reflectivity as functions of the cladding widths have important bearing on the design of the Bragg grating structures in active devices such as distributed feedback (DFB) and distributed Bragg reflector (DBR) lasers and functional devices such as tunable optical filters and modulators.

D. Effect of the Grating Depth

Finally, we examine the effect of the grating depth, defined as the difference in widths for the high index cladding (Δw). We set the refractive index of the core n_L=1.0, the core width w_L=20nm, the high index cladding of section A w_{HI}=100nm, and 20 periods. The reflection spectra as a function of grating depth are shown in Figure 4.16.

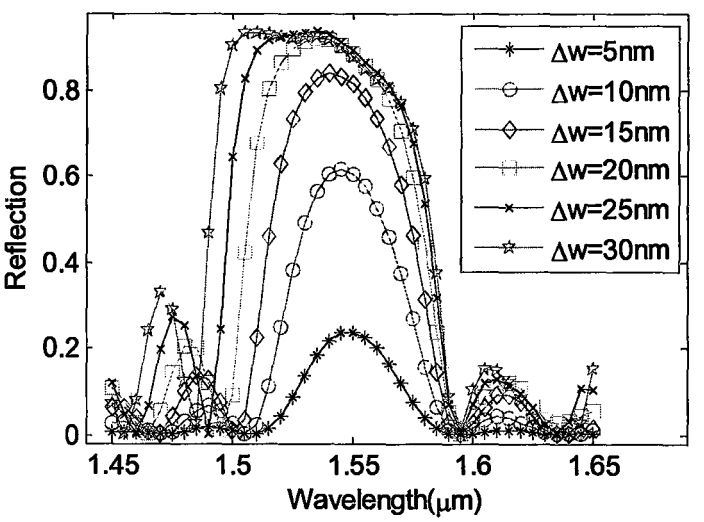

Figure 4.16. Reflection spectra of the slot waveguide grating with respect to core widths. Star: Δw=5nm; circle: Δw=10nm; diamond: Δw=15nm; square: Δw=20nm; cross: Δw=25nm; pentagram: Δw=30nm.

We observe that the peak reflection increases with the increase of grating depth, which is understood as the grating becomes stronger. In addition, the peak reflection

shifts towards the shorter wavelength as grating depth increases, which is different from the Bragg condition based on the fundamental mode of the slot waveguide. The shift of the reflection peak from the Bragg condition for strong gratings can be explained as follows: As the grating is weak, the fundamental harmonic wave, namely, Floquet mode, is dominant. Correspondingly, the Bragg wavelength corresponds to the peak of the reflection spectrum. As the grating becomes stronger, the roles of the high-order space harmonic waves and/or the radiative waveguide modes become more important. Physically, the interaction between the electromagnetic waves and the periodic grating structures is responsible for the coupling between the space harmonics of the guided and radiation modes. Accordingly, part of energy is stored in the vicinity of the grating interfaces. The reactive stored energy is responsible for the blue shift of the peak wavelength from the conventional Bragg wavelength.

Finally, it should be pointed out that the analysis is for TM modes only as these are the modes supported by the slot waveguides with relatively low loss. The TE modes are in general not supported by the same structures and therefore the waveguides are highly polarization dependent. Such polarization dependence may be beneficial or detrimental depending on the applications of the devices.

4.4.2 SPP insulator-metal-insulator grating

Miniaturization of guided-wave optical devices is crucial for building large-scale dense integrated photonic circuits. Surface plasmonic waveguides have been investigated intensively in recent years due to their ability to confine and guide electromagnetic waves in nano-structures at optical frequencies [76-81]. The surface plasma polariton (SPP) is a

type of electromagnetic wave which is bound to the metal-dielectric interface and decays exponentially from the interface into neighbouring media [82]. The non-radiative nature of the field makes possible concentrating and channeling light in a sub-wavelength scale, and the high surface sensitivity allows one to utilize the periodically modulated metallic surfaces to construct the photonic band gaps [83-85]. The uses of SPPs to realize low-loss Bragg gratings as a promising replacement of traditional dielectric gratings which are widely used in distributed feedback (DFB) and distributed Bragg reflector (DBR) lasers have been investigated both theoretically and experimentally[86-89].

The published Bragg waveguide gratings could be grouped into two classes regarding the cross section of the waveguide structures, namely, insulator-metal-insulator (IMI) [86, 89, 90], and metal-insulator-metal (MIM)[87, 88]. It is a well known fact that there exists a trade-off between the confinement and the loss. In this respect, MIM structures provide higher confinement whereas IMI structures give rise to longer propagation length. However, the proposed IMI waveguides are by corrugated metallic strip width or thickness, the reflectivity is usually very weak for small corrugation and high loss is expected as the corrugation is aggrandized.

Alternative structures to realize IMI Bragg waveguide gratings were proposed and demonstrated in ref[91, 92]. The type of structures consists of alternatively stacked IMI waveguides with different dielectric materials. The low absorption loss is expected for this structure as the coupling between nearby sections can be adjusted by varying the dielectric materials. The anomalous transmission behaviours on specific wavelengths has been investigated by coupled wave method[91]. The similar configuration used as TM-

pass/TE-stop polarizer has been studied in reference [92]. In this work, the potential application of the structure in distributed feedback (DFB) and distributed Bragg reflector (DBR) lasers has been investigated theoretically.

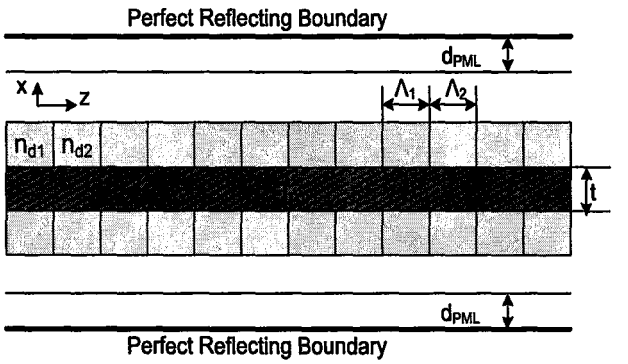

Figure 4.17. Sketch of the computation window, the studied structure is enclosed by perfectly matched layers terminated by perfectly reflecting boundaries (PRB).

The waveguide grating is modeled as a periodic structure with a unit cell consisting of two IMI waveguide sub-sections of different dielectric claddings (Figure 4.17). The thickness and the refractive indexes of the metal and two upper and lower claddings are denoted by t, n_m, n_{d1}, and n_{d2}, respectively. The section lengths are represented by Λ_1 and Λ_2, respectively. The waveguide parameters in our simulation are chosen as follows: the refractive index of the metal is $n_m = 0.558 - j9.81$ (gold) and the desired central wavelength is λ_0=1550nm. The section lengths and the target central wavelength are related by the Bragg conditions as follows:

$$\Lambda_{1,2} = \frac{\lambda_0}{4\,\mathrm{Re}\left(Neff_{1,2}\right)} \tag{4.27}$$

where $Neff_{1,2}$ are the effective indices of the fundamental local modes in the two sub-sections.

The grating structure is investigated by the complex mode matching method in which the computation domain is enclosed by perfectly matched layers (PML) terminated by perfect reflecting boundary.

We first study the dependence of the power reflectivity, transmittivity, and loss as the functions of the metallic strip thickness. The computation parameters used in the simulation are as follows: the refractive index of the dielectric claddings are n_{d1}=1.44 and n_{d2}=1.46, respectively. The computation window is 5.0 μ m, the thickness of PML is 0.5 μ m for each side. The number of periods is 50.

The reflection, transmission and loss spectra are calculated and displayed in Figure 4.18 as a function of metallic strip thickness. Three different metallic strip thicknesses, t =10nm, 20nm, and 30nm are examined. It is observed that the peak reflection and the transmission pit decrease with the increase of the thickness of the strip. The reason for the increase in peak reflectivity for thinner metal thickness is that the field penetration into the dielectric medium is enhanced as the thickness of the metallic strip decreases, which leads to an increase of the modal mismatching between the sections. In the meanwhile, the absorption loss is reduced as a consequence of the reduced metal thickness.

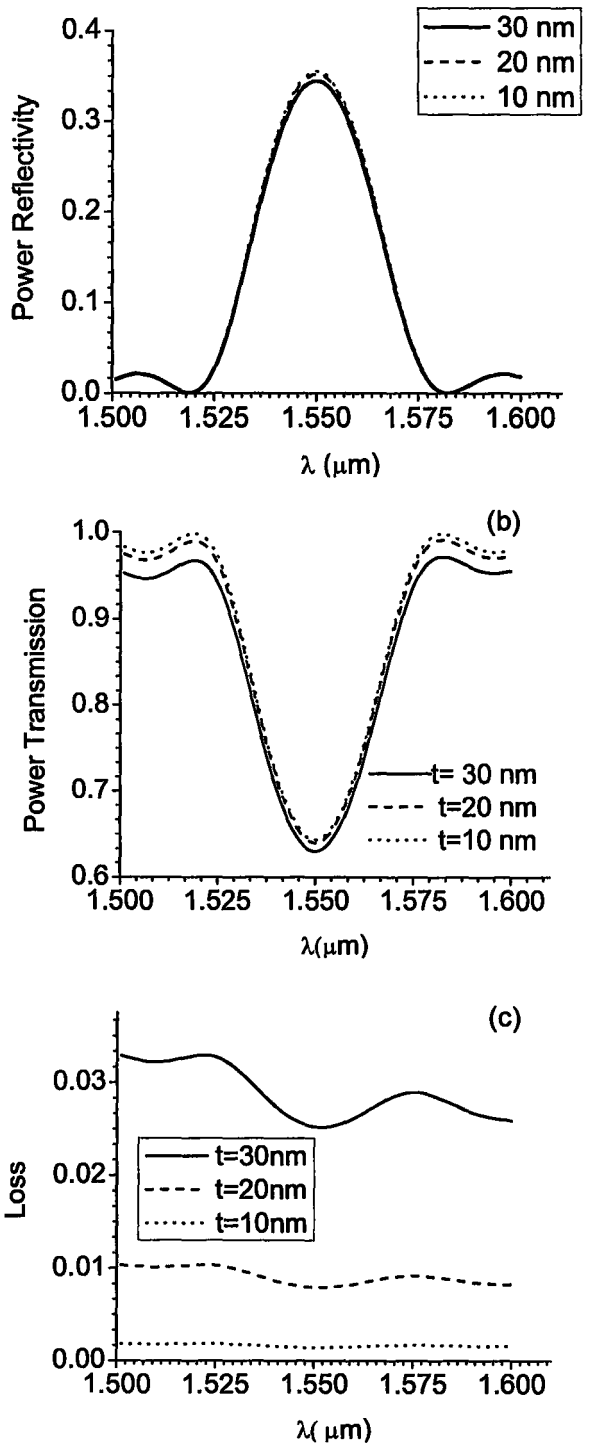

Figure 4.18. Reflection, transmission, and loss spectra of the SPP waveguide grating, solid line: t=30nm; dash: t=20nm; dot: t=10nm.

Next, we investigate the effect of the refractive index difference between the dielectric media on the reflection and transmission spectra on the gratings. The parameters used in the simulation are: t=30nm, n_{d1}=1.44, and n_{d2}=1.46, 1.48 and 1.50. The number of periods remains 50.

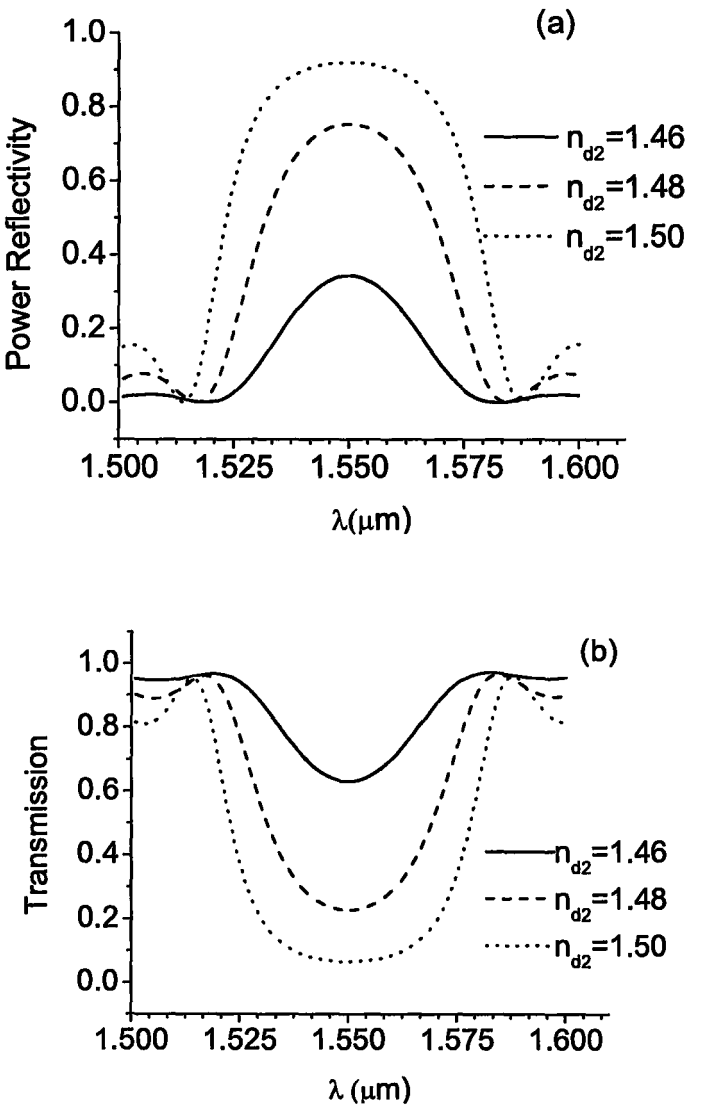

Figure 4.19. Reflection and transmission spectra of the SPP waveguide grating, solid line: n_{d2}=1.45; dash: n_{d2}=1.48; dot: n_{d2}=1.50.

The reflection and transmission spectra for different dielectric materials are shown in Figure 4.19. We observe that the peak reflection increases with the increase of refractive index difference, which is understood as the grating becomes stronger. In addition, the peak reflection shifts towards the shorter wavelength as grating depth increases, which is different from the Bragg condition based on the fundamental mode calculation.

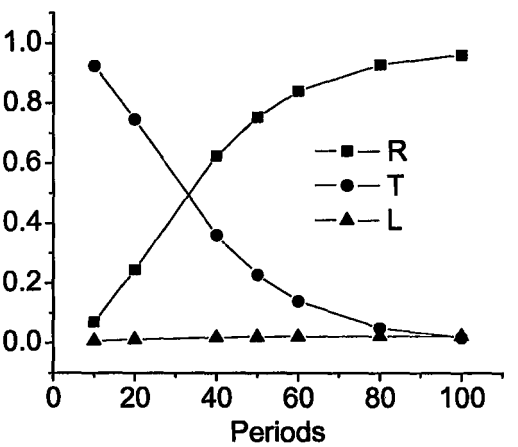

Figure 4.20. Reflection (R), transmission (T), and loss (L) as a function of period numbers.

We also investigate reflection, transmission and loss for the proposed grating at the central wavelength (1.55 μm) at which the reflection reaches its maximum. The parameters used in the simulation are: the thickness of the core is t=30nm, the refractive indices are n_{d1}=1.44, n_{d2}=1.48, the number of periods ranges from 10 to 100. The simulation result is shown in Figure 4.20. It is seen that the reflection increases while the transmission decreases with the period number as expected. On the other hand, it is observed that the loss changes only slightly and remains very low.

To further illustrate the performance of the proposed structure, we compare the reflection and the loss of the current structure with the SPPs ridge grating structure[90]. The ridge grating (Figure 4.21) consists of metal film (t = 20 nm, h=30nm) surrounded by the dielectric medium (n_d =1.44).

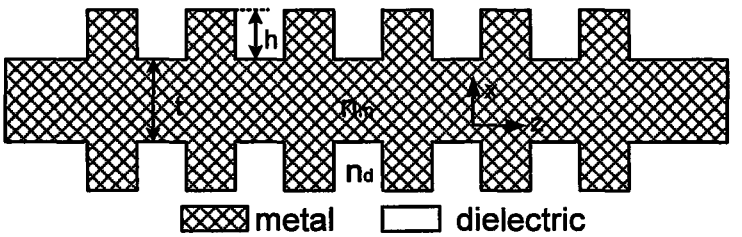

Figure 4.21. Spp Ridge grating

For comparison, the parameters of the structure are given by: n_{d1} =1.44 and n_{d2} =1.46, t =20nm. The number of periods used is 50 for both structures. The calculated spectrum of reflection and loss are shown in Figure 4.22. The confinement of both gratings is expected to be almost the same since they are both IMI structures. It is observed that the peak reflection of the current structure is larger than the ridge grating, and moreover, it is noted the loss of the new structure is much less than that of the ridge grating in the literature.

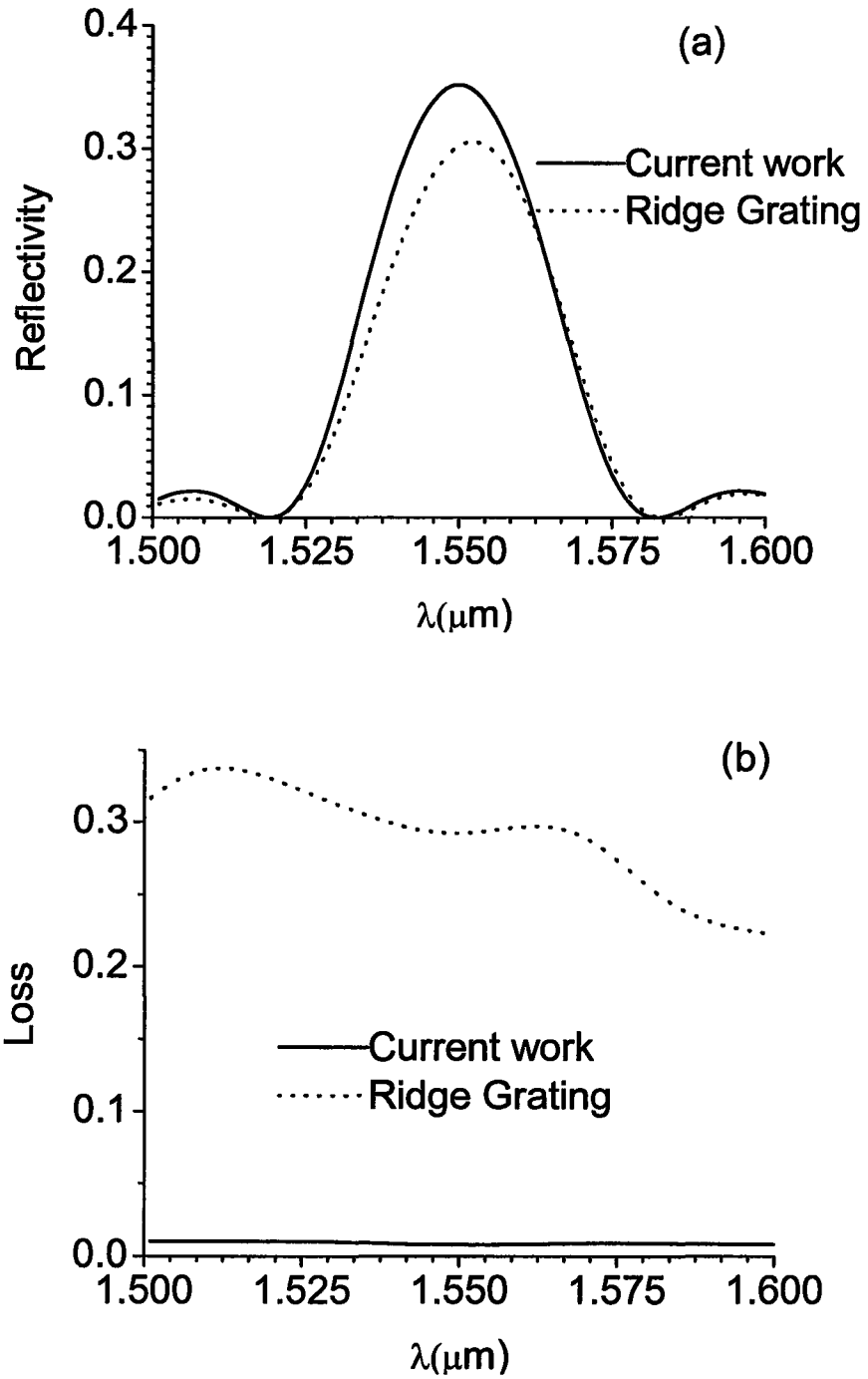

Figure 4.22: Reflection and loss spectra of the SPP waveguide grating, solid line: Current structure; dash: Ridge grating reference [90] .

4.4.3 Bragg grating with gapped nano-metallic strips

In this work, we propose and analyze a Bragg grating consisting of gapped nano-metallic strips embedded in InGaAsP/InP waveguide as shown in Figure 4.23.

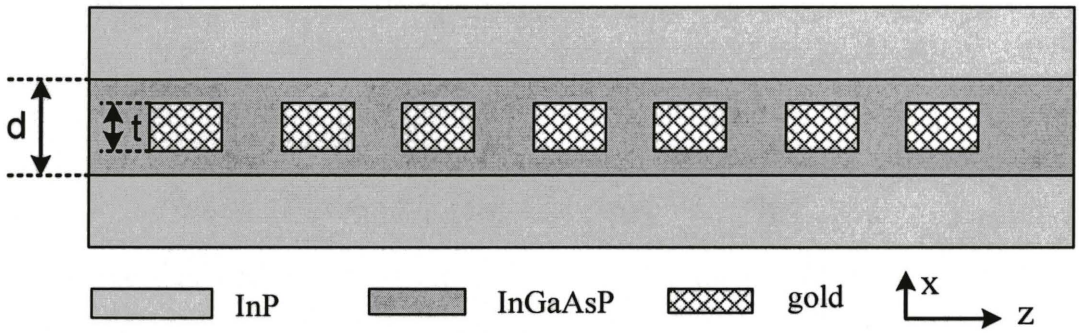

Figure 4.23. Geometry of Bragg grating with gapped nano-metallic strips

The geometry of the proposed waveguide grating is depicted in Figure 4.23: the gapped metallic strips (Au) are enclosed by InGaAsP; a lower index outer cladding (InP) is added to improve confinement of the electromagnetic waves. The modes of the waveguide structure with and without metallic strips have been examined by a finite difference method. The computation parameters used in the simulation are as follows: the refractive index of the inner cladding (InGaAsP) is set to 3.5 and that of the outer cladding (InP) is 3.17; the thickness of the inner cladding d is 0.3 μm; the computation window is 10.8μm with the 1 nm grid size; the thickness of PML is 0.5μm for each side and PML reflection is set to 1e-2; the metal film thickness t is set to 15nm with its length specified by the varying duty cycle in what follows; the working wavelength λ_0 =1550nm; the refractive index of the metal in this work is selected as gold with $n_m = 0.558 - j9.81$ and is assumed unchanged for a narrow wavelength region. The field patterns of the transverse section are shown in Figure 4.24.

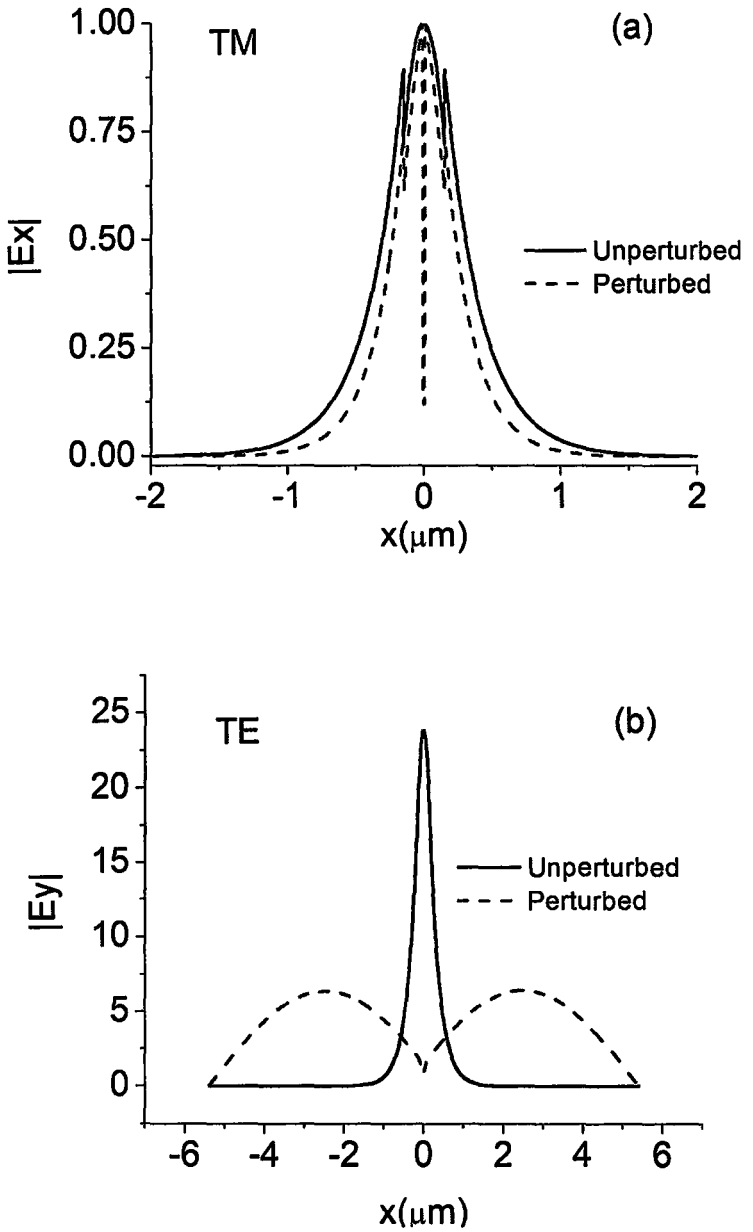

Figure 4.24. Field patterns of unperturbed and perturbed waveguide sections: (a) TM polarization; (b) TE polarization.

The grating is characterized by its compact size and applicable for both TE and TM waves. For the TM polarization, the structure is considered as an IMI SPP - dielectric

waveguide grating in which the wave coupling happens between the symmetric SPP mode in the IMI section and the guided TM mode in the dielectric waveguide section. The confinement is improved comparing to other types of IMI SPP gratings due to the "background" three-layer dielectric waveguide structure. For the TE polarization, the waveguide structure with the metallic strip (i.e., the IMI) section does not support any guided mode. As a result, the wave interaction happens between the guided TE mode in the dielectric waveguide section and the radiation modes in the IMI section. By adjusting the grating duty cycle (i.e., the metallic strip length inside each grating period), well-behaved spectral characteristics are observed.

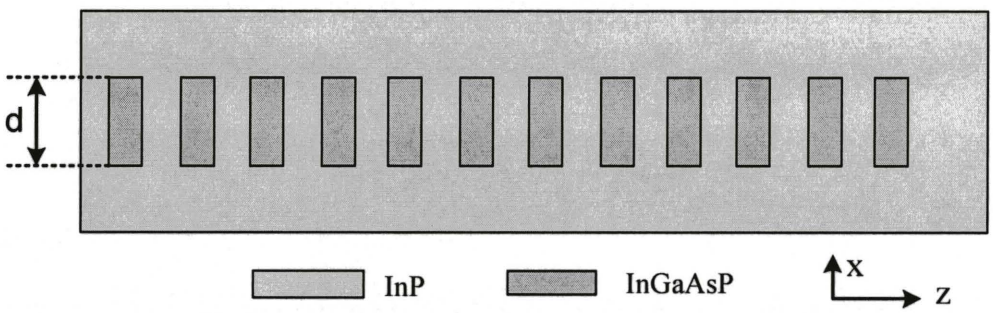

Figure 4.25. Schematic of a deep etched grating.

It is noted that the deep-etched grating as shown in Figure 4.25 is commonly used to construct compact Bragg gratings. Hence it is beneficial to evaluate the performance of our proposed structure through the comparison with the deep-etched grating.

The two structures share the similarity on TE waves as the coupling between confined and radiation modes happens in both structures. In light of suppression the radiation loss, a small duty cycle (i.e., a shorter IMI section) is preferred. For TM waves, however, unlike in the deep-etched grating where the coupling is still between the

confined and radiation modes, the wave interaction in our proposed structure happens between the confined mode in the dielectric waveguide section and the symmetric SPP mode in the IMI section, which is shown by our numerical analysis to have a reduced reflection spectral bandwidth at comparable peak reflections.

For the TM polarization, the existence of the metal structure at the center of the waveguide gives rise to the SPP mode supported by the metal, which leads to perturbation of the field locally near the center of the waveguide as illustrated in Figure 4.24 (a). Assuming that the input/output sections of the grating are single mode waveguide structures without the perturbations, the grating subsection lengths $\Lambda_{\text{unperturbed}}$ and $\Lambda_{\text{unperturbed}}$ are determined by Bragg condition

$$\Lambda_{\text{unperturbed}} = (1-\zeta)\cdot\frac{\lambda}{2\,\text{Re}\left(Neff_{\text{unperturbed}}\right)} \tag{4.28}$$

$$\Lambda_{\text{perturbed}} = \zeta\cdot\frac{\lambda}{2\,\text{Re}\left(Neff_{\text{perturbed}}\right)} \tag{4.29}$$

where ζ denotes the duty cycle, and $Neff_{\text{unperturbed}}$, $Neff_{\text{perturbed}}$ represent the effective indices of the mode with the lowest propagation loss in unperturbed and perturbed waveguide section, respectively.

We first calculated the reflectivity and loss spectra of a 30 μm-long waveguide grating with nano-metallic structure for TM and TE modes for different duty cycles as shown in Figure 4.26. It is observed that the proposed structure can be potentially designed for both TE and TM polarizations. For TM case, the higher peak reflection happens at ζ=0.5; on the contrary, higher peak reflection is observed at smaller duty

cycle (ζ=0.1) for TE mode. The seeming paradox is explained by the higher radiation loss existed in larger duty cycles for TE polarizations.

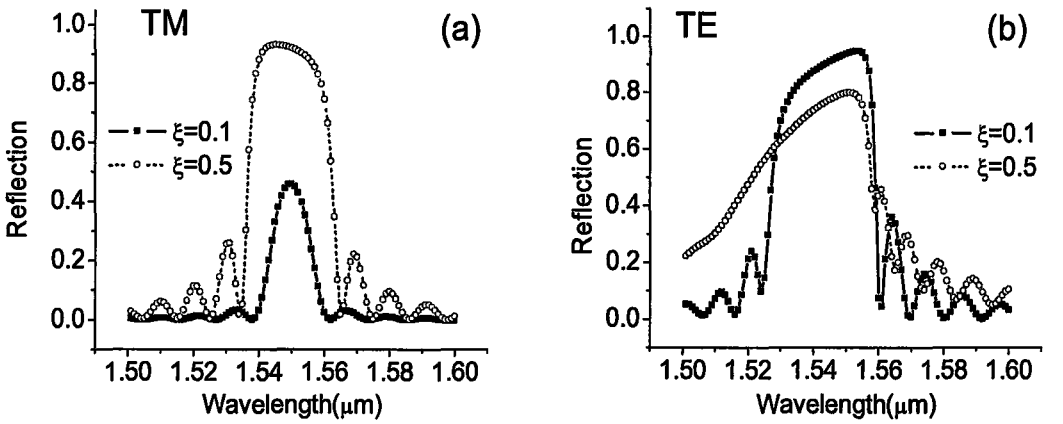

Figure 4.26. Reflection spectra of a 24 μm-long waveguide grating with nano-metallic structure (a) TM (b) TE.

To disclose the impact of the duty cycles on the performance and reveal the discrepancies between the current structure and the deep-etched grating structure, we examine the merits and drawbacks of the two structures through the comparison on the key parameters such as peak reflectivity, loss at the peak reflection wavelength, loss at reflection half bandwidth, reflection bandwidth, etc. To be comparable, the deep-etched grating is formed by corrugating throughout the core (InGaAsP) and filled with the same materials as the cladding medium (InP). Moreover, the lengths of the two gratings are fixed to 30μm.

The peak reflection, the loss at the peak reflection wavelength, the loss at the reflection half bandwidth, and the reflection bandwidth as functions of duty cycles for TE polarizations are shown in Figure 4.27.

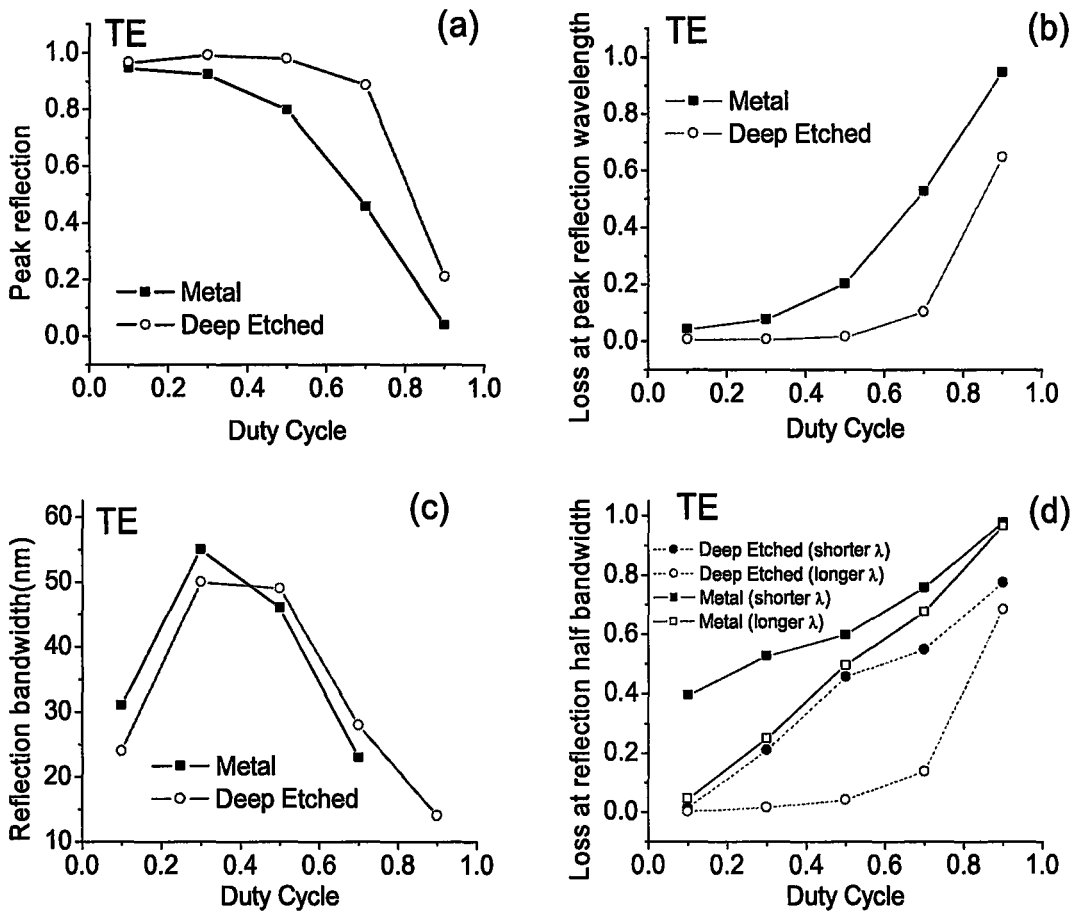

Figure 4.27. Spectral characteristics (TE) as a function of duty cycles for the proposed grating and the deep-etched grating: (a) peak reflection; (b) loss at the peak reflection wavelength; (c) loss at the reflection half bandwidth; (d) reflection bandwidth.

It is observed that strong backward couplings happen in both gratings and high peak reflection appears even in small duty cycles. On the other hand, the loss at the peak reflection wavelength as well as the loss at the reflection half bandwidth increases with the duty cycle in both gratings. As a result, peak reflection is dramatically reduced with the increase of the duty cycle. The bandwidths of the two gratings vary in the same trend

while the deep-etched grating prevails. The decreasing of the bandwidth for larger duty cycles (ξ>0.3) is explained by the diminishing of the peak reflection.

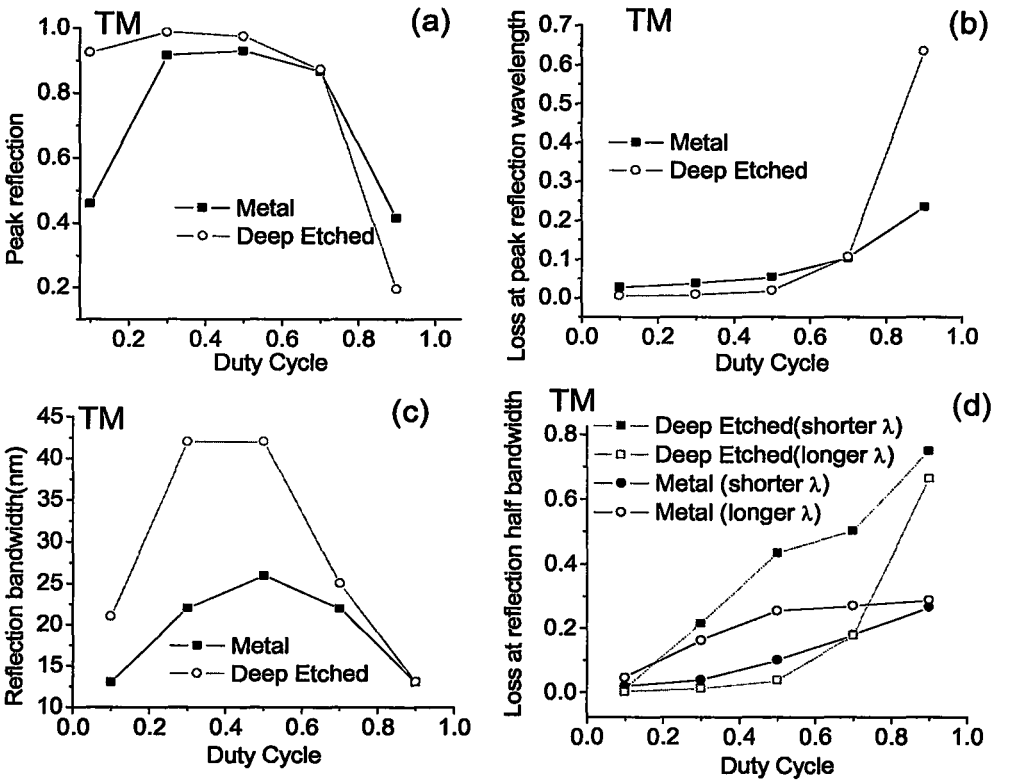

Figure 4.28. Spectral characteristics (TE) as a function of duty cycles for the proposed grating and the deep-etched grating: (a) peak reflection; (b) loss at the peak reflection wavelength; (c) loss at the reflection half bandwidth; (d) reflection bandwidth.

The TM spectral responses of the proposed grating and deep-etched grating as functions of duty cycles are shown in Figure 4.28. It is illustrated that the loss at the peak reflection wavelength and the loss at the reflection half bandwidth increase with the duty cycle, however, the origins of loss in the two gratings are quite different: the

loss of the deep-etched grating mainly results from the radiation loss, whereas that of the proposed grating comes largely from the absorption loss of the metal. Since the metallic grating supports the low propagation loss symmetric SPP mode, noticeable smaller loss of metallic grating is demonstrated for larger duty cycles comparing to that of the deep-etched grating. Further, the guide TM mode/SPP mode coupling in proposed grating also leads to the nearly symmetric peak reflection and reflection bandwidth with complementary duty cycles as shown in

Figure 4.28 (a) and Figure 4.28(c), respectively. It is found that the peak reflections in the range from ζ=0.3 to ζ=0.7 are quite close for both gratings; however, the proposed grating has the conspicuous narrower bandwidth.

4.5 Summary

In this Chapter, a complex mode matching method has been described and verified by examples of facet reflectivity and polarization rotators. The proposed method then has been applied to investigate the characteristics of waveguide grating structures based on slot waveguide, spp waveguide etc.

Chapter 5 Complex Coupled Mode Theory Based on Normal Modes

5.1 Introduction

Though the coupled-mode theory (CMT) has been widely applied as an analytical approach for analysis of wave propagation and field interaction in optical waveguides, the classical coupled-mode theory has been challenged by non-guided radiation fields due to the continuous spectrum of radiation modes. In the previous chapter, a mode matching method based on perfectly matched layers terminated by perfectly reflection boundaries has been introduced to cope with radiation fields. This approach is less appealing to the coupled-mode theory as a large number of modes undermine the benefits of the theory in the first place.

In this chapter, within the framework of PML and PRB computation model, we develop the coupled mode theory based on the complex modes and apply it to investigate the radiation coupling in short/long period gratings and waveguide taper structures.

5.2 Derivation of Complex Coupled Mode Equations

To derive the coupled-mode equations based on the complex modes described in Section 2, we assume that the permittivity function distribution along the waveguide with perturbations can be expressed as

$$\tilde{\varepsilon}(x,y,z)=\varepsilon(x,y)+\Delta\varepsilon(x,y,z) \tag{5.1}$$

where the index perturbation $\Delta\varepsilon$ is defined as the difference between the index profiles

of the practical waveguides under investigation and the reference waveguides for which the complex modes are known. Maxwell's equations for the perturbed waveguides are

$$\nabla \times \mathbf{E}(x,y,z) = -j\omega\mu_o \mathbf{H}(x,y,z) \tag{5.2}$$

$$\nabla \times \mathbf{H}(x,y,z) = +j\omega\tilde{\varepsilon}(x,y,z)\mathbf{H}(x,y,z) \tag{5.3}$$

Suppose that the difference between the perturbed and the reference waveguides is sufficiently small so that we can expand the unknown transverse electromagnetic fields of the perturbed waveguides in terms of the transverse modal fields of the reference waveguides, i.e.,

$$\mathbf{E}_t(x,y,z) = \sum_{n=1} \left[a_n(z) + b_n(z)\right] \mathbf{e}_{tn}(x,y) \tag{5.4}$$

$$\mathbf{H}_t(x,y,z) = \sum_{n=1} \left[a_n(z) - b_n(z)\right] \mathbf{h}_{tn}(x,y) \tag{5.5}$$

The functions $a_n(z)$ and $b_n(z)$ are the mode amplitudes for the forward and backward propagating waves, respectively. The longitudinal fields can be expressed in terms of transverse components as

$$\mathbf{E}_z(x,y,z) = \sum_{n=1} \left[a_n(z) - b_n(z)\right] \frac{\varepsilon}{\tilde{\varepsilon}} \mathbf{e}_{zn}(x,y) \tag{5.6}$$

$$\mathbf{H}_z(x,y,z) = \sum_{n=1} \left[a_n(z) + b_n(z)\right] \mathbf{h}_{zn}(x,y) \tag{5.7}$$

The next step is to derive the coupled-mode equations governing the mode amplitudes. To do so, we simply substitute eqs. (5.4)-(5.7)into(5.2)-(5.3). After mathematical manipulations, we derive the following coupled equations:

$$N_m \frac{da_m}{dz} + j\gamma_m a_m = -j\sum_{n=1} \kappa_{mn} a_n - j\sum_{n=1} \chi_{mn} b_n \tag{5.8}$$

$$N_m \frac{db_m}{dz} - j\gamma_m b_m = +j\sum_{n=1} \kappa_{mn} b_n + j\sum_{n=1} \chi_{mn} a_n \tag{5.9}$$

in which the coupling coefficients are given by

$$\kappa_{mn} = \frac{\omega\varepsilon_o}{4} \int_A \left(\tilde{n}^2 - n^2\right)\left(\mathbf{e}_{tn} \cdot \mathbf{e}_{tm} - \frac{n^2}{\tilde{n}^2} e_{zn} \cdot e_{zm}\right) da \tag{5.10}$$

$$\chi_{mn} = \frac{\omega\varepsilon_o}{4} \int_A \left(\tilde{n}^2 - n^2\right)\left(\mathbf{e}_{tn} \cdot \mathbf{e}_{tm} + \frac{n^2}{\tilde{n}^2} e_{zn} \cdot e_{zm}\right) da \tag{5.11}$$

where the refractive indices are used to replace the permittivity functions, i.e., $\varepsilon = n^2\varepsilon_o$ and $\tilde{\varepsilon} = \tilde{n}^2\varepsilon_o$. The coefficient N_m is defined as

$$N_m = \frac{1}{2} \iint \left(\mathbf{e}_{tm} \times \mathbf{h}_{tm}\right) \cdot \hat{\mathbf{z}} da \tag{5.12}$$

Under the normalization condition (13), $N_1 = 1$ for the real core guided modes and $N_m \cong 1$ for the complex cladding leaky modes with relatively small mode losses. In general, however, N_m may not be equal to unity and can be complex.

The coupled-mode equations (5.8)-(5.9) and the expressions for the coupling coefficients (5.10)-(5.11) are formally identical to those derived for guided modes in waveguides made of reciprocal media in presence of loss and/or gain and hence can be solved by the same analytical and numerical techniques as previously done in literature. In the classical coupled-mode theory, to deal with radiation fields based on the integral of the continuous radiation modes is possible but extremely cumbersome. On the other hand,

however, both guided and radiation fields are considered in the new complex coupled-mode theory in a unified fashion. Also, it is noted that the coupling coefficients for the co- and contra-coupling modes are symmetrical in the sense that

$$\kappa_{mn} = \kappa_{nm} \tag{5.13}$$

$$\chi_{mn} = \chi_{nm} \tag{5.14}$$

Further, we may rewrite the mode amplitudes by separating the slowly varying envelopes with the fast oscillating carriers so as to

$$a_n = A_n \exp(-j\gamma_n z) \tag{5.15}$$

$$b_n = B_n \exp(+j\gamma_n z) \tag{5.16}$$

On substitution of eqs. (19) by eqs. (23), we derive

$$N_m \frac{dA_m}{dz} = -j\sum_{n=1} \kappa_{mn} A_n \exp\left[-j(\gamma_n - \gamma_m)z\right] - j\sum_{n=1} \chi_{mn} B_n \exp\left[+j(\gamma_n + \gamma_m)z\right] \tag{5.17}$$

$$N_m \frac{dB_m}{dz} = +j\sum_{n=1} \kappa_{mn} B_n \exp\left[+j(\gamma_n - \gamma_m)z\right] + j\sum_{n=1} \chi_{mn} A_n \exp\left[-j(\gamma_n + \gamma_m)z\right] \tag{5.18}$$

For grating structures whose index perturbations are periodic along the waveguide axis, the coupling coefficients eqs. (5.10)-(5.11) are also periodic functions with the same period. We may expand the coupling coefficients in terms of Fourier series as

$$\kappa_{mn} = \sum_{l=-\infty}^{+\infty} D_{mn}^{(l)} \exp\left(jl\frac{2\pi}{\Lambda}z\right) \tag{5.19}$$

$$\chi_{mn} = \sum_{l=-\infty}^{+\infty} C_{mn}^{(l)} \exp\left(jl\frac{2\pi}{\Lambda}z\right) \tag{5.20}$$

Substitute eqs. (5.19)-(5.20) into eqs.(5.17)-(5.18) and we derive

$$N_m \frac{dA_m}{dz} = -j\sum_{n=1} A_n \sum_{l=-\infty}^{+\infty} D_{mn}^{(l)} \exp\left[-j\left(\gamma_n - \gamma_m - l\frac{2\pi}{\Lambda}\right)z\right] -j\sum_{n=1} B_n \sum_{l=-\infty}^{+\infty} C_{mn}^{(l)} \exp\left[+j\left(\gamma_n + \gamma_m + l\frac{2\pi}{\Lambda}\right)z\right] \quad (5.21)$$

$$N_m \frac{dB_m}{dz} = +j\sum_{n=1} B_n \sum_{l=-\infty}^{+\infty} D_{mn}^{(l)} \exp\left[+j\left(\gamma_n - \gamma_m + l\frac{2\pi}{\Lambda}\right)z\right] +j\sum_{n=1} A_n \sum_{l=-\infty}^{+\infty} C_{mn}^{(l)} \exp\left[-j\left(\gamma_n + \gamma_m - l\frac{2\pi}{\Lambda}\right)z\right] \quad (5.22)$$

It can be shown that the phase factors $\gamma_n - \gamma_m \pm l2\pi/\Lambda$ and $\gamma_n + \gamma_m \pm l2\pi/\Lambda$ in the exponential terms in eqs. (5.21)-(5.22)are most critical in determining the strength of interactions between the different modes over distance. Only when these factors are close to zero there will be appreciable power exchange between the coupled modes, a condition referred to as the phase-matching conditions. In fact, the role of grating is to facilitate the phase matching between two propagation modes with different propagation constants by providing a grating space harmonic component related to the grating period and profile. Note that the phase matching conditions for the co- and contra-propagating modes are quite distinct and may not be readily realized by the same grating. In practice, we normally design the grating to assist coupling for either contra-propagating (e.g., Bragg gratings) or co-propagating (e.g., long-period gratings) waves only. Under this assumption, the coupled mode equations are further reduced to two groups as described below.

For the contra-propagation waves, the coupled-mode equations reduce to

$$N_m \frac{dA_m}{dz} = -j\sum_{n=1} B_n \sum_{l=-\infty}^{+\infty} C_{mn}^{(l)} \exp\left[+j\left(\gamma_n + \gamma_m + l\frac{2\pi}{\Lambda}\right)z\right] \quad (5.23)$$

$$N_m \frac{dB_m}{dz} = +j\sum_{n=1} A_n \sum_{l=-\infty}^{+\infty} C_{mn}^{(l)} \exp\left[-j\left(\gamma_n + \gamma_m - l\frac{2\pi}{\Lambda}\right)z\right] \tag{5.24}$$

and for the co-directional propagation waves, we have

$$N_m \frac{dA_m}{dz} = -j\sum_{n=1} A_n \sum_{l=-\infty}^{+\infty} D_{mn}^{(l)} \exp\left[-j\left(\gamma_n - \gamma_m - l\frac{2\pi}{\Lambda}\right)z\right] \tag{5.25}$$

$$N_m \frac{dB_m}{dz} = +j\sum_{n=1} B_n \sum_{l=-\infty}^{+\infty} D_{mn}^{(l)} \exp\left[+j\left(\gamma_n - \gamma_m + l\frac{2\pi}{\Lambda}\right)z\right] \tag{5.26}$$

Further, for a given grating, the phase matching condition is a function of wavelength through wavelength dependence of the mode propagation constants, i.e., $\gamma_n(\lambda)$ and $\gamma_m(\lambda)$. It also depends on the mode index ($m,n = 1,2,...$) and the order of space harmonics in the Fourier expansion ($l = -\infty,...+\infty$). Any combination of these parameters that lead to a phase matching condition will likely yield a distinct resonant signature in the mode coupling as illustrated later in the transmission and reflection spectra in this paper. By identifying these phase matching conditions in the coupled- mode equations, we can greatly simplify the solutions and also gain great insight into the salient features underlying the interaction of the modes in presence of the gratings.

First of all, we may consider only the largest Fourier expansion coefficient, i.e., $l = \pm 1$ or the 1st-order grating effect and ignore all these other high-order space harmonics. Investigation of the higher-order gratings can be performed in the similar fashion, but will not be pursued further in this work. The coupled-mode eqs (5.23)-(5.26) are subsequently decoupled into two separate sets such that

$$N_m \frac{dA_m}{dz} = -j\sum_{n=1} B_n C_{mn}^{(-1)} \exp\left[+j\left(\gamma_n + \gamma_m - \frac{2\pi}{\Lambda}\right)z\right] \tag{5.27}$$

$$N_m \frac{dB_m}{dz} = +j\sum_{n=1} A_n C_{mn}^{(+1)} \exp\left[-j\left(\gamma_n + \gamma_m - \frac{2\pi}{\Lambda}\right)z\right] \tag{5.28}$$

for the contra-directional propagation waves and

$$N_m \frac{dA_m}{dz} = -j\sum_{n=1} A_n D_{mn}^{(-1)} \exp\left[-j\left(\gamma_n - \gamma_m + \frac{2\pi}{\Lambda}\right)z\right] \tag{5.29}$$

$$N_m \frac{dB_m}{dz} = +j\sum_{n=1} B_n D_{mn}^{(+1)} \exp\left[+j\left(\gamma_n - \gamma_m + \frac{2\pi}{\Lambda}\right)z\right] \tag{5.30}$$

for the co-directional propagation waves.

In many practical situations, the phase matching conditions can only be realized at a distinct wavelength (i.e., λ_{mn}) for a given pair of modes (i.e., m and n). For the sake of simplicity, we suppose that the m-th mode is the forward propagating fundamental guided mode with largest real propagation constant, i.e., $m=1$ and $\gamma_m = \beta_1$ (real). In the proximity of the phase-matching wavelength $\lambda \cong \lambda_{1n}$, we may consider only the two modes that are close to the phase match (whenever it is possible!) so that eqs. (5.27)-(5.30) are simplified to

$$N_1 \frac{dA_1}{dz} = -jC_{1n}^{(-1)} B_n \exp\left[+j\left(\gamma_n + \beta_1 - \frac{2\pi}{\Lambda}\right)z\right] \tag{5.31}$$

$$N_n \frac{dB_n}{dz} = +jC_{n1}^{(+1)} A_1 \exp\left[-j\left(\gamma_n + \beta_1 - \frac{2\pi}{\Lambda}\right)z\right] \tag{5.32}$$

for the contra-directional propagation modes, and

$$N_1 \frac{dA_1}{dz} = -jD_{1n}^{(-1)} A_n \exp\left[-j\left(\gamma_n - \beta_1 + \frac{2\pi}{\Lambda}\right)z\right] \tag{5.33}$$

$$N_n \frac{dA_n}{dz} = -jD_{n1}^{(+1)} A_1 \exp\left[+j\left(\gamma_n - \beta_1 + \frac{2\pi}{\Lambda}\right)z\right] \tag{5.34}$$

for the co-directional propagating modes. Note that $\gamma_n = \beta_n - j\alpha_n$ and we define the phase detuning factors such that

$$\Delta\beta_n = \frac{1}{2}\left(\gamma_1 + \gamma_n - \frac{2\pi}{\Lambda}\right) \tag{5.35}$$

for the contra-directional propagation modes and

$$\Delta\beta_n = \frac{1}{2}\left(\gamma_1 - \gamma_n - \frac{2\pi}{\Lambda}\right) \tag{5.36}$$

for the co-directional propagation modes. The phase matching conditions happened as

$$\Re\left(\Delta\beta_n\right) = 0 \tag{5.37}$$

so that the grating period for the phase matching conditions for the contra- and co-directional modes are

$$\Lambda = \frac{2\pi}{\Re\left(\gamma_1 + \gamma_n\right)} \tag{5.38}$$

and

$$\Lambda = \frac{2\pi}{\Re\left(\gamma_1 - \gamma_n\right)} \tag{5.39}$$

We may recast eqs. (5.33)-(5.34)into more revealing forms as follows:

$$N_1 \frac{dA_1}{dz} = -jC_{1n}^{(-1)} B_n \exp\left[+j\left(2\Delta\beta_n\right)z\right] \tag{5.40}$$

$$N_n \frac{dB_n}{dz} = +jC_{n1}^{(+1)} A_1 \exp\left[-j\left(2\Delta\beta_n\right)z\right] \tag{5.41}$$

for the contra-directional modes and

$$N_1 \frac{dA_1}{dz} = -jD_{1n}^{(-1)} A_n \exp\left[-j\left(2\Delta\beta_n\right)z\right] \tag{5.42}$$

$$N_n \frac{dA_n}{dz} = -jD_{n1}^{(+1)} A_1 \exp\left[+j\left(2\Delta\beta_n\right)z\right] \tag{5.43}$$

for the co-directional modes.

5.3 Solutions of Complex Coupled Mode Equations

Computationally, we may solve the full coupled mode equations (5.27)-(5.30) (referred to as the full CMT) or the reduced eqs. (5.40)-(5.43)(referred to as the reduced CMT). The former can be readily carried out by a standard numerical algorithm such as the Ruga-Kutta method whereas the latter can be solved to yield simple analytical formulas.

Suppose that all the power is initially launched in the forward-propagating fundamental mode, i.e., $a_1(0)=1$. For the contra-directional modes, we assume that no power is associated with the backward-propagating modes at the other side of the grating, i.e., $b_n(L)=0$. The analytical solutions are

$$a_1(z)=a_1(0)\frac{\Delta\beta_n \sinh S(z-L)-jS\cosh S(z-L)}{-\Delta\beta_n \sinh SL-jS\cosh SL}e^{-j(\beta_1-\Delta\beta_n)z} \tag{5.44}$$

$$b_n(z)=-a_1(0)\frac{C_{n1}^{(+1)}}{N_n}\frac{\sinh S(z-L)}{\Delta\beta_n \sinh SL+jS\cosh SL}e^{j(\gamma_n-\Delta\beta_n)z} \tag{5.45}$$

where

$$S=\sqrt{\kappa_n^2-(\Delta\beta_n)^2} \tag{5.46}$$

$$\kappa_n=\sqrt{\frac{C_{1n}^{(-1)}C_{n1}^{(+1)}}{N_1N_n}} \tag{5.47}$$

For the co-directional modes, we assume that no power is associated with the secondary mode at the starting point of the grating, i.e., $a_n(0)=0\,(n\neq 1)$. The solutions are

$$a_1(z)=a_1(0)\frac{j\Delta\beta\sin(Q_nz)+Q_n\cos(Q_nz)}{Q_n}e^{-j(\beta_1-\Delta\beta_n)z} \tag{5.48}$$

$$a_n(z) = -je^{j\Delta\beta_n z}\frac{D_{n1}^{(+1)}}{N_n}\frac{\sin(Q_n z)}{Q_n}a_1(0)e^{-j(\gamma_n+\Delta\beta_n)z} \tag{5.49}$$

where

$$Q_n = \sqrt{\chi_n^2 + (\Delta\beta_n)^2} \tag{5.50}$$

$$\chi_n = \sqrt{\frac{D_{n1}^{(+1)}D_{1n}^{(-1)}}{N_n N_1}} \tag{5.51}$$

Note that the analytical solutions of the reduced coupled-mode equations are formally identical to those derived previously for real modes, except that the effective coupling coefficients κ_n (or χ_n) and the equivalent phase detuning factor $\Delta\beta_n$ may become complex.

Once we obtain the mode amplitudes, we will be able to calculate the guided powers carried by each of the modes. In general, the power flow along the waveguide is given as

$$P(z) = \frac{1}{2}\Re\iint_A \left[\mathbf{E}_t(x,y,z)\times\mathbf{H}_t^*(x,y,z)\right]\cdot\hat{z}da \tag{5.52}$$

By substitution of the field expansions in terms of the complex modes into eq.(5.52), we obtain

$$P(z) = \sum_{m=1}\sum_{n=1} M_{mn}\left[a_m a_n^* - b_m b_n^*\right] - \sum_{m=1}\sum_{n=1} N_{mn}\left[a_m b_n^* - b_m a_n^*\right] \tag{5.53}$$

where the first summation is for the power associated with the co-directional propagating modes in the forward and backward directions whereas the second summation is related to the power of the contra-directional propagating modes. The cross-power coefficients are defined as

$$M_{mn} = \frac{1}{4}\iint_A \left(\mathbf{e}_{tm} \times \mathbf{h}_{tn}^* + \mathbf{e}_{tn}^* \times \mathbf{h}_{tm}\right) \cdot \hat{z} da \tag{5.54}$$

$$N_{mn} = \frac{1}{4}\iint_A \left(\mathbf{e}_{tm} \times \mathbf{h}_{tn}^* - \mathbf{e}_{tn}^* \times \mathbf{h}_{tm}\right) \cdot \hat{z} da \tag{5.55}$$

Normally, the cross-power associated with the contra-directional modes is negligible in comparison with that with the co-directional modes and hence the second summation in eq. (45) may be ignored so that

$$P(z) \cong \sum_{m=1}\sum_{n=1} M_{mn}\left[a_m a_n^* - b_m b_n^*\right] \tag{5.56}$$

For the complex modes that are significant in the mode coupling process, the transverse fields are almost real and hence these modes are almost power orthogonal so that we may further approximate eq. (5.56) as

$$P(z) \cong \sum_{n=1}\left[|a_n|^2 - |b_n|^2\right] \tag{5.57}$$

Assume that the total power is launched into the forward propagating fundamental mode at the input. For the contra-directional mode coupling in Bragg grating, the total power at the input of the grating is therefore

$$P(0) = 1 - R(\lambda) \tag{5.58}$$

in which the total reflected power is expressed as

$$R(\lambda) \cong \sum_{m=1}\sum_{n=1} M_{mn} b_m(0) b_n^*(0) \tag{5.59}$$

and the mode indices m and n can not be equal to unity simultaneously. If we further neglect the cross-power associated with the co-directional propagating modes, i.e., $M_{mn} \cong 0$ and $M_{nn} \cong 1$, we have

$$R(\lambda) \cong \sum_{n=1} \left| b_m(0) \right|^2 \tag{5.60}$$

Similarly, if assume that at the output of the grating, no backward propagating modes exist. The total power at the output of the grating is

$$P(L) = \left| a_1(L) \right|^2 = T(\lambda) \tag{5.61}$$

The power conservation of the waveguide gratings calls for $P(0) = P(L)$, i.e.,

$$T(\lambda) = 1 - R(\lambda) \tag{5.62}$$

5.4 Applications of CMT in Bragg Reflectors

As an example for the application for the complex coupled-mode theory derived and solved in previous sections, we consider the volume Bragg gratings structure in Figure 5.1 in which the volume grating is placed in the core along the waveguide axis. The index perturbation of the grating is Δn, which is assumed to be small in comparison with the refractive index difference between the core and the cladding regions ($\Delta << n_{co} - n_{cl}$).

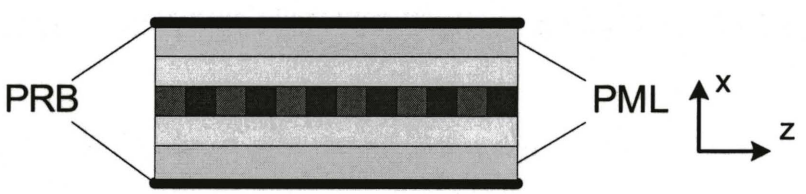

Figure 5.1. Volume Bragg grating structure based on slab waveguides

Other types of grating such as the corrugated surface gratings widely used in slab and rectangular waveguides can also be simulated by using the same formulations, but will not be examined without loss of generality. We assume that $\Delta n_{grating} = 9 \times 10^{-4}$ and $L = 800 \mu m$ and consider the following cases in our simulation.

5.4.1 Bragg gratings with lower index outer cladding ($n_s < n_{cl}$)

By considering the phase matching condition, we readily identify three distinct wavelengths corresponding to the Bragg conditions between the forward propagating fundamental mode and the first three backward propagating modes, respectively. Note that under this situation all modes are guided with real propagation constants and coupling coefficients so that the conventional CMT does apply. We subsequently calculated the coupling coefficients for these three pairs of mode coupling and show them in Figure 5.2(a). By applying the analytical solutions of the reduced coupled-mode theory around each of the phase matching wavelengths, we obtained the transmission spectra as indicated by the solid, dotted and dash lines in Figure 5.2 (a). It is observed that each of the phase-matching conditions produces a distinct dip in the transmission spectrum with magnitude proportional to the strength of the coupling coefficient $|\kappa_n|$. The entire transmission spectra may be obtained by first calculating the reflection spectra using the reduced coupled-mode theory near each of the phase matching points. The results are shown in Figure 5.2 (b) as dash lines. Also shown in the same figure are the results obtained by solving the full coupled-mode equations numerically with total of three modes and also by applying the rigorous mode-matching method (MMM) with total of 40

modes. The results of the reduced CMT, the full CMT and the rigorous MMM are all in good agreement, indicating that the reduced CMT is sufficient.

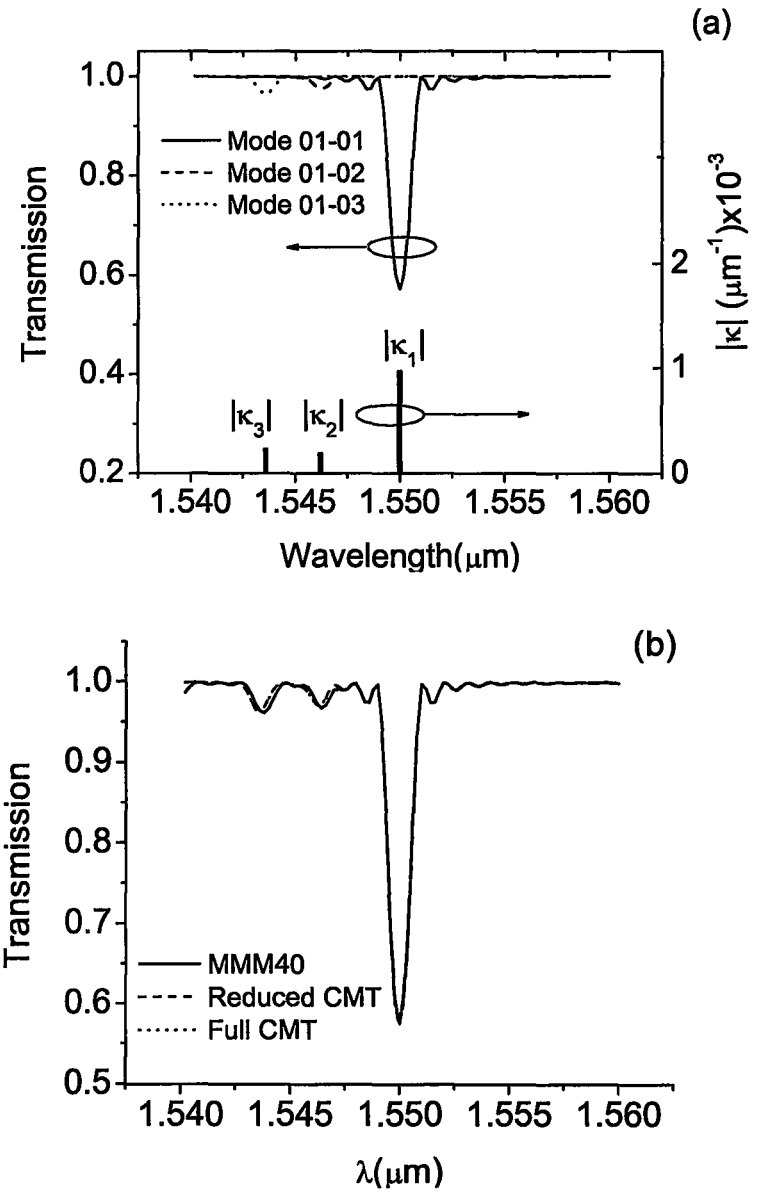

Figure 5.2. The transmission spectrum for Case A with lower outer cladding index n_s=1.0: (a) Solutions from the reduced CMT involving only two phase matching modes; (b) The transmission spectrum calculated by the reduced CMT (dash lines), the full CMT (dotted lines) and the rigorous MMM (solid lines).

5.4.2 Bragg gratings with equal index outer cladding ($n_s = n_{cl}$)

For the infinite cladding gratings ($n_s = n_{cl}$), the real, guided cladding modes evolve to complex quasi-leaky modes as well as PML modes. The latter plays negligible roles in the interactions with the grating-assisted couplings between the forward propagating guided mode and the backward propagating complex modes due to their huge mode losses and small mode overlaps with the guided modes in the core. For the quasi-leaky modes, however, the spectral spacing between them is too small and hence the phase-matching wavelengths are hardly distinguishable relative to the spectral width of each transmission dip as illustrated in Figure 5.3(a). Further, the coupling strengths $|\kappa_n|$ at these phase matching modes are similar.

The results by solving the full CMT with consideration for coupling from 1 to 10 backward propagating modes are illustrated in Figure 5.3(a). A flat overall drop in the transmission spectrum is predicted by considering all the relevant modes. The accuracy of the complex CMT involving 10 modes is verified by comparison with the results from the rigorous MMM with total of 60 modes as evident in Figure 5.3 (b). Shown on the same figure with dotted lines are results obtained using the reduced CMT considering only the phase-matched modes near the phase matching wavelengths.

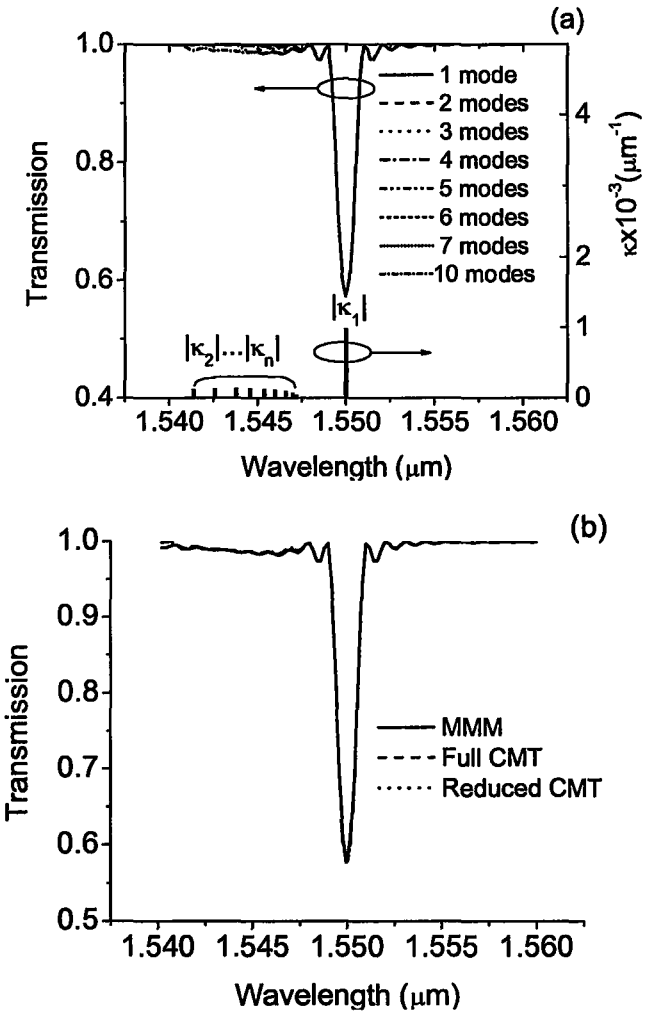

Figure 5.3: The transmission spectrum for Case B with equal outer cladding index n_s=1.450. (a) Phase matching wavelengths, corresponding coupling strengths, and the transmission spectrum predicted by the full CMT involving from 2 up to 11 modes; (b) The transmission spectrum calculated by the full CMT (dotted lines) and the rigorous MMM (solid lines).

It is indeed surprising to see that the simple solutions of the reduced CMT yield remarkably accurate results even under the situation in which the phase matching wavelengths are very close to each other. In comparison with the conventional coupled-mode theory which has to resort to either continuous radiation modes or large number of

box modes or tricky leaky modes, the complex coupled mode theory is much more straightforward in dealing with strong radiation fields in this case.

5.4.3 Bragg gratings with higher index outer cladding ($n_s > n_{cl}$)

If the refractive index of the outer cladding is higher than that of the cladding, the waveguide structure becomes leaky in the sense that no guided modes exist for mode index lower than the cladding index. We identify a total of seven (7) phase-matching modes and calculate the transmission spectrum by solving the full CMT considering coupling from 1 to 7 modes, respectively. In Figure 5.4(b), it shows the comparison between the full CMT (total of 7 modes), the reduced CMT (two modes near each phase-matching wavelengths) and the rigorous MMM (total of 60 modes), which are in excellent agreement with each other.

If we further increase the refractive index of the outer cladding (e.g., n_s=1.60 and n_s=1.90), the mode spacing becomes further apart and the phase-matching wavelengths more distinct as illustrated in Figure 5.5(a) and Figure 5.5(b), respectively. Also, the mode losses for the complex modes are in fact smaller due to the reflection from the interface of the cladding and outer cladding and coupling strengths vary more significantly from mode to mode. All these lead to the transmission spectra with highly visible resonance dips as evident in Figure 5.5 (a) and Figure 5.5 (b). The comparison between the full complex CMT with total of 4 modes, the reduced CMT with two modes for each of the phase-matching wavelengths and the rigorous MMM with total of 60 modes shows excellent agreement.

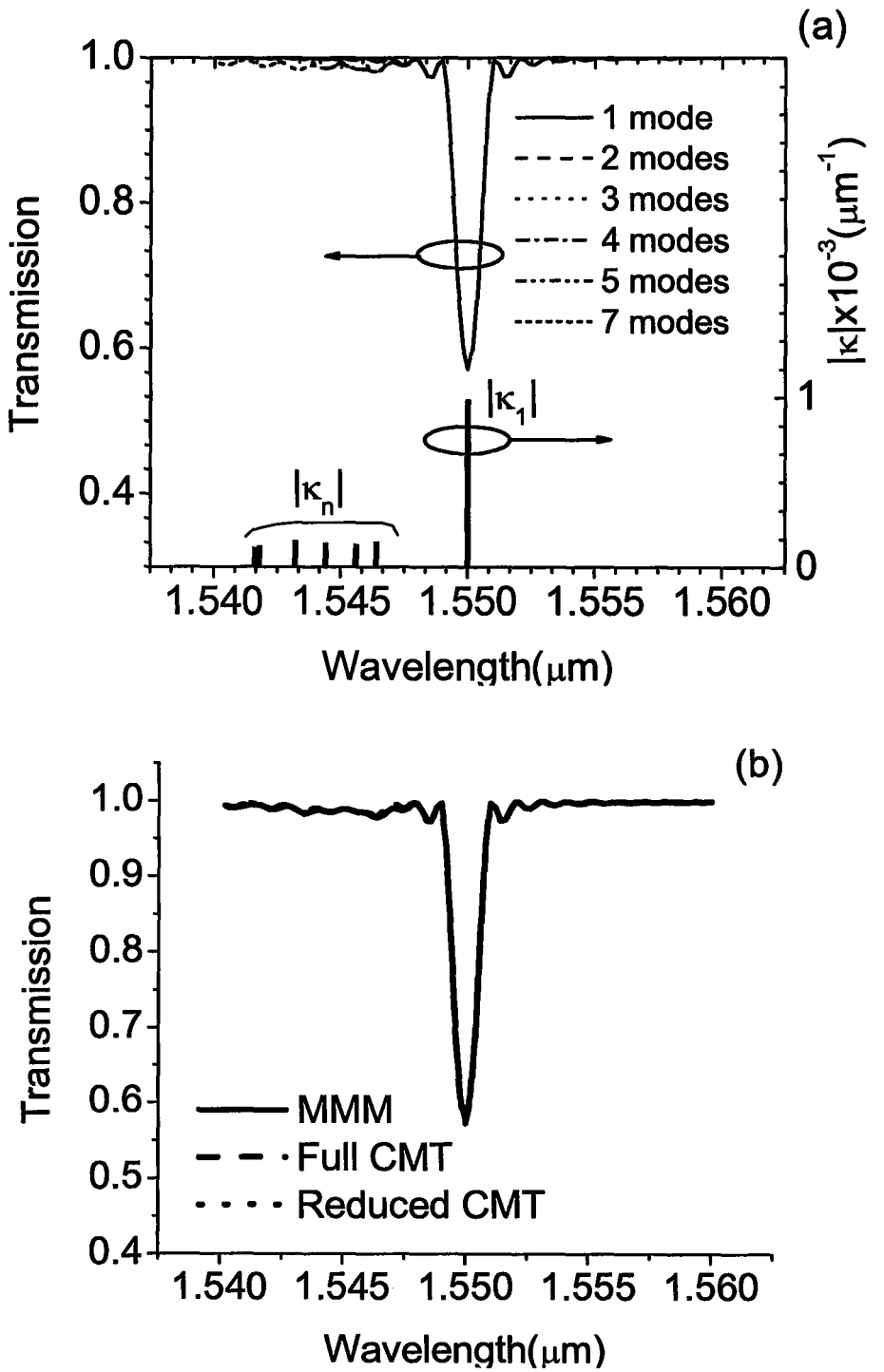

Figure 5.4. Transmission spectra with index of the outer cladding n_s slightly larger than the index of the inner cladding n_{cl} (n_s=1.455).

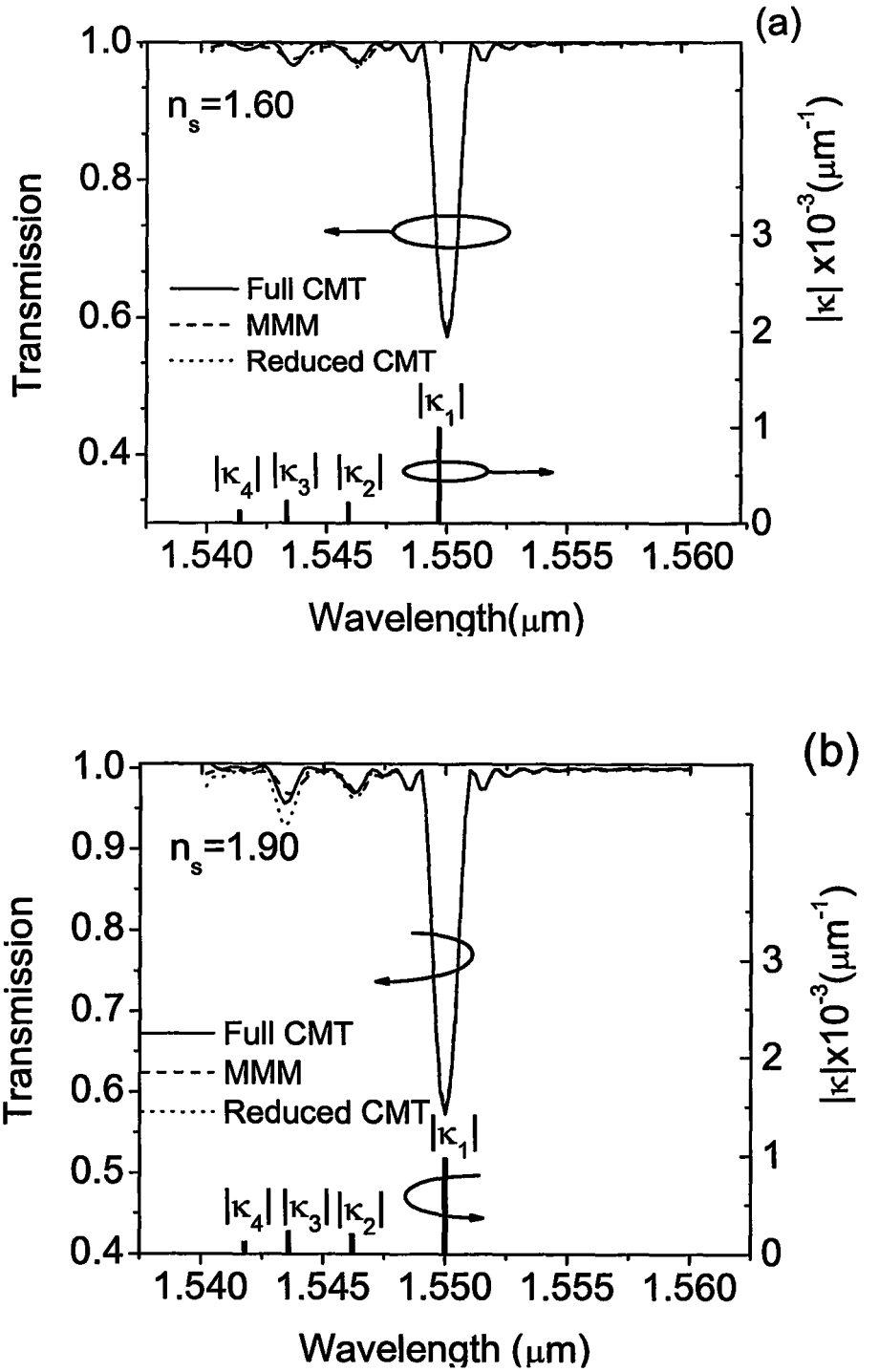

Figure 5.5. Transmission spectra with n_s larger than n_{cl}: (a) n_s=1.60; (b) n_s=1.90.

5.5 Applications of CMT in Transmissive Gratings

Long period gratings (LPG) have attracted widespread interest in optical communications and sensing systems for their capabilities of coupling light from the waveguide core to the cladding[93-95]. Compared with Bragg gratings, the power exchange in LPG happens between the co-propagating core mode and cladding modes. As a result, the coupling mechanism of LPG makes it highly susceptive to the refractive index of the outer cladding (also refers to surrounding media in the text)[42]. There have been many theoretical studies and experimental investigations on the LPG transmission spectra with varying surrounding materials [96-100]. For a waveguide structure with lower refractive index of the outer cladding (surrounding materials) than that of the inner cladding, the core modes and cladding modes are both guided modes. Consequently, the power exchange occurs between guided core modes and cladding modes and can be well analyzed by the conventional coupled mode theory[43]. However, if the surrounding material has a equal or higher refractive index than that of the inner cladding material, since the radiation loss becomes significant, and one has to resort to the continuous radiation modes or the approximate leaky modes [94, 100]. Under this circumstance, the conventional coupled-mode theory becomes cumbersome. Although there have been several previous works for investigation of guided-radiation mode couplings or guided-leaky mode couplings [97, 98, 100], little attention has been paid to the impact of the power leakage loss which is crucial for understanding the physical insights of guided-mode-radiative/leaky mode coupling.

This work investigates the mode coupling in long period planar gratings. Especially we will focus on the development and demonstration of simple yet revealing analytical solutions. With the help of the analytical expressions, it is clearly shown that the effect of coupling to radiation leads to a decay factor for the guided power through the waveguide.

5.5.1 Derive analytical solutions for long period gratings

The transverse geometry and the computation model are depicted Figure 3.3. The symmetric waveguide structure is designed to support a single guided core mode. n_{cl} and n_s denote refractive indices of inner cladding and outer cladding respectively. The perfectly matched layer (PML) terminated by perfectly reflecting boundaries (PRB) is introduced to truncate the computation window.

With the perfect reflection boundary facilitated with perfectly matched layers, the modal propagation constants of the unperturbed waveguide are expressed as $\beta_n = \gamma_n - j\alpha_n$. For simplicity, provided that the refractive index distribution along the long period grating core is

$$n(r,z) = n_{co} + \delta n(r,z) = n_{co} + \Delta n\left[1+\cos\left(\frac{2\pi}{\Lambda}z\right)\right] \tag{5.63}$$

where n_{co} is the refractive index of unperturbed waveguide core; Δn is the "dc" index change spatially averaged over a grating period; Λ is the period of the grating. For weak gratings ($\Delta n << n_{co}$), the relative permittivity can be approximated by

$$\varepsilon(r,z) = n_{co}^{\ 2} + 2n_{co}\Delta n\left[1+\cos\left(\frac{2\pi}{\Lambda}z\right)\right] \tag{5.64}$$

Based on the assumption that the difference between the perturbed waveguide and the reference waveguide is sufficiently small so that the fields of the perturbed waveguide could be expanded by the modes of the reference waveguide,

$$\mathbf{E}_t(r,z) = \sum_{v=0}\left[\hat{A}_v(z)+\hat{B}_v(z)\right]\mathbf{e}_v^t(\mathbf{r}) \tag{5.65}$$

$$\mathbf{H}_t(r,z) = \sum_{v=0}\left[\hat{A}_v(z)-\hat{B}_v(z)\right]\mathbf{h}_v^t(\mathbf{r}) \tag{5.66}$$

where $\hat{A}_v$ and $\hat{B}_v$ are amplitudes of the vth mode traveling along the +z and -z directions, respectively. The transverse fields can be further expressed as

$$\mathbf{E}_t(r,z) = \sum_{v=0}\left[A_v(z)\exp(-j\beta_v z)+B_v(z)\exp(+j\beta_v z)\right]\mathbf{e}_v^t(\mathbf{r}) \tag{5.67}$$

$$\mathbf{H}_t(r,z) = \sum_{v=0}\left[A_v(z)\exp(-j\beta_v z)-B_v(z)\exp(+j\beta_v z)\right]\mathbf{h}_v^t(\mathbf{r}) \tag{5.68}$$

where A_v and B_v are slowly varying amplitudes of the v-th mode traveling in the +z and -z directions respectively. It should be stressed that, for complex modes with leakage loss, $\hat{A}_v(z)$ decays along propagation direction while $A_v(z)$ does not.

For a weakly guided long period grating in which only one guided core mode exists, we made three reasonable simplifications: 1) the coupling among higher order co-propagation cladding modes is neglected according to the phase matching condition; 2) the incident wave is the guided forward core mode and the power is normalized as 1W; 3) backward coupling is negligible. By substitution of fields of the perturbed waveguide

section to Maxwell equations and utilizing the orthogonal relations discussed above, a set of complex coupled mode equations can be derived

$$N_{co}\frac{dA_{co}}{dz}=-\frac{j}{2}\sum_{v=1}\kappa^{t}_{co-v}A_{v}\exp\left(2j\delta_{co-v}z\right) \tag{5.69}$$

$$N_{v}\frac{dA_{v}}{dz}=-\frac{j}{2}\kappa^{t}_{v-co}A_{co}\exp\left(-2j\delta_{co-v}z\right) \tag{5.70}$$

where the complex detuning factors δ_{co-v} is defined as

$$\delta_{co-v}=\frac{1}{2}\left(\beta_{co}-\beta_{v}-2\pi/\Lambda\right)=\frac{1}{2}\left(\gamma_{co}-\gamma_{v}-2\pi/\Lambda\right)+\frac{j}{2}\alpha_{v} \tag{5.71}$$

The coupling coefficients are given by

$$\kappa_{co-v}=\frac{\omega\varepsilon_{o}}{4}\iint_{core}2n_{co}\Delta n\left(\mathbf{e}^{t}_{v}\cdot\mathbf{e}^{t}_{co}-\frac{n^{2}}{\tilde{n}^{2}}\mathbf{e}^{z}_{v}\cdot\mathbf{e}^{z}_{co}\right)da \tag{5.72}$$

In practice, the mode interactions are determined mainly by two critical factors, e.g., the detuning factor and the coupling coefficient. Appreciable power exchange happens only when the detuning factor is minimized (i.e., the phase is matched and the loss is not excessive) and the coupling is relatively strong. This implies that we may apply the above two conditions as a filtering condition to simplify the analysis. In most cases, only two modes may likely meet the above conditions at and around a given wavelength. For this reason, the multiple coupled equations may be reduced to only two equations corresponding to the said minimum detuning condition. At any given wavelength, suppose the critical modes with smallest detuning factor and relative large coupling coefficient interacting with the fundamental core mode is identified, the coupled modes equations can be simplified to two mode equations

$$\frac{dA_{co}}{dz} = -\frac{j}{2}\kappa^{t}_{co-v}A_{v}\exp\left(+2j\delta_{co-v}z\right) \tag{5.73}$$

$$N_{v}\frac{dA_{v}}{dz} = -\frac{j}{2}\kappa^{t}_{v-co}A_{co}\exp\left(-2j\delta_{co-v}z\right) \tag{5.74}$$

Throughout this study, these simplified complex coupled mode equations are referred to as the reduced coupled mode equations.

For a long period grating, the boundary conditions are $A_{co}(z=0)=1$ and $A_{v}(z=0)=0$. The analytical solutions for the co-propagating modes are

$$\hat{A}_{co}(z) = \frac{-j\delta_{co-v}\sin(Sz)+S\cos(Sz)}{S}\exp\left(-j\left(\beta_{co}-\delta_{co-v}\right)z\right) \tag{5.75}$$

$$\hat{A}_{v}(z) = -j\frac{\kappa_{co-v}}{2N_{v}}\frac{\sin(Sz)}{S}\exp\left(-j\left(\beta_{v}+\delta_{co-v}\right)z\right) \tag{5.76}$$

where

$$S = \sqrt{\frac{\kappa^{2}_{co-v}}{4N_{v}}+\delta^{2}_{co-v}} \tag{5.77}$$

For phase matched modes with $\mathrm{Re}(\delta_{co-v})\approx 0$,

$$S \approx \sqrt{\frac{\kappa^{2}_{co-v}}{4N_{v}}-\frac{\alpha^{2}_{v}}{4}} \tag{5.78}$$

The core mode power variation along the propagation direction can be easily derived,

$$P_{co} = \left|\hat{A}_{co}(z)\right|^{2} = \left|\cos(Sz)-\frac{\alpha_{v}}{2}\frac{\sin(Sz)}{S}\right|^{2}\exp\left(-\alpha_{v}z\right) \tag{5.79}$$

Eq. (5.79) is remarkably simple, yet quite revealing. The term $\left|\cos(Sz)-\frac{\alpha_{v}}{2}\frac{\sin(Sz)}{S}\right|^{2}$ represents the power exchange between the core mode and the

complex mode, whereas the multiplier $\exp(-\alpha_v z)$ stands for the leakage loss. For the phase mismatched modes, considering the case in which $\delta_{co-v} >> \frac{1}{2}\sqrt{\kappa_{co-v}^2 / N_v}$, we have

$$S \approx \delta_{co-v} \tag{5.80}$$

The power of the complex mode variation along the propagation direction can be approximated by

$$P_v = |A_v(z)|^2 \approx \left|\frac{\kappa_{co-v}}{4SN_v}\right|^2 \left|\exp(-\alpha_v z) - \exp\left(-j\,\mathrm{Re}(2\delta_{co-v})z\right)\right|^2 \tag{5.81}$$

For long distance, $\exp(-\alpha_v z) \approx 0$,

$$P_v = |A_v(z)|^2 \approx \left|\frac{\kappa_{co-v}}{4SN_v}\right|^2 \tag{5.82}$$

5.5.2 Examples of CMT in long period gratings

We consider a long period grating with the following structure parameters: period $\Lambda = 300$ μm, length $L = 30$ mm, the grating is written in the core with the "dc" index change $\Delta n = 2\times10^{-4}$; core radius $r_{co} = 2.5\mu m$, cladding radius $r_{cl} = 62.5$ μm; the refractive index of the core $n_{co} = 1.458$ and the refractive index of the inner cladding n_{cl}=1.45. Long period gratings with three different surrounding materials (n_s) will be analyzed as follows:

Case I. Long period grating with lower refractive index surrounding medium ($n_s < n_{cl}$)

In this case ($n_s < n_{cl}$), the waveguide structure supports a number of guided cladding modes. As a result, the key parameters in the coupled mode equations, i.e., the coupling coefficients, the normalizing factors, and the detuning factors, are all real. The

complex coupled-mode theory therefore is the same as the conventional coupled mode theory. Through identifying the phase matching conditions, the transmission spectra can be easily obtained. We plot the transmission spectra for n_s=1.0 and n_s=1.44 in Figure 5.6. A blue shift of the transmission is observed as the increase of the refractive index of the surrounding material.

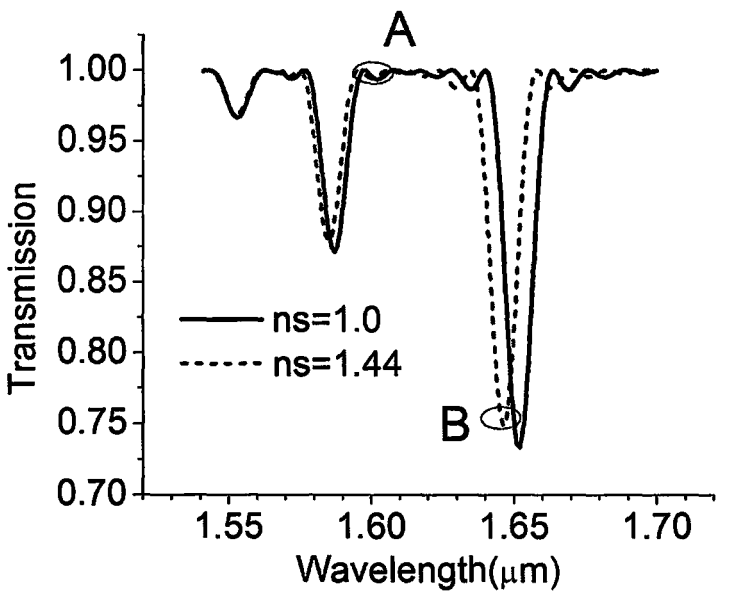

Figure 5.6. Transmission spectra of LPG with low refractive index outer cladding.

The power conservation is studied by assessing the power carried by the guided core mode and the cladding mode (which is the most closely phase-matched) when n_s=1.44. The LPG is investigated at two wavelengths, i.e., 1600nm (the out of phase point) and 1645nm (the in phase point) as indicated in Figure 5.6. The simulation results in Figure 5.7 show that power exchange between the coupled modes becomes significant

only at the phase matched point. Also the power conservation along the propagation direction is observed.

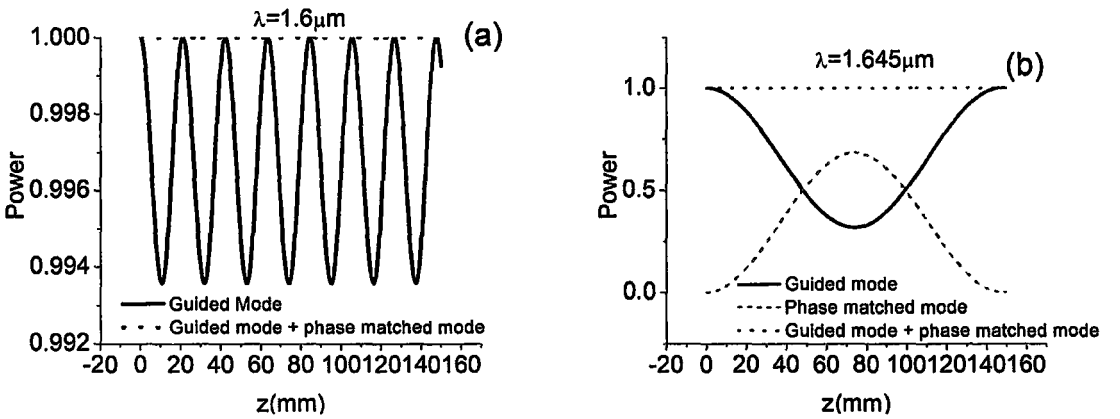

Figure 5.7. Power variation along propagation direction for LPG with lower refractive index of the outer cladding layer (n_s=1.44): (a) out of phase point; (b) in-phase point.

Case II. Long period grating with higher index surrounding medium $n_s > n_{cl}$

If the surrounding material has a higher refractive index than that of the inner cladding, the cladding modes become complex cladding modes in which the field mainly is confined in the inner cladding while oscillated in the surrounded materials. To disclose the impact of variations of the surrounding materials, we studied the LPG with two different refractive indices of the outer cladding medium. The detuning factors as functions of wavelengths in Figure 5.8 show that each dip in the transmission spectra corresponds to a specific phase matching point. For this reason, the reduced coupled mode equation is valid and can be used to predict the performance of the LPG. The transmission spectra shown in Figure 5.8 (b) indicate that the coupling strength is enhanced with the increase of the refractive index for the outer cladding.

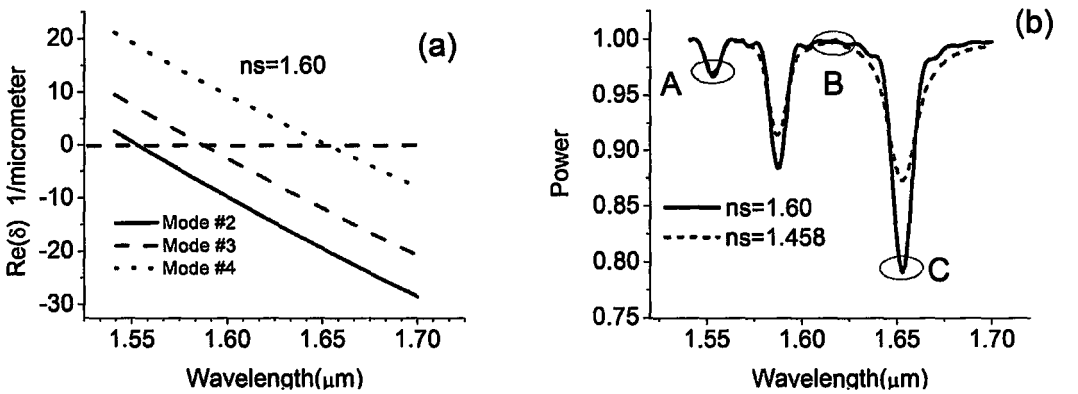

Figure 5.8. Characteristics of LPG with high refractive index surrounding media: (a) detuning factor as a function of wavelengths; (b) transmission spectra.

To provide physical insights for the guided-complex modes coupling, the power variations of the guided core mode are studied by investigating the LPG with n_s=1.60 at 1553nm. The core mode power is determined by two factors: the coupling factor and the decaying factor. We plot the power solely affected by the coupling factor, the power decided by decaying factor, and the power considering both the coupling factor and the decaying factor, respectively (in Figure 5.9). The result in Figure 5.9 (a) indicates that the core mode and complex cladding mode coupling is similar to the core mode guided cladding mode coupling if the leakage loss is small. The result in Figure 5.9 (b), on the other hand, reveals the decaying nature of the envelope of the power along the waveguide, due to the radiation loss of the complex mode. The overall power variation shown in Figure 5.9 (c) exhibits an attenuated oscillation along the propagation direction due to the power exchange and radiation loss.

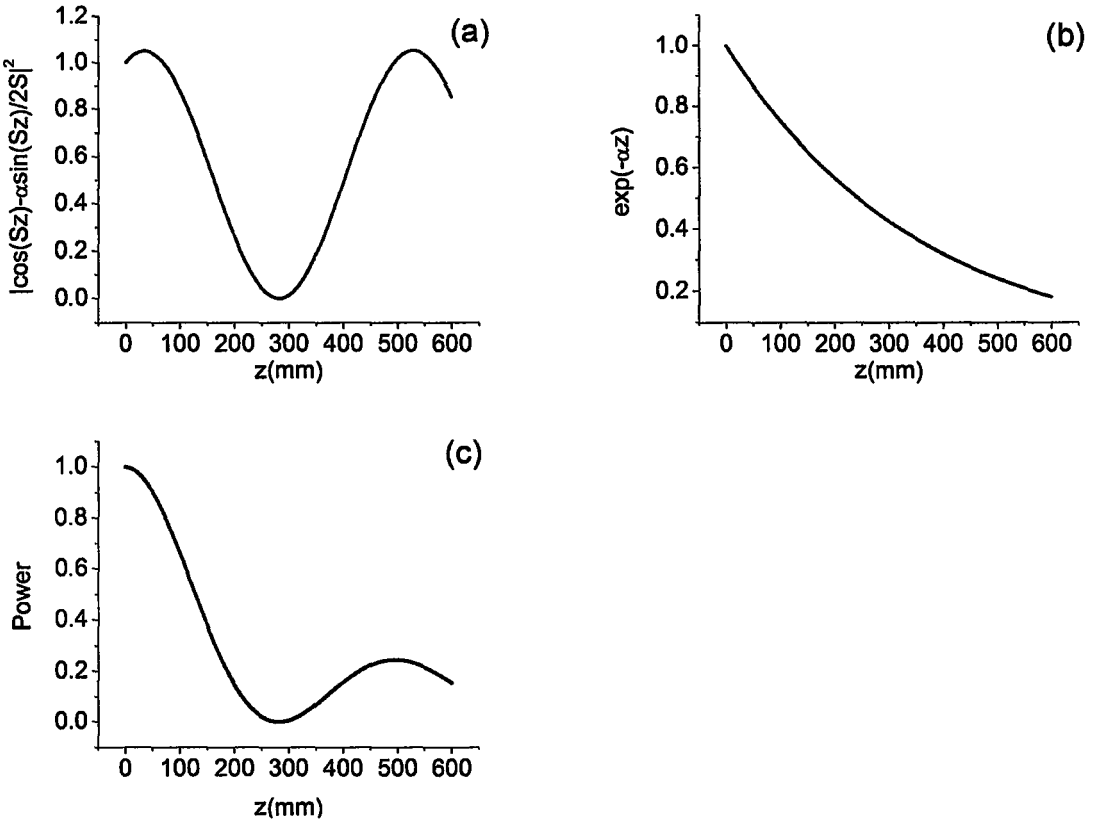

Figure 5.9. Core mode power variations along propagation direction for LPG with ns=1.60 at the wavelength equals to1553nm (Point A in Figure 5.8 (a)): (a) coupling factor; (b) decaying factor; (c) core mode power variation.

To further illustrate the salient features of the power exchange and attenuation in the presence of radiation, we examine power carried by the guided and the complex mode along the waveguide at two distinct wavelengths corresponding to the points A and C in Figure 5.8 (b). The results are shown in Figure 5.10(a) and Figure 5.10 (b), respectively. In both cases, the guided mode is coupled with the phase-matched complex mode with significant power exchange as indicated by the oscillation of the power along the waveguide. On the other hand, the coupling strength at the point A is much stronger than

that at the point C, while the leakage loss for the corresponding complex mode is much less (The effective indices of the complex modes at the points A and C are $1.45\text{-}j10^{-7}$ and$1.45\text{-}j10^{-6}$,respectively. The refractive index of the core mode is 1.451). Therefore, the power damping at the point A is smaller than that at the point C. On the other side, the total power carried by the guided mode and the complex mode decays monotonically due to the radiation loss.

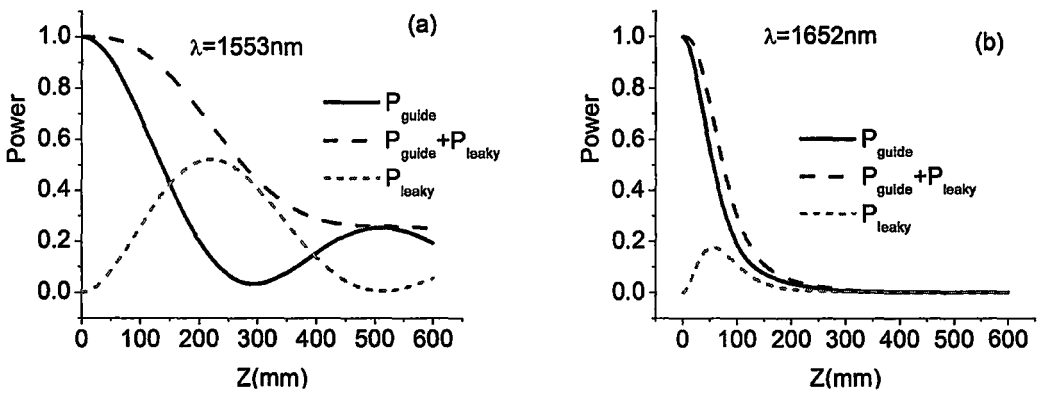

Figure 5.10. Power evolution of guided mode and complex mode as functions of propagation distance in LPG with n_s =1.60 for phase matched wavelengths: (a) wavelength equals to 1553 nm; (b) wavelength equals to 1652 nm.

For out of phase point B in Figure 5.8 (b) (wavelength equals to 1625 nm), the simulation results in Figure 5.11 indicate that: the total power decays with propagation; the power of the complex mode oscillates with a decaying envelope and approaches a constant after a certain distance; the asymptotic line is well approximated by $\left|\frac{\kappa_{co-v}}{4N_vS}\right|^2$.

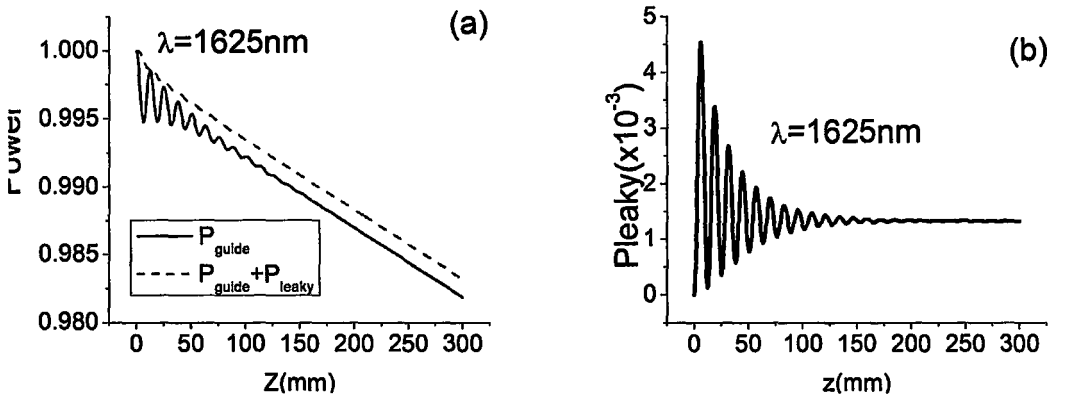

Figure 5.11. Powers of guided mode and complex mode along the propagation direction for LPG at λ=1625nm: (a) power of guided mode and the total power of the guided and complex modes; (b) power of complex mode.

Case III. Long period grating with infinite claddings ($n_s = n_{cl}$)

Now we consider the long period grating with the refractive index of the surrounding material equals to that of the cladding, e.g. LPG with infinite cladding. This seemingly simple structure has the most challenging complexity comparing to other cases in regard of computation effort for two reasons: on one hand, the cladding modes are all continuous radiation modes, implying that a set of modes will satisfy the phase matching condition; on the other hand, special attention has to be paid on choosing the PML parameters to obtain the accurate modal indices. Large computation window is preferred to reduce the mode spacing to yield a smooth transmission spectrum. In this study, the computation window is set to r_s=800μm; the PML reflection is set to 1e-50 with 5.5μm thickness on both sides. The coupling length defined by $2\pi/(\beta_{co}-\beta_v)$ is plotted in

Figure 5.12. It is shown that the many radiation modes are simultaneously close to the phase matching condition.

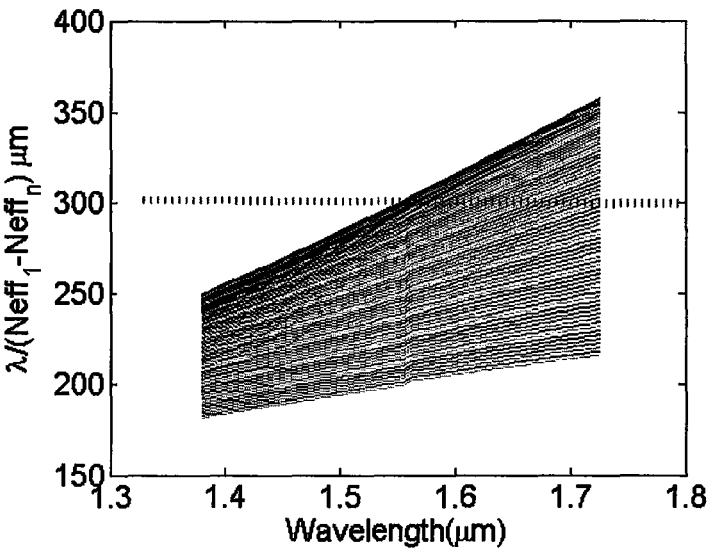

Figure 5.12. Coupling length for LPG with infinite cladding.

Strictly speaking, the reduced coupled mode equations which utilize two phase matched modes are not valid, as those modes close to resonant conditions will contribute to the power exchange and can not be neglected any more. On the other hand, by noting the fact that the interactions among the radiation modes are negligible, we may apply the approximated analytical solution as follows:

$$T = 1 - \sum_{\nu}^{N} \left(1 - \left| A_{co,\nu} \right|^2 \right) \tag{5.83}$$

where $A_{co,\nu}$ is the amplitude of the core mode coupling to the ν-th radiation mode and is obtained through eqs. (5.75). The convergence of the core mode transmission has been investigated at wavelength equals to 1725nm. The results in Figure 5.13 (a) indicate that

at least 30 modes are required to obtain a satisfactory precision. The transmission spectra in Figure 5.13 (b) confirm that the analytical approximation agrees well with the numerical solutions from the full CMT equations.

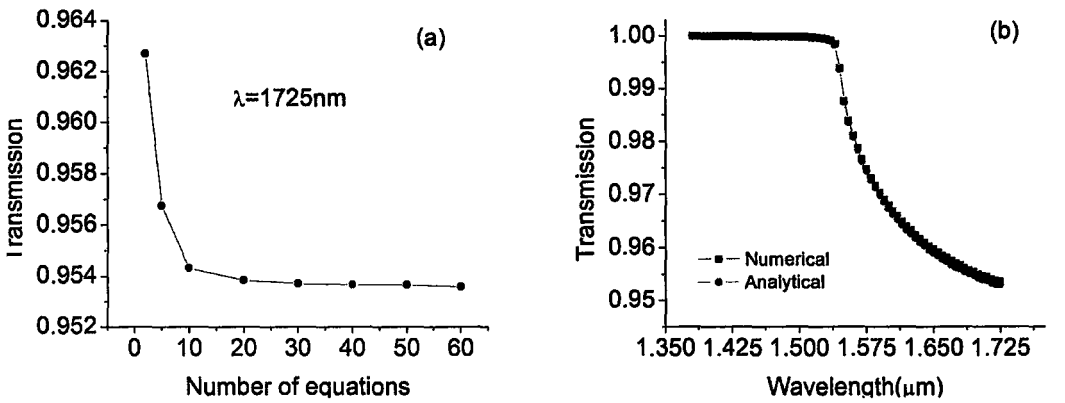

Figure 5.13. Transmission characteristics of LPG with infinite claddings. a) Convergence of complex coupled equations b) transmission spectrum.

5.6 Applications of CMT in Waveguide Taper Structure

Tapered waveguides are widely used in various optical systems to obtain a high efficient power coupling between devices with different cross-sectional geometries[101, 102]. To minimize the transition loss, the tapered waveguide structure must work adiabatically, in other words, the geometry/index variation along the propagation direction must be gradual[103]. Though the design criterion of adiabatic taper has been investigated and proposed [104], efficient and simple calculation approaches are still desirable to predict the impact of different geometrical/index parameters on the performance of the structure. Of the many modeling techniques [105-114], coupled mode analysis based on local modes has been widely adopted as a physically intuitive and

mathematically simple approach for radiation loss investigation [112-114]. The fact that the power loss results through coupling from the lowest order mode to the higher order radiation modes means, the complete mode spectrum including discrete guided and continuous radiation modes, have to be identified as a priori. Treating the radiation modes, however, is complicated due to their continuum characteristics. This work is dedicated to investigate the guided-radiation mode coupling of the tapered waveguide structure based on local modes.

5.6.1 Coupled Mode Equations Based on Local Modes

The coupled mode equations based on local modes are as follows:

$$\frac{d}{dz}a_m = -j\beta_m a_m - \sum \kappa_{mn} a_n - \sum \chi_{mn} b_n \tag{5.84}$$

$$\frac{d}{dz}b_m = j\beta_m a_m - \sum \kappa_{mn} b_n - \sum \chi_{mn} a_n \tag{5.85}$$

where

$$\kappa_{mn} = \frac{1}{4N_m}\iint\left(\frac{\partial e_{tn}}{\partial z}\times h_{tm} + e_{tm}\times\frac{\partial h_{tn}}{\partial z}\right)\cdot\hat{z}da \tag{5.86}$$

$$\chi_{mn} = \frac{1}{4N_m}\iint\left(\frac{\partial e_{tn}}{\partial z}\times h_{tm} - e_{tm}\times\frac{\partial h_{tn}}{\partial z}\right)\cdot\hat{z}da \tag{5.87}$$

The coupling coefficients can be further simplified as the approaches used by Marcuse[33],

$$\kappa_{mn} = \frac{1}{4N_m}\frac{\omega\varepsilon_0}{\beta_n - \beta_m}\iint\left(\frac{\partial n^2}{\partial z}e_{tm}\cdot e_{tn}\right)\cdot\hat{z}da \tag{5.88}$$

$$\chi_{mn} = \frac{1}{4N_m} \frac{\omega\varepsilon_0}{\beta_n + \beta_m} \iint \left(\frac{\partial n^2}{\partial z} e_{tm} \cdot e_{tn} \right) \cdot \hat{z} da \tag{5.89}$$

5.6.2 Examples and discussion

We consider a linear taper which has been investigated in the literature[111]. The structure is represented by

$$d(z) = d_{in} + z \tan\theta \tag{5.90}$$

Here θ is the taper angle.

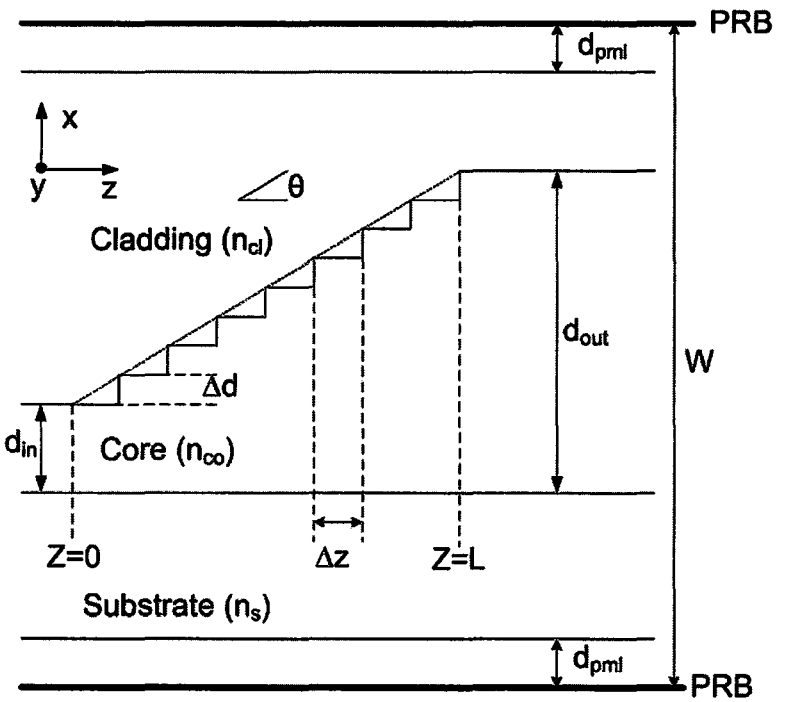

Figure 5.14. Geometry of linear taper waveguide structure

The structure geometry is shown in Figure 5.14 and the physical parameters are: refractive index of substrate n_s=1.515, refractive index of the core n_{co}=1.517, and the

refractive index of the cladding n_{cl}=1.0. The width of the input waveguide core d_{in}=5μm and the width of the output waveguide core d_{out}=10μm. The working wavelength is chosen to be λ=1.32μm. Though the ideal taper is continuous,we can use staircase approximation to evaluate the radiation loss. The number of steps (M) and grid size (Δz) along the propagation direction is determined by step height (Δd). The step height (Δd), on the other hand, is decided by the beam resolution.

For a linear taper shown above, the two refractive index profiles are the same everywhere except in the vicinity of the boundary between the cladding and the core. Moreover, for taper waveguide structure with small angles, the backward reflection is negligible. Based on the analysis, we may simplify the coupling coefficients for TE modes as

$$\kappa_{mn}(z)=\frac{\omega\varepsilon_0}{4N_m}\frac{n_{co}^2-n_{cl}^2}{\beta_n-\beta_m}\tan\theta\cdot\left(e_{tm}\cdot e_{tn}\right)_{x=d} \tag{5.91}$$

The computation parameters are as follows: the thickness of the substrate ds=55μm; computation window W=70 μm ,PML thickness is 2.5μm on both side, the PML reflection is 1e-4. The power transmission coefficient obtained by solving the coupled equations ((5.84)-(5.85)) will be referred to full CMT. For weakly coupled waveguide structure in which the mutual coupling among the higher order modes is negligible, we may consider the coupling between the fundamental mode and higher order modes separately, e.g., instead of using ((5.84)-(5.85)), the coupled equations can be expressed as:

$$\frac{d}{dz}a_1 = -j\beta_1 a_1 - \kappa_{1n}a_n \tag{5.92}$$

$$\frac{d}{dz}a_n = -j\beta_n a_n - \kappa_{n1}a_1 \tag{5.93}$$

The transmission coefficient is approximated by

$$T = 1 - \sum_n |a_n|^2 \tag{5.94}$$

The transmission obtained through (5.94)will be referred to reduced CMT. The power transmission of the studied linear taper as a function of taper angle has been shown in Figure 5.15. Comparing to the benchmark obtained from mode matching method, the results from full CMT overestimate the transmission, on the other hand, results of reduced CMT underestimate the power transmission. For small taper angle, full CMT and reduced CMT are good approximations. However, for large angle, full CMT is more accurate as the mutual coupling among higher modes becomes pronounced.

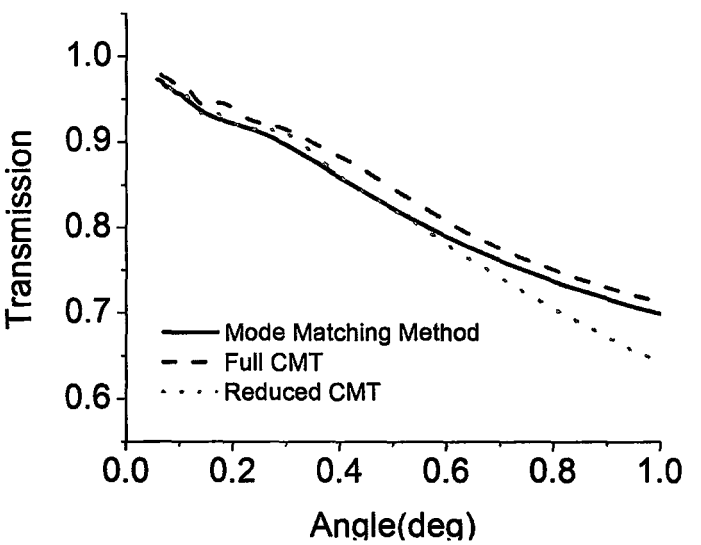

Figure 5.15. Power Transmission of a linear taper.

The convergence of the full CMT with the grid size has been investigated. The relative error of power transmission for different grid size (Δd) has been shown in Figure 5.16. It is observed that the relative error becomes smaller with the decreasing of mesh size for different taper angles. Further, the relative error decreases with the taper angle.

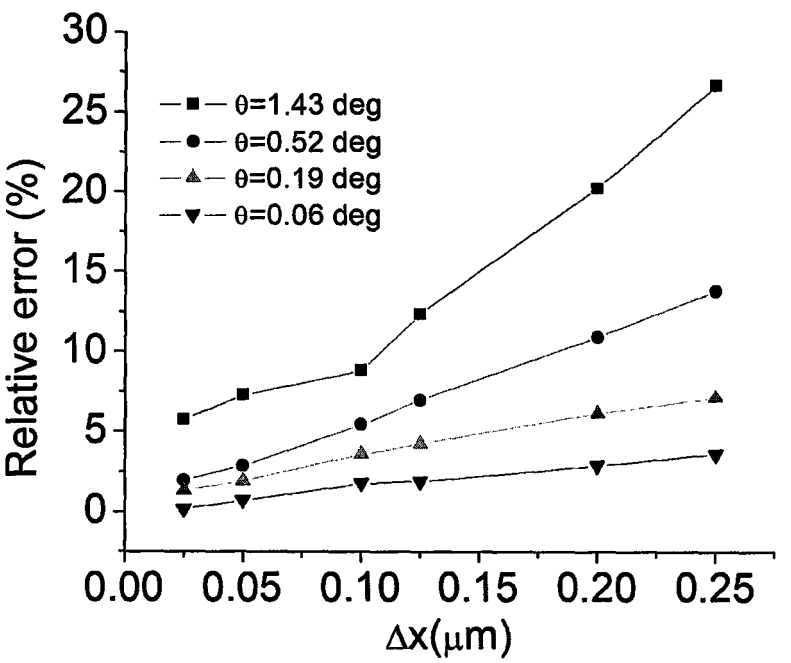

Figure 5.16. Convergence behavior of grid size (Δd).

We also studied the convergence of the full CMT with respect to the number of modes being used. It is observed from Figure 5.17 that the relative error decreases with the number of modes. Similar to the convergence behavior of the mesh sizes, the accuracy is deteriorated with the increase of the taper angle.

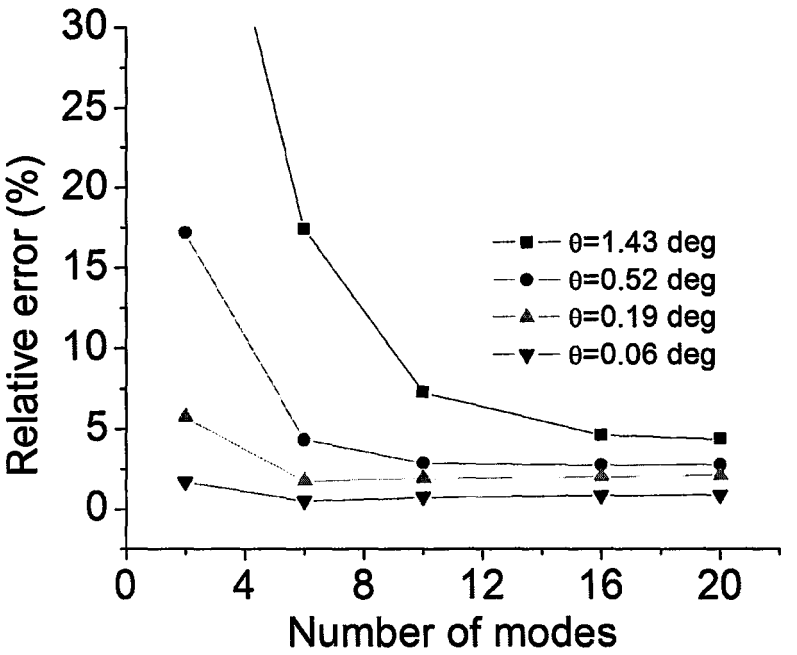

Figure 5.17. Convergence behavior of number of modes.

5.7 Summary

In this Chapter, a coupled mode theory based on complex modes has been proposed and verified through examples of short/long period gratings. Further, we formulated the complex coupled mode theory based on local mode and applied it to study the transition loss of the tapered waveguide structure. An analytical solution of radiation loss for long period grating has been derived. The effectiveness as well as the accuracy has been validated through the study of transmissive waveguide grating with different surrounding materials.

Chapter 6 Conclusions and Suggestions for Future Research

6.1 Summary of Contributions

This thesis covers a series of frequency domain modeling techniques for optical waveguide analysis. A complex coupled-mode theory and a three-dimensional complex mode matching method are developed and presented in which the radiation fields are expanded in terms of complex modes solved from a waveguide model with perfectly matched layer (PML) terminated by perfectly reflecting boundaries (PRB). The combination of PML and PRB produces an ideal waveguide model in which the physical domain of the waveguide is not affected by the reflection from the edge of the computation window, while the model fields are well defined in a finite and closed simulation environment. These complex modes are characterized by the quasi-leaky cladding modes and the PML modes, which are confined mainly in the cladding and the PML regions, respectively. These complex modes are orthogonal and can be normalized in terms of power. Design examples including slot waveguide grating, surface Plasmon polaritons gratings, short/long period gratings, and waveguide taper structures have been investigated by the proposed methods.

The major contributions of this thesis are summarized as follows:

1. We have developed a highly accurate and efficient full-vector mode-matching method based on finite-difference method. The perfectly matched layer is

employed to reduce the parasite boundary reflections. The average power and the orthogonality of the guided modes and complex modes have been discussed in detail. The scattering matrix for multi-discontinuities is derived. The developed method is applied to analyze the facet modal reflectivity of a buried waveguide. Comparison with the reported results shows that the semi-vector method is only valid for large structure aspect ratio. We also investigated the modal reflection behaviour for varied mode numbers. It is noted that the reflectivity oscillates first and converges as the mode numbers increased. The capability and accuracy of the developed method in multiple three-dimensional discontinuities have been validated by investigating the power exchange in periodically loaded waveguide polarization rotators.

2. A complex coupled mode theory has been developed. Simple analytical solutions are derived for both contra- and co-directional coupled modes in waveguide grating structures. We subsequently applied the complex coupled-mode theory to simulation of Bragg grating along the core of a symmetric slab waveguides with different refractive indices for the outer cladding. In particular, we examined the cases where the index of the outer cladding is lower, equal and higher than that of the inner cladding. While the first situation has been studied extensively by the conventional coupled-mode theory involving real guided core and cladding modes, the latter two cases are practically cumbersome to treat due to the involvement of continuous radiation modes. By using the complex coupled-mode theory, all cases can be treated readily in the same fashion and the simulation

results of the complex coupled-mode theory are shown to yield results in excellent agreement with the rigorous mode matching method. In comparison with the mode-matching method which is essentially numerical in nature, the coupled-mode theory is more intuitive and insightful. By identifying the distinct phase-matching conditions for different modes at different wavelengths, we can further reduce the coupled-mode equations to a simple two-mode formulation. Analytical solutions obtained from the reduced coupled-mode theory are shown to be highly accurate. We believe that the complex coupled-mode theory extended the scope of the conventional coupled-mode theory based on guided modes so that field radiation and leakage loss in typical optical waveguides can be treated easily, accurately and efficiently. A wide range of applications of this powerful theory can therefore envisaged with the new complex coupled-mode theory.

3. A low loss Bragg grating structure based on insulator-metal-insulator surface plasmonic waveguide has been investigated thoroughly. The rigorous and efficient complex mode-matching method (CMMM) is utilized in modeling the Bragg gratings. The key performance parameters, namely, reflection, transmission and loss spectra against the design parameters such as metallic thickness, refractive index difference of dielectric mediums have been investigated. It was shown that peak reflection is inversely proportional to the metallic strip thickness, whereas the loss increases with the metallic strip thickness. Further, the strong grating could be implemented by adjusting the difference of refractive indexes of the dielectric media. Finally, the performance, especially the advantage of the

proposed structure, is evaluated by comparing the reflection and loss spectra with the ridge gratings.

4. We have modeled and analyzed a Bragg grating structure based on dielectric slot waveguides. The complex mode-matching method (CMMM), which is accurate, efficient, and intuitive, is used for the simulation of the Bragg gratings and validated by the bi-directional beam propagation method (Bi-BPM). A systematic investigation of the key performance parameters, namely, the confinement factors and the peak reflectivity, is carried out against key design parameters such as the widths of the low-index slot and the high-index claddings, the refractive index of the slot guiding region, and the depth of the grating. It was shown that there is a trade-off between the confinement factor and the peak reflectivity against the width of the slot guiding layer as the confinement factor increases whereas the peak reflectivity decreases as the width of the slot increases. Further, we discovered that there exist optimum widths for the high-index cladding at which the confinement factor and the peak reflectivity reach their respective peak values. Finally, we investigated the reflection spectra of the Bragg grating as functions of the grating depth and observed and explained the blue shift of the peak wavelength from the conventional Bragg condition.

5. We have proposed and assessed a Bragg grating constructed by InP/InGaAsP waveguide with embedded gapped nano-metallic strips. Simulations of the spectral characteristics have been carried out by the complex mode matching method. Simulation results have shown that promising spectral characteristics can

be obtained for both TE and TM polarizations based on our different design concept from the conventional deep-etched grating. Comparing to the deep-etched grating, the fabrication simplicity of our proposed structure justifies its slight retreat on the spectral performance for the TE mode, not to mention that for the TM mode, it does present a better performance in terms of the reflection spectral bandwidth. Our studies on the design parameter dependence have also revealed that the grating duty cycle has significant impact on the grating loss. To achieve smaller grating loss, we need smaller duty cycles for both deep-etched and our proposed grating designs. Trench etching with a high aspect ratio is particularly hard, which makes the fabrication of the deep-etched grating with a small duty cycle highly costly. In our proposed grating structure, however, fabrications with different duty cycle designs are as simple, because it only involves the thin metal film removal.

6.2 Suggestions for Future Research

This thesis discusses frequency domain analysis tools for optical waveguide simulation and modeling. In particular, the coupled mode theory has been extended to radiation mode coupling through the introduction of complex modes within the framework of perfectly matched layers and zero boundary conditions. Although the complex coupled mode theory has been formulated based on local modes and normal modes and has been applied to analyze reflective/transmissive grating, tilted gratings, and tapered waveguide structures, there still remain some interesting topics worthy of further investigation:

1. Radiation coupling in second- order grating

Second order gratings have been widely used as in/out couplers in photonic integrated circuits. The most commonly used simulation method is FDTD which is computation expensive. The frequency domain methods, on the other hand, have been challenged due to the strong coupling to the radiation fields. Although the mode matching method is effective with certain periodical structures, it is not efficient for grating structure with arbitrary geometries. Conventional coupled mode theory improved with Green functions for the radiation coupling is mathematically complicated and is difficult to implement. The newly proposed complex coupled mode theory may be an efficient and physically insightful approach considering its capabilities of representing the continuous radiative fields with discretized complex modes. The potential difficulties of the complex coupled mode theory in the second-order gratings are predicted to be how to extract the proper phase-matched modes, since the higher order modes whose real part of effective indexes close to zero are all adjacent to the phase-matching conditions.

2. Hybrid simulation method

As photonic integrated circuits become the mainstream trend in both academic and industrial areas, efficient and accurate CAD tools for design and optimization of photonic devices and circuits are highly desired. However, the existing frequency/time domain algorithms are unable to meet all the requirements. Consequently, the hybrid simulation method may be the best solution in which the different methods can be cascaded through S matrix in which the element parameters are extracted from accepted techniques.

Bibliography

[1] S. E. Miller, "Integrated optics: An introduction," *Bell Sys. Tech. J.,* vol. 48, no.7, pp. 2059-2069, 1969.

[2] I. P. Kaminow, "Optical integrated circuits: A personal perspective," *J. Lightwave Technology,* vol. 26, no.9-12,pp. 994-1004, May-Jun 2008.

[3] D. Iazikov, C. Greiner, and T. W. Mossberg, "Apodizable integrated filters for coarse WDM and FTTH-type applications," *J. Lightwave Technology,* vol. 22, no.5,pp. 1402-1407, May 2004.

[4] M. Smit and Y. S. Oei, "Photonic integrated circuits for advanced communication networks," *J. Optoelectronics,* vol. 12, no.1,pp. 25-30, Jan-Mar 1998.

[5] J. J. G. M. van der Tol, Y. S. Oei, U. Khalique, R. Notzel, and M. K. Smit, "InP-based photonic circuits: Comparison of monolithic integration techniques," *Progress in Quantum Electron,* vol. 34, no.4,pp. 135-172, Jul 2010.

[6] Y. Sakamaki, K. Hattori, Y. Nasu, T. Hashimoto, Y. Hashizume, T. Mizuno, T. Goh, and H. Takahashi, "One-chip integrated polarisation-multiplexed DQPSK demodulator using silica-based planar lightwave circuit technology," *Electron Lett,* vol. 46, no.16,pp. 1152-1153, Aug. 2010.

[7] Y. Sakamaki, H. Yamazaki, T. Mizuno, T. Goh, Y. Nasu, T. Hashimoto, S. Kamei, K. Hattori, H. Takahashi, T. Kobayashi, and M. Ishikawa, "Dual polarisation optical hybrid using silica-based planar lightwave circuit technology for digital coherent receiver," *Electronics Letters,* vol. 46, no.1,pp. 58-59, Jan. 2010.

[8] H. Fukuda, K. Yamada, T. Tsuchizawa, T. Watanabe, H. Shinojima, and S. I. Itabashi, "Silicon photonic circuit with polarization diversity," *Opt. Express,* vol. 16, no.7,pp. 4872-4880, Mar 2008.

[9] W. Bogaerts, D. Taillaert, P. Dumon, D. Van Thourhout, and R. Baets, "A polarization-diversity wavelength duplexer circuit in silicon-on-insulator photonic wires," *Opt Express,* vol. 15, no.4,pp. 1567-1578, Feb 2007.

[10] R. Nagarajan, M. Kato, J. Pleumeekers, P. Evans, D. Lambert, A. Chen, V. Dominic, A. Mathur, P. Chavarkar, M. Missey, A. Dentai, S. Hurtt, J. Baeck, R. Muthiah, S. Murthy, R. Salvatore, S. Grubb, C. Joyner, J. Rossi, R. Schneider, M. Ziari, F. Kish, and D. Welch, "Single-chip 40-channel InP transmitter photonic integrated circuit capable of aggregate data rate of 1.6Tbit/s," *Electron Lett,* vol. 42, no.13,pp. 771-773, Jun 2006.

[11] W. A. Zortman, D. C. Trotter, and M. R. Watts, "Silicon photonics manufacturing," *Opt Express,* vol. 18, no.23,pp. 23598-23607, Nov 2010.

[12] B. Jalali, S. Yegnanarayanan, T. Yoon, T. Yoshimoto, I. Rendina, and F. Coppinger, "Advances in silicon-on-insulator optoelectronics," *IEEE J Selected Topics in Quantum Electronics,* vol. 4, no.6,pp. 938-947, Nov-Dec 1998.

[13] A. J. Lowery, "Computer-aided photonics design," *IEEE Spectrum,* vol. 34, no.4,pp. 26-31, Apr 1997.

[14] D. Gallagher, "Photonic CAD matures," in *IEEE LEOS newsletter*, pp. 8-14, Feb, 2008.

[15] R. Soref, "The past, present, and future of silicon photonics," *IEEE J. Selected Topics in Quantum Electron,* vol. 12, no.6,pp. 1678-1687, Nov-Dec 2006.

[16] C. Xu, "CAD for photonic devices and circuit," in *Asia Optical Fiber Comm & Optoelectronic Expo* Shanghai, 2006.

[17] A. Taflove and S.C.Hagness, *Computational Electrodynamics : the finite-difference time-domain method* Boston: Artech House, 2005.

[18] K. S. Yee, "Numerical solution of initial boundary value problems involving Maxwell's equations in isotropic media," *IEEE Trans. Antennas Propagat,* vol. 16, no.3,pp. 302-307, 1966.

[19] D. Marcuse, "Coupled mode theory of round optical fibers," *Bell Sys. Tech. J.,* vol. 52, no.6,pp. 817-842, 1973.

[20] A. Yariv, "Coupled-mode theory for guided-wave optics," *IEEE J Quantum Electron,* vol. 9, no.9,pp. 919-933, 1973.

[21] W. Snyder, "Coupled-mode theory for optical fibers," *J. Opt. Soc.Am,* vol. 62, no.11,pp. 1267-1277, 1972.

[22] S. E. Miller, "Coupled-wave theory and waveguide applications," *Bell Sys. Tech. J.,* vol. 33, no.3,pp. 661-719, 1954.

[23] M. D. Feit and J. A. Fleck, "Light-Propagation in Graded-Index Optical Fibers," *Applied Optics,* vol. 17, no.24,pp. 3990-3998, 1978.

[24] J. Gerdes and R. Pregla, "Beam-Propagation Algorithm Based on the Method of Lines," *J. Opt.l Soc Am B,* vol. 8, no.2,pp. 389-394, Feb 1991.

[25] G. R. Hadley, "Wide-Angle Beam Propagation Using Pade Approximant Operators," *Opt Lett,* vol. 17, no.20,pp. 1426-1428, Oct 15 1992.

[26] H. Shigesawa and M. Tsuji, "Mode Propagation through a Step Discontinuity in Dielectric Planar Wave-Guide," *IEEE Trans Microwave Theory and Techniques,* vol. 34, no.2,pp. 205-212, Feb 1986.

[27] T. E. Rozzi, "Rigorous Analysis of Step Discontinuity in a Planar Dielectric Waveguide," *IEEE Trans. Microwave Theory and Techniques,* vol. 26, no.10,pp. 738-746, 1978.

[28] H. A. Jamid and M. Z. M. Khan, "3-D full-vectorial analysis of strong optical waveguide discontinuities using Pade approximants," *IEEE J. Quantum Electron,* vol. 43, no.3-4,pp. 343-349, Mar-Apr 2007.

[29] P. L. Ho and Y. Y. Lu, "A bidirectional beam propagation method for periodic waveguides," *IEEE Photon. Technology Lett,* vol. 14, no.3,pp. 325-327, Mar 2002.

[30] P. L. Ho and Y. Y. Lu, "A stable bidirectional propagation method based on scattering operators," *IEEE Photon Technology Lett,* vol. 13, no.12,pp. 1316-1318, Dec 2001.

[31] J. Ctyroky, S. Helfert, R. Pregla, P. Bienstman, R. Baets, R. De Ridder, R. Stoffer, G. Klaasse, J. Petracek, P. Lalanne, J. P. Hugonin, and R. M. De La Rue, "Bragg waveguide grating as a 1D photonic band gap structure: COST 268 modelling task," *Opt. Quantum Electron,* vol. 34, no.5,pp. 455-470, May-Jun 2002.

[32] K. Q. Le, "Complex Pade approximant operators for wide-angle beam propagation," *Optics Communications,* vol. 282, no.7,pp. 1252-1254, Apr 1 2009.

[33] D. Marcuse, *Theory of dielectric optical waveguides*. New York: Academic Press, 1974.

[34] H. Kogelnik, "Theory of dielectric waveguides," in *Integrated Optics*, T. Tamir, Ed. New York: Springer-Verlag, 1975.

[35] A. Hardy and W. Streifer, "Coupled Mode Theory of Parallel Wave-Guides," *J. Lightwave Technol,* vol. 3, no.5,pp. 1135-1146, 1985.

[36] H. A. Haus, W. P. Huang, S. Kawakami, and N. A. Whitaker, "Coupled-Mode Theory of Optical Wave-Guides," *J. Lightwave Technology,* vol. 5, no.1,pp. 16-23, Jan 1987.

[37] H. A. Haus, W. P. Huang, and A. W. Snyder, "Coupled-mode formulations," *Opt. Lett,* vol. 14, no.21,pp. 1222-1224, Nov 1 1989.

[38] W. P. Huang and H. A. Haus, "Self-Consistent Vector Coupled-Mode Theory for Tapered Optical Wave-Guides," *J. Lightwave Technology,* vol. 8, no.6,pp. 922-926, Jun 1990.

[39] H. A. Haus and W. P. Huang, "Coupled-Mode Theory," *Proc.of the IEEE,* vol. 79, no.10,pp. 1505-1518, Oct 1991.

[40] S. L. Chuang, "A Coupled Mode Formulation by Reciprocity and a Variational Principle," *J Lightwave Technology,* vol. 5, no.1,pp. 5-15, Jan 1987.

[41] A. W. Snyder and J. D. Love, *Optical Waveguide Theory*. Chapman and Hall: Chapman and Hall, 1983.

[42] T. Erdogan, "Cladding-mode resonances in short- and long-period fiber grating filters," *J. Opt Soc Am A,* vol. 14, no.8,pp. 1760-1773, Aug 1997.

[43] T. Erdogan, "Fiber grating spectra," *J Lightwave Technology,* vol. 15, no.8,pp. 1277-1294, 1997.

[44] R. Sammut and A. W. Snyder, "Leaky Modes on a Dielectric Waveguide - Orthogonality and Excitation," *Applied Opt,* vol. 15, no.4,pp. 1040-1044, 1976.

[45] S. L. Lee, Y. C. Chung, L. A. Coldren, and N. Dagli, "On leaky mode approximations for modal expansion in multilayer open waveguides," *IEEE J. Quantum Electron,* vol. 31, no.10,pp. 1790-1802, Oct 1995.

[46] P. Bienstman and R. Baets, "Optical modelling of photonic crystals and VCSELs using eigenmode expansion and perfectly matched layers," *Opt Quantum Electron,* vol. 33, no.4-5,pp. 327-341, Apr 2001.

[47] P. Bienstman, H. Derudder, R. Baets, F. Olyslager, and D. De Zutter, "Analysis of cylindrical waveguide discontinuities using vectorial eigenmodes and perfectly matched layers," *IEEE Trans Microwave Theory and Techniques,* vol. 49, no.2,pp. 349-354, Feb 2001.

[48] H. Derudder, D. De Zutter, and F. Olyslager, "Analysis of waveguide discontinuities using perfectly matched layers," *Electron Lett,* vol. 34, no.22,pp. 2138-2140, Oct 29 1998.

[49] H. Derudder, F. Olyslager, D. De Zutter, and S. Van den Berghe, "Efficient mode-matching analysis of discontinuities in finite planar substrates using perfectly matched layers," *IEEE Tran on Antennas and Propagation,* vol. 49, no.2,pp. 185-195, Feb 2001.

[50] K. Jiang and W. P. Huang, "Finite-difference-based mode-matching method for 3-D waveguide structures under semivectorial approximation," *J Lightwave Technology,* vol. 23, no.12,pp. 4239-4248, Dec 2005.

[51] Y. Shani, R. Alferness, T. Koch, U. Koren, M. Oron, B. I. Miller, and M. G. Young, "Polarization Rotation in Asymmetric Periodic Loaded Rib Wave-Guides," *Applied Phys Lett,* vol. 59, no.11,pp. 1278-1280, Sep 9 1991.

[52] C. Vassallo, "1993-1995 optical mode solvers," *Opt Quantum Electron,* vol. 29, no.2,pp. 95-114, Feb 1997.

[53] Y. P. Chiou, Y. C. Chiang, and H. C. Chang, "Improved three-point formulas considering the interface conditions in the finite-difference analysis of step-index optical devices," *J Lightwave Tech,* vol. 18, no.2,pp. 243-251, Feb 2000.

[54] M. S. Stern, "Semivectorial Polarized Finite-Difference Method for Optical Wave-Guides with Arbitrary Index Profiles," *IEE Proc. J. Optoelectronics,* vol. 135, no.1,pp. 56-63, Feb 1988.

[55] C. L. Xu, W. P. Huang, M. S. Stern, and S. K. Chaudhuri, "Full-Vectorial Mode Calculations by Finite-Difference Method," *IEE Proc. J. Optoelectronics,* vol. 141, no.5,pp. 281-286, Oct 1994.

[56] E. Anemogiannis, E. N. Glytsis, and T. K. Gaylord, "Determination of guided and leaky modes in lossless and lossy planar multilayer optical waveguides: Reflection pole method and wavevector density method," *J Lightwave Technology,* vol. 17, no.5,pp. 929-941, May 1999.

[57] J. Chilwell and I. Hodgkinson, "Thin-Films Field-Transfer Matrix-Theory of Planar Multilayer Waveguides and Reflection from Prism-Loaded Waveguides," *J. Opt. So Am A,* vol. 1, no.7,pp. 742-753, 1984.

[58] J. Petracek and K. Singh, "Determination of leaky modes in planar multilayer waveguides," *IEEE Photon Tech Lett,* vol. 14, no.6,pp. 810-812, Jun 2002.

[59] C. Vassallo, "Improvement of Finite-Difference Methods for Step-Index Optical Wave-Guides," *IEE Proc J Optoelectronics,* vol. 139, no.2,pp. 137-142, Apr 1992.

[60] Y. C. Chiang, Y. P. Chiou, and H. C. Chang, "Improved full-vectorial finite-difference mode solver for optical waveguides with step-index profiles," *J Lightwave Technology,* vol. 20, no.8,pp. 1609-1618, Aug 2002.

[61] W. P. Huang, C. L. Xu, W. Lui, and K. Yokoyama, "The perfectly matched layer (PML) boundary condition for the beam propagation method," *IEEE Photon Tech Lett,* vol. 8, no.5,pp. 649-651, May 1996.

[62] M. Reed, P. Sewell, T. M. Benson, and P. C. Kendall, "Efficient propagation algorithm for 3D optical waveguides," *IEE Proc-Optoelectronics,* vol. 145, no.1,pp. 53-58, Feb 1998.

[63] E. Silberstein, P. Lalanne, J. P. Hugonin, and Q. Cao, "Use of grating theories in integrated optics," *J Opt Soc Am A,* vol. 18, no.11,pp. 2865-2875, Nov 2001.

[64] T. Ando, T. Murata, H. Nakayama, J. Yamauchi, and H. Nakano, "Analysis and measurement of polarization conversion in a periodically loaded dielectric waveguide," *IEEE Photon Tech Lett,* vol. 14, no.9,pp. 1288-1290, Sep 2002.

[65] K. Kawano, T. Kitoh, M. Kohtoku, T. Takeshita, and Y. Hasumi, "3-D semivectorial analysis to calculate facet reflectivities of semiconductor optical waveguides based on the bi-directional method of line BPM (MoL-BPM)," *IEEE Photon Tech Lett,* vol. 10, no.1,pp. 108-110, Jan 1998.

[66] V. R. Almeida, Q. F. Xu, C. A. Barrios, and M. Lipson, "Guiding and confining light in void nanostructure," *Opt Lett,* vol. 29, no.11,pp. 1209-1211, Jun 2004.

[67] N. N. Feng, J. Michel, and L. C. Kimerling, "Optical field concentration in low-index waveguides," *IEEE Quantum Electron,* vol. 42, no.9-10,pp. 885-890, Sep-Oct 2006.

[68] M. Lipson, "Guiding, modulating, and emitting light on silicon - Challenges and opportunities," *J. Lightwave Technology,* vol. 23, no.12,pp. 4222-4238, Dec 2005.

[69] Q. F. Xu, V. R. Almeida, R. R. Panepucci, and M. Lipson, "Experimental demonstration of guiding and confining light in nanometer-size low-refractive-index material," *Opt Lett,* vol. 29, no.14,pp. 1626-1628, Jul 15 2004.

[70] C. Vassallo, *Optical Waveguide Concepts.* Amsterdam: Elsevier, 1991.

[71] T. Baehr-Jones, M. Hochberg, G. X. Wang, R. Lawson, Y. Liao, P. A. Sullivan, L. Dalton, A. K. Y. Jen, and A. Scherer, "Optical modulation and detection in slotted Silicon waveguides," *Opt Express,* vol. 13, no.14,pp. 5216-5226, Jul 11 2005.

[72] T. Fujisawa and M. Koshiba, "Polarization-independent optical directional coupler based on slot waveguides," *Opt Lett,* vol. 31, no.1,pp. 56-58, Jan 1 2006.

[73] F. Dell'Olio and V. M. N. Passaro, "Optical sensing by optimized silicon slot waveguides," *Opt Express,* vol. 15, no.8,pp. 4977-4993, Apr 16 2007.

[74] T. Fujisawa and M. Koshiba, "Theoretical investigation of ultrasmall polarization-insensitive 1 X 2 multimode interference waveguides based on sandwiched structures," *IEEE Photon Tech Lett,* vol. 18, no.9-12,pp. 1246-1248, 2006 2006.

[75] H. Zhang, J. W. Mu, and W. P. Huang, "Improved bidirectional beam-propagation method by a fourth-order finite-difference scheme," *J Lightwave Technology,* vol. 25, no.9,pp. 2807-2813, Sep 2007.

[76] W. L. Barnes, A. Dereux, and T. W. Ebbesen, "Surface plasmon subwavelength optics," *Nature,* vol. 424, no.6950,pp. 824-830, Aug 14 2003.

[77] L. Chen, J. Shakya, and M. Lipson, "Subwavelength confinement in an integrated metal slot waveguide on silicon," *Opt Lett,* vol. 31, no.14,pp. 2133-2135, Jul 15 2006.

[78] G. Gay, O. Alloschery, B. V. De Lesegno, C. O'Dwyer, J. Weiner, and H. J. Lezec, "The optical response of nanostructured surfaces and the composite diffracted evanescent wave model," *Nature Physics,* vol. 2, no.4,pp. 262-267, Apr 2006.

[79] K. G. Lee and Q. H. Park, "Coupling of surface plasmon polaritons and light in metallic nanoslits," *Physical Review Letters,* vol. 95, no.10,pp. -, Sep 2 2005.

[80] S. A. Maier, "Plasmonics: The promise of highly integrated optical devices," *IEEE J. Sel Top in Quantum Electron,* vol. 12, no.6,pp. 1671-1677, Nov-Dec 2006.

[81] E. Ozbay, "Plasmonics: Merging photonics and electronics at nanoscale dimensions," *Science,* vol. 311, no.5758,pp. 189-193, Jan 13 2006.

[82] H. Raether, *Surface plasmons*. New York: Springer-Verlag, 1988.

[83] S. A. Darmanyan and A. V. Zayats, "Light tunneling via resonant surface plasmon polariton states and the enhanced transmission of periodically nanostructured metal films: An analytical study," *Physical Review B,* vol. 67, no.3, pp.035424-1-7, Jan 15 2003.

[84] M. Kretschmann and A. A. Maradudin, "Band structures of two-dimensional surface-plasmon polaritonic crystals," *Physical Review B,* vol. 66, no.24,pp. 245408-1-7, Dec 15 2002.

[85] J. M. Steele, C. E. Moran, A. Lee, C. M. Aguirre, and N. J. Halas, "Metallodielectric gratings with subwavelength slots: Optical properties," *Physical Review B,* vol. 68, no.20,pp.205103-1 -7, Nov 2003.

[86] A. Boltasseva, T. Nikolajsen, K. Leosson, K. Kjaer, M. S. Larsen, and S. I. Bozhevolnyi, "Integrated optical components utilizing long-range surface plasmon polaritons," *J. Lightwave Technology,* vol. 23, no.1,pp. 413-422, Jan 2005.

[87] Z. H. Han, E. Forsberg, and S. L. He, "Surface plasmon Bragg gratings formed in metal-insulator-metal waveguides," *IEEE Photon Tech Lett,* vol. 19, no.2-4,pp. 91-93, Jan-Feb 2007.

[88] A. Hosseini and Y. Massoud, "A low-loss metal-insulator-metal plasmonic bragg reflector," *Opt Express,* vol. 14, no.23,pp. 11318-11323, Nov 13 2006.

[89] S. Jette-Charbonneau, R. Charbonneau, N. Lahoud, G. A. Mattiussi, and P. Berini, "Bragg gratings based on long-range surface plasmon-polariton waveguides: Comparison of theory and experiment," *IEEE J. Quantum Electron,* vol. 41, no.12,pp. 1480-1491, Dec 2005.

[90] T. Sondergaard, S. I. Bozhevolnyi, and A. Boltasseva, "Theoretical analysis of ridge gratings for long-range surface plasmon polaritons," *Physical Review B,* vol. 73, no.4,pp. 045320-1-7, Jan 2006.

[91] V. M. Fitio and Y.V.Bobitski, "HIgh transmission of system dielectric grating thin film dielectric grating," in *Laser Fiber Opt. Netw. Model.* , Yalta, Crimea, 2005.

[92] J. Yamauchi, T. Yamazaki, K. Sumida, and H. Nakano, "TE/TM wave splitters using surface plasmon polaritons," in *Integrated Photonics and Nanophotonics Research and Applications*, 2007.

[93] V. Bhatia and A. M. Vengsarkar, "Optical fiber long-period grating sensors," *Opt. Lett.,* vol. 21, no.9,pp. 692-694, May 1 1996.

[94] H. J. Patrick, G. M. Williams, A. D. Kersey, J. R. Pedrazzani, and A. M. Vengsarkar, "Hybrid fiber Bragg grating/long period fiber grating sensor for strain/temperature discrimination," *IEEE Photon Tech Lett,* vol. 8, no.9,pp. 1223-1225, Sep 1996.

[95] A. M. Vengsarkar, P. J. Lemaire, J. B. Judkins, V. Bhatia, T. Erdogan, and J. E. Sipe, "Long-period fiber gratings as band-rejection filters," *J. Lightwave Technology,* vol. 14, no.1,pp. 58-65, Jan 1996.

[96] O. Duhem, J. F. Henninot, M. Warenghem, and M. Douay, "Demonstration of long-period-grating efficient couplings with an external medium of a refractive index higher than that of silica," *Applied Opt,* vol. 37, no.31,pp. 7223-7228, Nov 1 1998.

[97] Y. Jeong, B. Lee, J. Nilsson, and D. J. Richardson, "A quasi-mode interpretation of radiation modes in long-period fiber gratings," *IEEE J Quantum Electron,* vol. 39, no.9,pp. 1135-1142, Sep 2003.

[98] Y. Koyamada, "Numerical analysis of core-mode to radiation-mode coupling in long-period fiber gratings," *IEEE Photon Tech Lett,* vol. 13, no.4,pp. 308-310, Apr 2001.

[99] H. J. Patrick, A. D. Kersey, and F. Bucholtz, "Analysis of the response of long period fiber gratings to external index of refraction," *J. Lightwave Technology,* vol. 16, no.9,pp. 1606-1612, Sep 1998.

[100] D. B. Stegall and T. Erdogan, "Leaky cladding mode propagation in long-period fiber grating devices," *IEEE Photon Technology Lett,* vol. 11, no.3,pp. 343-345, Mar 1999.

[101] H. Yanagawa, T. Shimizu, S. Nakamura, and I. Ohyama, "Index-and-Dimensional Taper and Its Application to Photonic Devices," *J. Lightwave Technology,* vol. 10, no.5,pp. 587-592, May 1992.

[102] O. Mitomi, K. Kasaya, and H. Miyazawa, "Design of a Single-Mode Tapered Wave-Guide for Low-Loss Chip-to-Fiber Coupling," *IEEE J. Quantum Electronics,* vol. 30, no.8,pp. 1787-1793, Aug 1994.

[103] J. D. Love, W. M. Henry, W. J. Stewart, R. J. Black, S. Lacroix, and F. Gonthier, "Tapered Single-Mode Fibers and Devices .1. Adiabaticity Criteria," *IEE Proc. J Optoelectronics,* vol. 138, no.5,pp. 343-354, Oct 1991.

[104] J. Haes, J.Willems, and R.Bates, "Design of adiabatic tapers for high contrast step index waveguides," in *Proc. SPIE.* vol. 2212, 1994, pp. 685-693.

[105] D. Marcuse, "Radiation losses of tapered dielectric slab waveguides," *Bell Sys. Tech. J.,* vol. 49, 273-290, 1970.

[106] A. R. Nelson, "Coupling optical waveguides by tapers," *Applied Opt,* vol. 14, no.12,pp. 3012-3015, 1975.

[107] J. A. Fleck, J. R. Morris, and M. D. Feit, "Time-Dependent Propagation of High-Energy Laser-Beams through Atmosphere," *Applied Physics,* vol. 10, no.2,pp. 129-160, 1976.

[108] T. Nakamura and N. Suzuki, "Spot-size converted laser diodes based on mode interference," *IEEE Photon Tech Lett,* vol. 12, no.2,pp. 143-145, Feb 2000.

[109] C. T. Lee, M. L. Wu, L. G. Sheu, P. L. Fan, and J. M. Hsu, "Design and analysis of completely adiabatic tapered waveguides by conformal mapping," *J. Lightwave Technology,* vol. 15, no.2,pp. 403-410, Feb 1997.

[110] P. G. Suchoski and V. Ramaswamy, "Exact Numerical Technique for the Analysis of Step Discontinuities and Tapers in Optical Dielectric Wave-Guides," *J. Opt Soc Am A,* vol. 3, no.2,pp. 194-203, Feb 1986.

[111] P. G. Suchoski and R. V. Ramaswamy, "Design of single-mode step-tapered Waveguide sections," *IEEE J Quantum Electron.,* vol. 23, no.2,pp. 205-211, Feb 1987.

[112] A. W. Snyder, "Coupling of modes in a tapered dielectric cylinder," *IEEE Trans on Microwave Theory and Techniques,* vol. 18, no.7,pp. 383-392, 1970.

[113] A. F. Milton and W. K. Burns, "Mode-Coupling in Tapered Optical-Waveguide Structures and Electro-Optic Switches," *IEEE Trans on Circuits and Systems,* vol. 26, no.12,pp. 1020-1028, 1979.

[114] A. F. Milton and W. K. Burns, "Mode-Coupling in Optical-Waveguide Horns," *IEEE J. Quantum Electron,* vol. 13, no.10,pp. 828-835, 1977.

Appendix A Finite-Difference Form of Wave Equations

$$
\begin{aligned}
P_{xx}E_x = & \frac{2}{\Delta x_m\left(\Delta x_m+\Delta x_{m+1}\right)}\frac{n^2{}_{m+1,n}}{n^2{}_{m+0.5,n}}E_x{}^{m+1,n} \\
& +\frac{2}{\Delta x_m\left(\Delta x_m+\Delta x_{m-1}\right)}\frac{n^2{}_{m-1,n}}{n^2{}_{m-0.5,n}}E_x{}^{m-1,n} \\
& +\frac{2}{\Delta y_n\left(\Delta y_n+\Delta y_{n+1}\right)}E_x{}^{m,n+1} \\
& +\frac{2}{\Delta y_n\left(\Delta y_n+\Delta y_{n-1}\right)}E_x{}^{m,n-1} \\
& +\left(\begin{array}{l}
-\dfrac{2}{\Delta x_m\left(\Delta x_m+\Delta x_{m+1}\right)}\dfrac{n^2{}_{m,n}}{n^2{}_{m+0.5,n}}-\dfrac{2}{\Delta x_m\left(\Delta x_m+\Delta x_{m-1}\right)}\dfrac{n^2{}_{m,n}}{n^2{}_{m-0.5,n}} \\
-\dfrac{2}{\Delta y_m\left(\Delta y_m+\Delta y_{n+1}\right)}-\dfrac{2}{\Delta y_n\left(\Delta y_m+\Delta y_{n-1}\right)}+n_{m,n}^2k_0^2
\end{array}\right)E_x{}^{m,n}
\end{aligned}
$$

$$
\begin{aligned}
P_{xy}E_y = & \frac{2}{2\Delta x_m+\Delta x_{m-1}+\Delta x_{m+1}}\frac{2}{2\Delta y_m+\Delta y_{m+1}+\Delta y_{m-1}}\cdot \\
& \left[\begin{array}{l}
\left(\dfrac{n_{m+1,n+1}^2}{n_{m+1,n}^2}-1\right)E_y^{m+1,n+1}+\left(-\dfrac{n_{m+1,n-1}^2}{n_{m+1,n}^2}+1\right)E_y^{m+1,n-1} \\
+\left(-\dfrac{n_{m-1,n+1}^2}{n_{m-1,n}^2}+1\right)E_y^{m-1,n+1}+\left(\dfrac{n_{m-1,n-1}^2}{n_{m-1,n}^2}-1\right)E_y^{m-1,n-1}
\end{array}\right]
\end{aligned}
$$

$$P_{yy}E_y = \frac{1}{\Delta y_n}\frac{2}{\Delta y_{n+1}+\Delta y_n}\frac{n_{m,n+1}^2}{n_{m,n+0.5}^2}E_y^{m,n+1}$$
$$+\frac{1}{\Delta y_n}\frac{2}{\Delta y_{n-1}+\Delta y_n}\frac{n_{m,n-1}^2}{n_{m,n-0.5}^2}E_y^{m,n-1}$$
$$+\frac{1}{\Delta x_m}\frac{2}{\Delta x_{m+1}+\Delta x_m}E_y^{m+1,n}$$
$$+\frac{1}{\Delta x_m}\frac{2}{\Delta x_{m-1}+\Delta x_m}E_y^{m-1,n}$$
$$-\left(\begin{array}{l}\dfrac{1}{\Delta y_n}\dfrac{2}{\Delta y_{n+1}+\Delta y_n}\dfrac{n_{m,n}^2}{n_{m,n+0.5}^2}+\dfrac{1}{\Delta y_n}\dfrac{2}{\Delta y_{n-1}+\Delta y_n}\dfrac{n_{m,n}^2}{n_{m,n-0.5}^2}\\ +\dfrac{1}{\Delta x_m}\dfrac{2}{\Delta x_{m+1}+\Delta x_m}+\dfrac{1}{\Delta x_m}\dfrac{2}{\Delta x_{m-1}+\Delta x_m}+n_{m,n}^2k_0^2\end{array}\right)E_y^{m,n}$$

$$P_{yx}E_x = \frac{2}{2\Delta y_n+\Delta y_{n+1}+\Delta y_{n-1}}\frac{2}{2\Delta x_m+\Delta x_{m+1}+\Delta x_{m-1}}\bullet$$
$$\left[\begin{array}{l}\left(\dfrac{n_{m+1,n+1}^2}{n_{m,n+1}^2}-1\right)E_x^{m+1,n+1}+\left(-\dfrac{n_{m-1,n+1}^2}{n_{m,n+1}^2}+1\right)E_x^{m-1,n+1}\\ +\left(-\dfrac{n_{m+1,n-1}^2}{n_{m,n-1}^2}+1\right)E_x^{m+1,n-1}+\left(\dfrac{n_{m-1,n-1}^2}{n_{m,n-1}^2}-1\right)E_x^{m-1,n-1}\end{array}\right]$$

List of Publications

Refereed Journals

P.1 **J. Mu**, and W. Huang, "Complex coupled-mode theory for tapered optical waveguides," Optics Letter, **36**(6): 1026-1028, 2011.

P.2 **J. Mu**, and W. Huang, "Analytical expressions for radiation effects on guided mode propagation in long period gratings," IEEE/OSA J. Lightwave Technology, **29**(7): 997-1002, 2011.

P.3 A. Khalatpour, **J. Mu**, and W. Huang, "Modified smooth transition method for determination of complex modes in multi-layer waveguide structures," IEEE/OSA J. Lightwave Technology. **28**(19):2851-2855, 2010.

P.4 **J. Mu**, X. Li and W. Huang, "Compact Bragg Grating with Embedded Metallic Nano-Structures," Optics Express.**18** (15):15893-15900, 2010.

P.5 N. Song, **J. Mu**, W. Huang, "Application of the complex coupled-mode theory to optical fiber grating structure," IEEE/OSA J. Lightwave Technology. **28**(5):761-767, 2010.

P.6 W. Huang, **J. Mu** , "Complex coupled-mode theory for optical waveguides," Opt Express.**17** (21):19134-19152, 2009 .

P.7 **J. Mu**, C. Xu and W. Huang, "An optical power combiner/wavelength demultiplexing module for hybrid WDM FTTX," Opt Express. **17**(6): 4791-4797, 2009.

P.8 **J. Mu**, W. Huang "A low-loss surface plasmonic Bragg grating," IEEE/OSA J. Lightwave Technology. **27**(4): 436-439, 2009.

P.9 **J. Mu**, H. Zhang and W. Huang "A theoretical investigation of slot waveguide Bragg gratings," IEEE J. Quantum Electronics. **44**(7): 622-627,2008.

P.10 **J. Mu**, W. Huang, "Simulation of three-dimensional waveguide discontinuities by a full-vector mode-matching method based on finite-difference schemes," Opt Express. **16**(22):18152–18163, 2008.

P.11 **J. Mu**, H. Zhang and W. Huang, "Design of waveguide Bragg gratings with strong index corrugations," IEEE J. Lightwave Technology. **26**(12):1596-1601, 2008.

P.12 H. Zhang, **J. Mu** and W. Huang, "Assessment of rational approximations for square root operator in bidirectional beam propagation method," IEEE J. Lightwave Technology. **26**(5):600-607, 2008.

P.13 H. Zhang, **J. Mu** and W. Huang, "Improved bidirectional beam-propagation method by a fourth-order finite-difference scheme," IEEE J. Lightwave Technology. **25**(9): 2807-2813, 2007.

International Conference Papers

P.14 W. Huang, **J. Mu**, "Complex coupled mode theory for optical waveguide modeling," Asia Communications and Photonics Conference and Exhibition (Invited talk), Shanghai, 2010.

P.15 Q. Xu, **J. Mu**, C. Xu, X. Li, "Experimental and theoretical characterization of multimode fiber Bragg grating external cavity lasers," Proc. SPIE, Vol. **7386**, 73862O, 2009.

P.16 **J. Mu** W. Huang, "Low-loss insulator-metal-insulator Spps Bragg reflector. Integrated," Photonics and Nanophotonics Research and Applications (IPNRA), Boston, 2008.

P.17 **J. Mu**, H. and W. Huang, "Investigation of long-range surface plasmon polariton gratings by mode matching method," Proc. of SPIE Vol. 6642, 664213, 2007.

P.18 H. Zhang, **J. Mu** and W. Huang, "Analysis of Bragg gratings for long-range surface plasmon polaritons using the bidirectional beam propagation method based on scattering operators," Proc. of SPIE Vol. 6641, 6641Z,2007.

P.19 **J. Mu** and W. Huang, "Simulation of Surface Plasmon Polariton (SPP) Bragg Gratings by Complex Mode Matching Method," Integrated Photonics and Nanophotonics Research and Applications (IPNRA), Salt Lake City, Utah, July 8, 2007.

List of Awards

1.NSERC/JSPS Summer Program in Japan Fellowship, Canada, 2010.

2.NSERC Alexander Graham Bell Canada Graduate Scholarship (CGS), 2009-2011.

3.Ontario Graduate Scholarship, Canada, 2009.

4.NSERC Summer Program in Taiwan Fellowship, Canada, 2009.

5.SPIE Scholarship in Optical Science and Engineering, USA, 2009.

6.Chinese Government Award for Outstanding Self-financed Students Abroad,2009

7.SPIE Scholarship in Optical Science and Engineering, USA, 2008.